universität wien

MASTERARBEIT / MASTER'S THESIS

Titel der Masterarbeit / Title of the Master's Thesis

„On the Effect of Relative Humidity on the Activation of Aerosol Particles in Butanol – Based Condensation Particle Counters“

verfasst von / submitted by

Peter Josef Wlasits, BSc

angestrebter akademischer Grad / in partial fulfilment of the requirements for the degree of

Master of Science (MSc)

Wien, 2019 / Vienna, 2019

Studienkennzahl lt. Studienblatt / degree programme code as it appears on the student record sheet:	A 066 876
Studienrichtung lt. Studienblatt / degree programme as it appears on the student record sheet:	Masterstudium Physik
Betreut von / Supervisor:	Assoz. Prof. Dr. Paul Winkler, Privatdoz.

Acknowledgments

First I want to express my gratitude to Prof. Paul Winkler for giving me the opportunity to do my thesis in his group and for introducing me to so many great people. Prof. Winkler supported me throughout my thesis and gave me the opportunity to explore different fields of research. He enabled me to to visit the International Aerosol Conference in St. Louis and to participate in the Schwechat Campaign and in the CLOUD13 Campaign at CERN. I immensely benefited from working in his group.
Furthermore I want to thank Paulus Bauer, Sophia Brilke, Loic Gonzalez Carracedo, Gerald Köberl, Julian Resch, David Schmoll, Kay Scholze, Dominik Stolzenburg, Christian Tauber, Miguel Vazquez Pufleau and Daniela Wimmer, whom I really enjoyed to work with. Without the constant support of Sophia and Christian this thesis would not have been possible. I want to thank them for giving me the opportunity to make mistakes, for reviving my programming skills and for their constant encouragement. Frequent discussions with all group members helped me to solve encountered problems.
Next I want to thank my family. My parents, Doris and Hermann Wlasits, supported me throughout my studies. I want to thank them for their financial support, but much more importantly for their advice in every life situation and for believing in me and my goals. My deepest appreciation goes to my sister, Victoria Wlasits, for her encouragement and support as well as for always lending me an ear if times get tough. I also want to thank my grandparents, Magdalena and Josef Artner, and all other family members for their support.
Moreover I want to thank Prof. Paul Wagner and Dr. Gerhard Steiner for their exceptional passion of teaching basic physics and thereby ensuring a good start for my studies. I also owe a great debt of gratitude to my former class teacher Mag. Herbert Lang, whose unique way of teaching chemistry influenced all of my career related decisions.
Lastly I would like to extend my sincere thanks to my friends and fellow students.

Abstract

Condensation Particle Counters are standard instruments for measuring the particle number concentration of aerosols. The cutoff diameter is commonly used to evaluate such an instrument's performance. Seed particle activation in particle counters is mediated by physical and chemical processes. Preliminary work by different authors suggests an impact of the relative humidity of the carrier gas on the detection efficiency of particle counters. This work aims at experimentally investigating the effect of the relative humidity of the carrier gas and the instrument's temperature settings on particle activation in commonly used particle counters. Measurements of the detection efficiency using different seed particles were conducted under controlled laboratory conditions. Physical and chemical seed particle properties influencing particle activation are pointed out and the findings are set into context with well - known processes governing heterogeneous nucleation and condensational particle growth. The results of this thesis provide deeper insights into the significance of the molecular structure of working fluids used in particle detectors.

Zusammenfassung

Kondensationskernzähler sind Standardinstrumente zur Bestimmung der Anzahlkonzentration von Aerosolen. Der Anwendungsbereich dieser Instrumente wird durch den Cutoff - Durchmesser festgelegt. Die Aktivierung von Kondensationskeimen wird durch eine Vielzahl physikalisch - chemischer Parameter bestimmt. Vorausgehende Studien verschiedener Autoren legen die Vermutung nahe, dass die relative Feuchte des verwendeten Trägergases die Detektionseffizienz beeinflusst. Die vorgelegte Studie untersucht den Effekt der relativen Feuchte des Trägergases und der Temperatureinstellungen der Messgeräte auf die Partikelaktivierung. Unter Verwendung verschiedener Kondensationskeime wurden Messungen der Detektionseffizienz unter kontrollierten Bedingungen im Labor durchgeführt. Die relevanten chemischen und physikalischen Eigenschaften der Kondensationskeime werden vorgestellt und mit bereits beschriebenen Effekten, die während der heterogenen Nukleation und dem Partikelwachstum auftreten, verbunden. Die Resultate dieser Arbeit betonen die Wichtigkeit der molekularen Struktur des verwendeten Dampfes in Partikelzählern.

Contents

1 Introduction

Aerosols are omnipresent in our daily life. There are many well - known effects in our environment that are linked to aerosols, for example smog covering large cities or clouds. Furthermore aerosols affect the human body. For instance, cigarette smoke is known to have adverse health effects. On the contrary, aerosols are also used to tackle the symptoms of various diseases, for example asthma or chronic obstructive pulmonary disease. In general aerosols consist of liquid or solid particles that are suspended in a carrier gas. Particle sizes range between a few nanometers and about 100 μm. There is a large number of aerosol sources. These sources can be subdivided into anthropogenic sources, like industry, vehicle emissions or biomass combustion, and natural sources, like sea spray, volcanic eruptions, erosion or nucleation. Aerosol physics aims at understanding the processes governing aerosol properties and the interactions of aerosols in the atmosphere.

One of the biggest challenges of our era is climate change. Atmospheric aerosol also affects the Earth's climate. Global and regional climate changes are influenced by the ability of aerosols to absorb or scatter solar radiation [1]. The Intergovernmental Panel for Climate Change (IPCC) regularly assesses information concerning the current understanding of climate change [2]. Figure 1 shows a graph taken from the most recent IPCC report. It shows the radiative forcing sorted by the emitted compound. Radiative forcing is a measure for the change in the net radiative flux at the top of the atmosphere [3]. The net radiative flux is defined as the difference between the incoming and outgoing radiation.

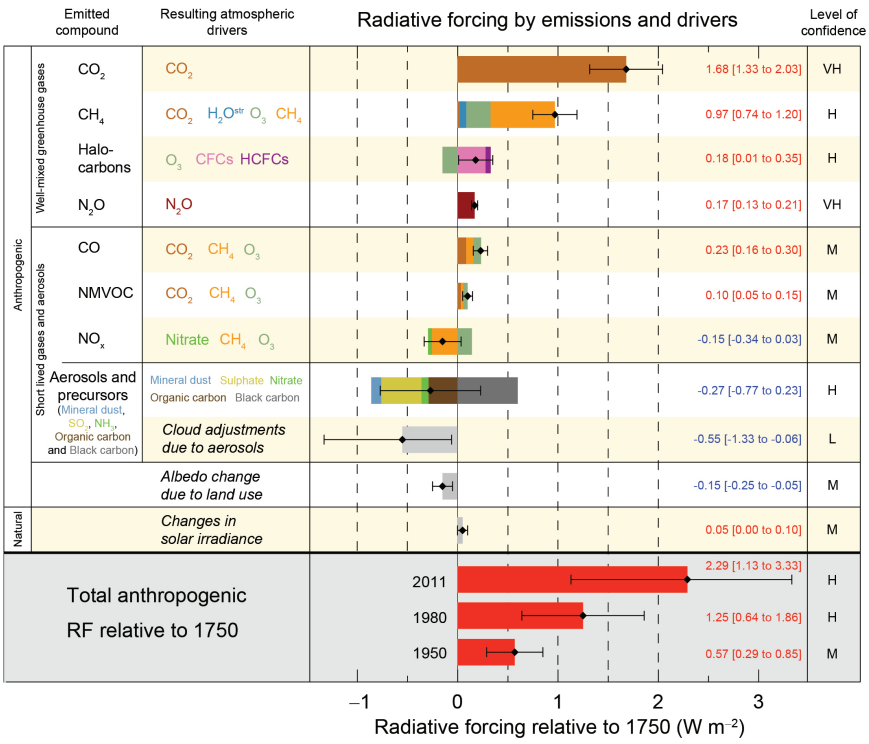

Figure 1: Anthropogenic Radiative Forcing by Emitted Compound, [4]

The report clearly states that aerosols and interactions of aerosols with clouds cause a large

portion of the global mean radiative forcing exhibiting the highest uncertainties concerning the total radiative forcing estimate [4]. As a result assessing the amount of aerosol particles in the atmosphere is of high importance.

The formation of atmospheric aerosol, the initial steps in particular, are determined by the chemistry of gaseous compounds and the concentrations of neutral and charged clusters [5]. Commonly the particle number concentration is used for monitoring aerosols. This quantity describes the number of particles within a certain volume and can be measured using Condensational Particle Counters. The first particle counter was the "Dust Counter" developed by J. Aitken in 1888 and it has been used for five decades [6]. Since then there has been a constant development of particle counters capable of measuring nanometer - sized particles.

Today, Condensational Particle Counters are widely used standard instruments in science and technology. In order to grow to detectable sizes particles have to be activated by heterogeneous nucleation. This initial step is influenced by different physical and chemical processes. The presence of ions, particle charge and the chemical nature of condensing vapors determine particle activation on the nanoscopic scale ([7] and [8]). Depending on the experimental approach, laboratory measurements under controlled conditions do not only lead to improvements concerning particle detection but also provide deeper insights into heterogeneous nucleation. By varying different parameters of commonly used particle counters the effects of the temperature settings, relative humidity, particle charge and particle shape can be analyzed. Particle counter - based measurements of different quantities are vital for improving and testing new approaches in the process of fully understanding nucleation phenomena. This thesis aims at testing the performance of state - of - the - art particle counters by varying two important physical parameters, i. e. the temperature settings of the instrument and the relative humidity of the carrier gas.

2 Nucleation

According to [9] nucleation processes are widely spread in nature and technology and play a prominent role considering condensation and evaporation. Nucleation theory is an interdisciplinary topic that is connected to thermodynamics, solid state physics, atmospheric physics and biophysics. [9]
In general nucleation refers to the initial stage of a phase transformation. In the context of aerosol physics a phase transformation from the gas phase to the liquid phase is described. D. Kashchiev introduces nucleation as the process of the random generation of nanoscopically small formations of a new phase (clusters) that have the ability to irreversibly grow to macroscopic sizes. Nucleation is the initial stage of such a phase transformation [9].
Such processes are described by the classical nucleation theory (CNT). Three important assumptions are made in this theory:

1. Clusters are spherical structures.
2. The macroscopic density is used to describe liquid clusters on the nanoscale.
3. The macroscopic surface tension is used to describe the cluster surface.

Nucleation processes are commonly examined by keeping the temperature T and pressure p constant. Therefore Gibbs free energy G is a suitable energy parameter. Gibbs free energy is given by

$$G = U + pV - TS. \tag{1}$$

U refers to the internal energy, V is the volume and S is the entropy of the system. The equilibrium state of a system is characterized using the total derivative of G,

$$dG = Vdp - SdT, \tag{2}$$

and accordingly a stable equilibrium corresponds to a minimum of G.
In general two types of nucleation are distinguished: homogeneous and heterogeneous nucleation. Homogeneous nucleation solely involves the presence of supersaturated vapor. In contrast, heterogeneous nucleation involves supersaturated vapor as well as preexisting particles. These particles are called seed particles.

2.1 Saturation Ratio

Figure 2.a represents a system consisting of a liquid and its corresponding vapor. In order to keep the temperature and the pressure constant the system is enclosed by insulated walls. Following [10] the partial vapor pressure p_v in such a system is defined as the pressure a gas would exert in a mixture of gases if it would occupy the volume all by itself. Furthermore the saturation vapor pressure p_s is defined as the pressure that maintains the mass equilibrium between the liquid and the gaseous phase at a certain temperature. [10]

The saturation ratio S is then given by

$$S = \frac{p_v}{p_s(T)}. \tag{3}$$

If just water vapor is present in such a system, the relative humidity (RH) is defined as

$$RH = \frac{p_{v,H_2O}}{p_{s,H_2O}(T)}. \tag{4}$$

The equilibrium state of the system is given by

$$p_v = p_s(T). \tag{5}$$

In equilibrium the Gibbs potential per liquid molecule μ_l equals the Gibbs potential per vapor molecule μ_v:

$$\mu_l - \mu_v = 0. \tag{6}$$

When the saturation ratio decreases below 1, the system is in the unsaturated state. Lastly, the state of supersaturation is reached when $S > 1$. In this case the partial vapor pressure is bigger than the saturation vapor pressure.

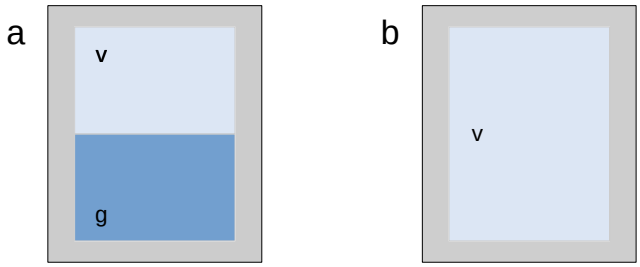

Figure 2: Exemplary Liquid - Vapor Systems: Figure 2.a shows the liquid phase and the vapor phase of a substance in a closed containment. On the contrary, Figure 2.b shows a system consisting of supersaturated vapor at a certain temperature (s. Subsection 2.2).

Experimentally supersaturation of the gas phase can be induced using three mechanisms:

- Adiabatic Expansion
- Non - Isothermal Diffusion
- Turbulent Mixing

2.2 Homogeneous Nucleation

Figure 2.b shows a schematic representation of a system containing just supersaturated vapor at a certain temperature. There is no liquid inside the container. As a result homogeneous nucleation might occur and clusters are formed. A Gibbs potential is assigned to every cluster consisting of i molecules. Nucleation is linked to the formation of a surface. This process consumes energy. The energy that is needed to form such a cluster is called nucleation work:

$$\Delta G_i = G_i - i\mu_l - ikTlnS. \tag{7}$$

k is the Boltzmann constant and "$G_i - i\mu_l$" is called excess free energy. The excess free energy is linked to the formation of a new surface and the limiting factor concerning a nucleation event. It corresponds to the energy linked to the formation of the surface of the cluster. The last term of the equation describes the change of the chemical potential of vapor molecules and liquid molecules. Due to the assumption of spherically shaped clusters a cluster radius r_i can be defined using the cluster's surface area A_i

$$A_i = 4\pi r_i^2, \tag{8}$$

and so

$$r_i = \sqrt{\frac{A_i}{4\pi}}. \tag{9}$$

The nucleation work is then given by

$$\Delta G_i = 4\pi\sigma r_i^2 - \frac{4\pi}{3} n_l r_i^3 kTlnS. \tag{10}$$

n_l describes the number of liquid molecules per unit volume and σ refers to the macroscopic surface tension of the liquid. The first term is linked to the surface of a cluster and the second term is linked to the volume of a cluster. Nucleation work therefore depends on the cluster size. Figure 3 shows the nucleation work as a function of the cluster radius. Depending on the saturation ratio there are three cases to distinguish:

1. S < 1: Due to the steady increase of the energy needed to form a cluster nucleation is inhibited. Formed clusters are not stable and decompose.

2. S $= 1$: The curve has the shape of a parabola. Nucleation is inhibited and clusters decompose.

3. S > 1: There is an energy barrier a cluster has to overcome in order to get into a stable state. The peak of the curve poses an unstable equilibrium that is characterized by the critical Gibbs energy ΔG^* and the critical cluster radius r^*.

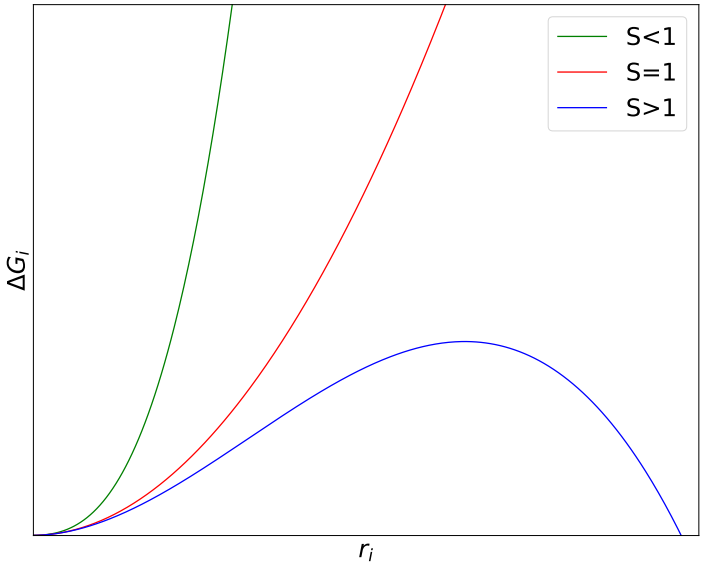

Figure 3: Schematic: Nucleation Work and Cluster Radius: The figure shows the nucleation work ΔG_i as a function of the cluster radius r_i for three different saturation ratios S. Units are arbitrary. The blue curve depicts the energy barrier a cluster has to overcome in order to reach a stable state.

2.2.1 Kelvin Equation

ΔG^* and r^* can be obtained by simple curve sketching which, after some substitutions, leads to the Kelvin equation

$$ln(S) = \frac{2\sigma}{n_l kT} \cdot \frac{1}{r^*}. \tag{11}$$

It describes the relationship between the critical cluster radius and the saturation ratio. The critical cluster radius decreases for an increasing saturation ratio. It states that the vapor pressure on the surface of a droplet with the critical radius is increased by a factor of S. Furthermore the equation states that the saturation ratio over a surface increases with a decreasing cluster radius. On basis of the Kelvin equation the critical cluster work ΔG^* can be calculated. It is given by

$$\Delta G^*_{hom} = \frac{4\pi\sigma}{3} \cdot r^{*2}. \tag{12}$$

The critical cluster work is therefore given by the surface of the critical cluster multiplied with the surface tension. The smaller the critical radius, the smaller the critical cluster work at a given saturation ratio.

2.2.2 Kinetic Approach

According to [11] the classical nucleation theory is generally based on rate equations. These rate equations account for changes of the cluster size due to the gain or the loss of molecules. It is assumed that clusters shrink and grow by acquiring or losing single molecules (called

monomers). Two further processes are excluded: cluster - cluster collision and cluster fusion. Loss and gain of molecules can be described by a linear reaction chain. The net rate I_i corresponding to an i - cluster growing into an (i+1) - cluster is given by

$$I_i = c_i \cdot n_i - e_{i+1} \cdot n_{i+1}. \tag{13}$$

c_i and e_i represent the capture rate and the evaporation rate (particles$\cdot s^{-1}$). n_i corresponds to the number concentration of i - clusters at a given time ($cm^{-3}s^{-1}$). As a result an equation for the time dependent number concentration of clusters containing i molecules can be derived:

$$\frac{dn_i}{dt} = c_{i-1} \cdot n_{i-1}(t) - e_i \cdot n_i(t) - c_i \cdot n_i(t) + e_{i-1} \cdot n_{i+1}(t) = I_{i-1}(t) - I_i(t). \tag{14}$$

Figure 4 presents a schematic for cluster growth and cluster shrinkage based on a linear reaction chain. The increase and decrease in size is neglected in this schematic. [11]

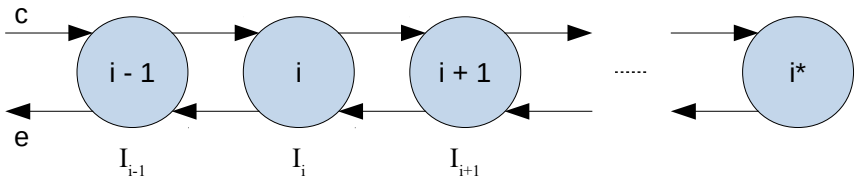

Figure 4: Schematic: Cluster Growth and Cluster Shrinkage, on basis of [11]

After some time an equilibrium is reached. This equilibrium is characterized by

$$I_i = 0 \ , \ \forall i, \tag{15}$$

and describes the equality between the capture rate and the evaporation rate. As a result all n_i are time - independent and all I_i are equal. The nucleation rate J can then be defined as the mean rate of cluster formation:

$$I_1 = I_2 = I_3 = ... = I_i = ... = I_{i^*} = J \ , \ [J] = [cm^{-3}s^{-1}]. \tag{16}$$

2.3 Heterogeneous Nucleation

The authors of [11] state that nucleation occurs homogeneously and heterogeneously in the atmosphere. Heterogeneous nucleation commonly takes place at lower supersaturations compared to homogeneous nucleation. The large amount of aerosol particles in the atmosphere provides a substrate for heterogeneous nucleation. The Kelvin equation is also valid for heterogeneous nucleation. [11]

2.3.1 Insoluble and Flat Surface

Figure 5 schematically presents the formation of a liquid embryo on the surface of a solid and insoluble seed particle. The contact angle θ is an important parameter for heterogeneous nucleation processes [12]. Generally, the nucleation work related to a flat and solid surface is given by

$$\Delta G^*_{het} = \Delta G^*_{hom} \cdot f(m), \tag{17}$$

[11]. m is called contact parameter. The exact value of the contact parameter can be calculated using the Young equation

$$m = cos(\theta) = \frac{\sigma_{sv} - \sigma_{sl}}{\sigma_{lv}}. \tag{18}$$

The indices of the surface tensions thereby refer to the phase boundaries presented in Figure 5. The function $f(m)$ is given by

$$f(m) = \frac{(2+m) \cdot (1-m)^2}{4}. \tag{19}$$

Two extrema of this function can be distinguished:

- $f(m) = 0 \rightarrow \theta = 0°$: The wettability of the surface is maximal.
- $f(m) = 1 \rightarrow \theta = 180°$: The wettability of the surface is minimal.

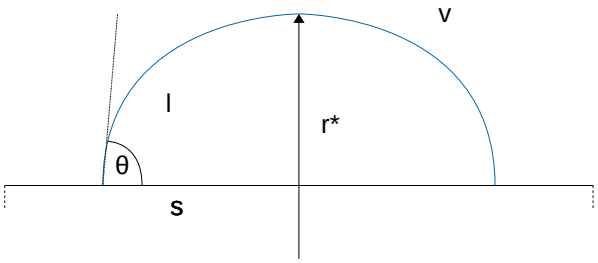

Figure 5: Schematic: Heterogeneous Nucleation on a Flat Surface: v denotes the vapor phase, s the solid phase and l refers to the liquid phase. θ denotes the contact angle; on basis of [11]

2.3.2 Insoluble and Spherical Seed Particle

Heterogeneous nucleation onto a spherical, solid and insoluble surface is described in a similar way (s. Figure 6). The critical nucleation work is given by:

$$\Delta G^*_{het} = \Delta G^*_{hom} \cdot f(m, \frac{R_p}{r^*}). \tag{20}$$

In contrast to heterogeneous nucleation on a flat surface not only the contact angle is important but also the relation of the seed particle radius R_p and the critical embryo radius r^*.

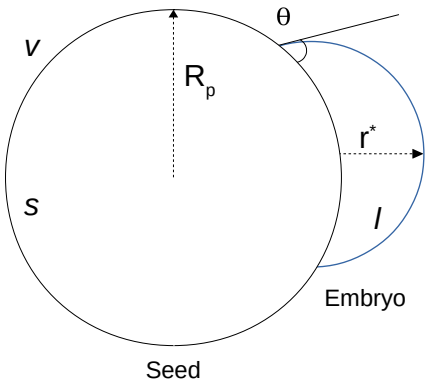

Figure 6: Schematic: Heterogeneous Nucleation on a Seed Particle: v denotes the vapor phase, s the solid phase and l refers to the liquid phase. θ denotes the contact angle; on basis of [11]

3 Experimental Methods

3.1 Particle Generation

The production of test aerosols is an important element of aerosol technology. According to [10] test aerosols are used for calibrating instruments, developing air - sampling equipment and conducting aerosol research. Thus, monodisperse aerosols are used to determine the effect of particle size on the performance of sampling devices. Most aerosol properties strongly depend on particle size and therefore monodisperse test aerosols of known size, shape and density are indispensable. Polydisperse aerosols are used to simulate the actual use of equipment under controlled laboratory conditions. As a result, a constant and reproducible output of solid aerosol particles characterizes an ideal aerosol generator. [10]
Two types of aerosol generators were used for the conducted experiments.

3.1.1 Tube Furnace

A tube furnace basically consists of a cylindrical hull with heatable walls that is placed around a glass tube. The desired particle material is put inside a small ceramic crucible, which is inserted into the tube (s. Figure 7).

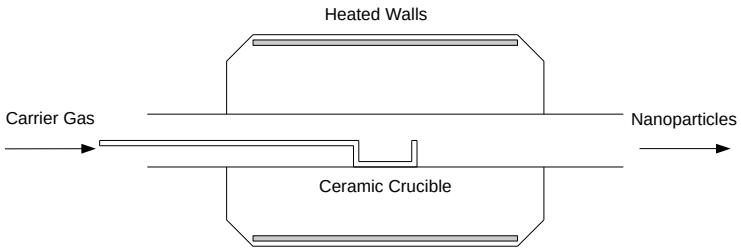

Figure 7: Schematic: Tube Furnace, based on [13]

According to [14] the aerosol material is vaporized in a carrier gas stream, for example N_2. Aerosols with number concentrations up to 10^7 particles per cm^3 are formed by homogeneous nucleation. Homogeneous nucleation and condensation occur in the cooler parts of the tube. Thereby the carrier gas stream is responsible for carrying the vaporized aerosol material into the cooler parts of the tube. [14]

3.1.2 Electrospray Ionization

In his PhD thesis G. Steiner [15] describes electrospray ionization as widely used method for the generation of well - defined nanometer - sized particles. A liquid sample is raised to a high voltage potential followed by exposure to an electric field. A surface charge is induced on the liquid. Due to the balance between surface tension and electrical forces the liquid forms out a cone. This cone is called Taylor cone. From the tip of the Taylor cone a jet of

droplets emanates. Liquid fission of the droplets occurs due to the evaporation of the solvent and singly charged ultra - fine particles or clusters are produced. [15]

3.2 Aerosol Charging

As pointed out by the authors of [16] charging nanoparticles in a defined way is important for a number of measurement techniques. In the ideal case a charging process would result in one single charge per particle. There are different approaches to particle charging. The most widely spread method is charging in a bipolar ion atmosphere. The underlying principle is diffusion charging. [16]
Following [17] bipolar diffusion charging requires the presence of positive and negative ions. The charge of a particle is increased by attaching a charge of like polarity and decreased by a charge of the opposite polarity. The rate of attachment depends on the diffusion rate of the ions and the migration in the electric field they induce. Coulombic forces lead to attraction or repulsion. Using a balanced ion population induces a quasi - steady charge state of the aerosol. The rate of attachment of positive charges equals the rate of attachment of negative charges. [17]
Figure 8 shows the schematic of a bipolar Americium - charger used for all conducted experiments. It basically consists of a conical hull that contains a stripe of radioactive ^{241}Am. The authors of [18] state that the radioactive material is embedded in a gold matrix on the strip. The activity of the source is about 60 MBq. The source is subject to an α - decay. The decay energy is about 5.5 MeV. Due to its half life of approximately two million years a decrease in the ion production can be neglected. [18]

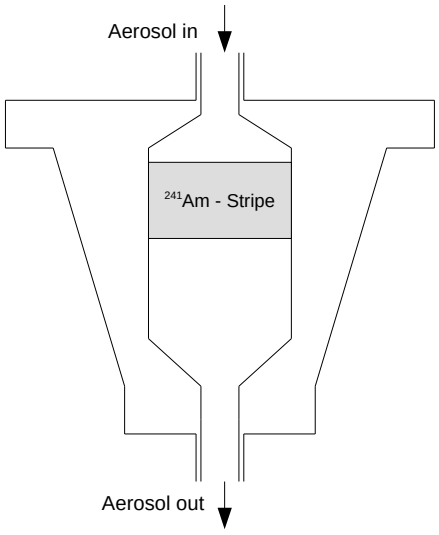

Figure 8: Schematic: ^{241}Am - Charger, based on [18]

3.3 Aerosol Classification: Differential Mobility Analyzer

The origin of the classification of particles according to their electrical mobility dates back to the 1920s [19]. Over the years improvements of the instrumentation have been developed. Today, differential mobility spectrometry is a reliable method for the determination of particle number size distributions. Additionally it can be used for the generation of monodisperse aerosols. [19]

An overview about the design and the working principle of a DMA is presented in [15]. According to the author the core component of electrical mobility measurements is the Differential Mobility Analyzer (DMA). The Vienna - type DMA is designed as a cylindrical capacitor. DMAs can be used as an analyzing device as well as a classifying device. Combined with an aerosol generator DMAs are used to classify one specific mobility band out of a broad particle distribution to serve as a source of monodisperse aerosol particles. Two groups of parameters determine the performance of a DMA: the geometry parameters and the operating conditions. The geometry parameters include R_1 (radius of inner electrode), R_2 (radius of the outer electrode) and L (axial distance between aerosol inlet and aerosol outlet). The operating conditions are characterized by the sheath air flow rate (Q_{sh}), the aerosol flow rate (Q_a), the sample flow rate (Q_s) and the excess air flow rate (Q_{ex}). Purified sheath air is introduced tangentially on the top of the instrument. Laminarization of the sheath air flow is obtained by putting a laminarization screen shortly after the air inlet. The aerosol inlet flow is fed into an annular cavity. Due to the curvature a smooth transition of the aerosol flow into the sheath air flow is guaranteed. An electric field has to be provided between the outer and the inner electrode. In order to do that a high voltage potential is applied to the inner electrode. The polarity of this potential can be positive or negative. The particles drift with respect to their electrical mobility in the direction of the electric field (radially and axially) towards an exit slit in the inner electrode. The relation between the applied voltage V and the electrical mobility Z of the particles is given by

$$Z = \frac{1}{V} \cdot \frac{ln(\frac{R_2}{R_1})}{2\pi L} \cdot \frac{(Q_{sh} + Q_{ex})}{2}. \tag{21}$$

Furthermore the electrical mobility of a spherical particle carrying i elementary charges can be expressed as

$$Z = \frac{ie_0}{3\pi\eta} \cdot \frac{\mathcal{C}(d_p)}{d_p}. \tag{22}$$

Here, d_p is the mobility equivalent diameter, η is the dynamic viscosity of the carrier gas ($\eta_{air} = 1.83 \cdot 10^{-5}$ Pa·s, 23 °C and 1013 Pa), e_0 refers to the elementary charge and $\mathcal{C}(d_p)$ is the Cunningham slip correction factor. $\mathcal{C}(d_p)$ accounts for particle sizes in the order of the mean free path of the carries gas molecules and is given by

$$\mathcal{C}(d_p) = 1 + 2.492 \cdot \left(\frac{\lambda}{d_p}\right) + 0.840 \cdot \left(\frac{\lambda}{d_p}\right) \cdot e^{-0.430 \cdot \left(\frac{\lambda}{d_p}\right)}, \tag{23}$$

[20]. λ is the mean free path of the carrier gas ($\lambda_{air} = 67.3$ nm, 23 °C and 1013 Pa). Another crucial parameter related to DMAs is the DMA resolution R. The resolution R is given by the following relation:

$$R = \frac{Q_a + Q_s}{Q_{sh} + Q_{ex}}. \tag{24}$$

Figure 9 shows a schematic of a Vienna - type DMA.

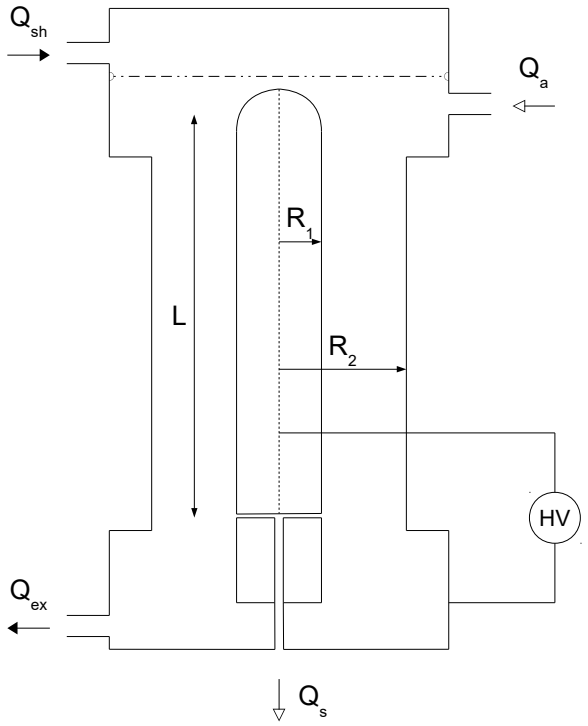

Figure 9: Schematic: Vienna - Type DMA: The geometry parameters include the radius of the inner electrode R_1, the radius of the outer electrode R_2 and the axial distance between the aerosol inlet and the aerosol outlet L. The operating conditions are given by the sheath air flow rate Q_{sh}, the aerosol flow rate Q_a, the sample flow rate Q_s and the excess air flow rate Q_{ex}; based on [15]

The UDMA used in this study is a refined version of the Vienna - type DMA design. Sheath air flow rates of about 600 lpm can be achieved resulting in an increase of the DMA's resolution. To provide such high flow rates of sheath air a special arrangement of pumps, dryers and heat exchangers has to be used. For high resolution mobility measurements well - known operating conditions have to be established. Due to the effect of the temperature of the sheath air flow on electrical mobility measurements the UDMA has to be calibrated on a daily basis. This calibration can be done by feeding aerosol particles with a known electrical mobility into the UDMA. A mobility spectrum is recorded. The voltage of a known signal

peak then corresponds to the voltage where most particles are transferred from the aerosol flow to the sample flow. Particles for calibration are generated using electrospray ionization. The actual sheath air flow rate can be determined on basis of such a calibration. [15]

3.4 Particle Detection

For the conducted measurements presented in this work two different types of particle detectors were used: detectors based on condensational particle growth (CPCs and PSMs) and detectors based on the charge carried by a particle (FCEs).

3.4.1 Faraday Cup Electrometer (FCE)

In their book P. Kulkarni et al. [17] introduce FCEs as simple electrometer - based particle detectors. Electrically charged particles can be detected. FCEs consist of a housing that contains a filter surrounded by a conducting enclosure (s. Figure 10). This enclosure acts as a Faraday cage. When charged particles pass through the Faraday cage, a charge equal to the charge carried by the particle is induced in order to isolate the electric field inside. The resulting current is measured by an electrometer. That resulting current is proportional to the particle number concentration. To ensure good performance such electrometers must not be exposed to humidity. [17]
According to [21] the electric current, that is measured by a FCE, can be split up into two components. The first component of the current consists of the signal induced by an outer source. This source are charged particles in the measured aerosol. The second component is the offset signal. The offset signal is induced by disturbances in the electrometer itself. In general the offset value is influenced by external conditions, like temperature or relative humidity. Typical offset values range between -5 fA and +5 fA. A drift in the offset value can be observed if the conditions are unstable. All measured signals are affected by the offset value. The absolute signal is altered by it, but differences between two signals are constant as long as the particle concentration is stable. [21]
The detection limit of FCE is therefore influenced by the noise occurring during measurements and the particle detection efficiency itself and, as a result, these two components are the source of uncertainty at low particle number concentrations [22]. On the other hand particle concentrations are limited by coincidence errors occurring in CPCs. It is therefore important that FCEs measure with a high signal - to - noise ratio (S/N - ratio) with low electric current measurement noise and high particle detection efficiency. [22]
Multiple particle charging is another source of measurement uncertainty. Generally, multiple charging is insignificant at small particle diameters, when methods of bipolar charging are used ([23] and [24]). Above particle diameters of approximately 30 nm the precision of the instrument is limited by multiple charging [23].

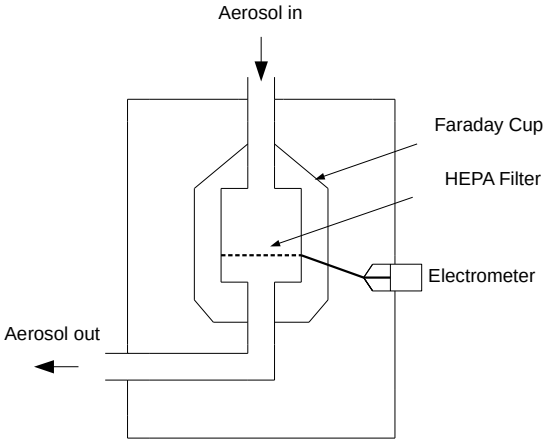

Figure 10: Schematic Figure of a Faraday Cup Electrometer, based on [25]

3.4.2 Condensation Particle Counter (CPC)

As already mentioned the particle number concentration $\mathcal{N}$ is measured using Condensation Particle Counters. The operational principle of commonly used CPCs can be divided into two steps: The first step is vapor nucleation and the second step is condensational growth of the aerosol particles. Due to condensational growth the particles can be detected optically. Every CPC consists of three main components: the saturator, the condenser and the optics block. Initially the aerosol is saturated with a condensable vapor at a certain temperature by passing through the saturator. Most saturators consist of a wick that is soaked with a working fluid. For the experiments described in this thesis only butanol - based CPCs were used. In the next step the aerosol enters the condenser. The condenser is kept at a significantly lower temperature compared to the saturator.

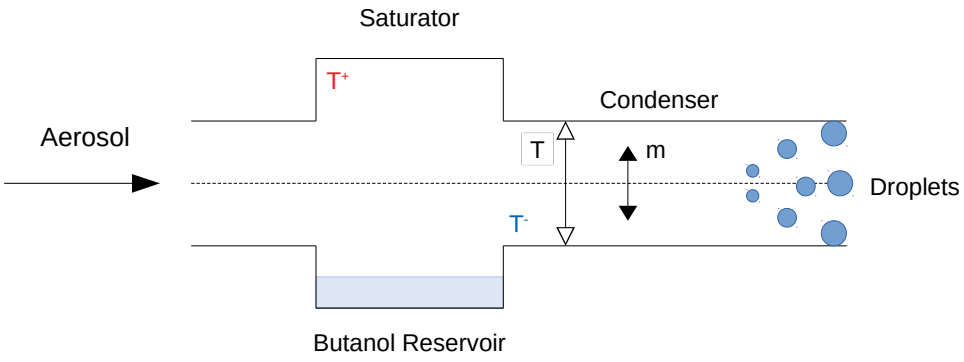

Figure 11: Schematic: Diffusion Flow Chamber: T^+ denotes the higher temperature in the saturator and T^- refers to the lower temperature in the condenser. m describes the mass of the molecules of the working fluid. Arrows depict the transport processes.

Two transport processes occur: On the one hand vapor molecules start diffusing towards the walls of the condenser. On the other hand there is a flux of heat from the warmer aerosol near the center of the condenser towards its cold walls (s. Figure 11). The butanol molecules are heavy and have high inertia. As a result heat is transfered more rapidly. Due to the Clausius - Clapeyron equation $p_s(T)$ decreases faster with decreasing temperature than p_v does. Eventually a state of supersaturation is reached (s. Equation 3). Heterogeneous nucleation occurs and the particle diameter increases due to condensational growth. The enlarged particles enter the optics block, where they are detected using a laser and a photodiode.

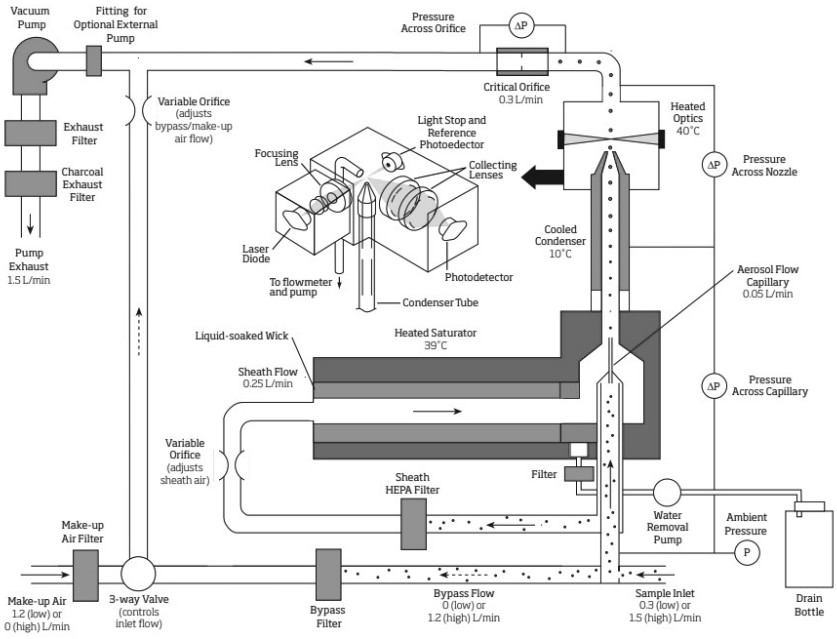

Figure 12: Layout of the TSI 3776 UCPC, [26]

A technically advanced CPC model is the TSI 3776 UCPC. Due to its specific layout the main technical characteristics are discussed in this section. Figure 12 shows a schematic representation of the CPC's layout.

According to [27] the UCPC has an inlet flow rate of 1.5 lpm (when operating in high flow - mode). This sample flow rate is then split up into 0.3 lpm of sensor flow and 1.2 lpm of bypass flow. The sensor flow is divided into 0.25 lpm of sheath flow and 0.05 lpm of capillary flow. This flow pattern is called capillary - sheath layout. Thereby the aerosol particles are confined near the centerline of the condenser. The highest saturation ratios of the n - butanol vapor can be found there. Various pressure sensors measure differences across the capillary, the critical orifice and the nozzle at the end of the capillary. [27]

Additionally the UCPC is equipped with a water - removal system. A pump removes condensed water and butanol, gathered in a condensate collection reservoir [26] .

3.4.3 Cutoff Diameter

The cutoff diameter (d_{50}) is used to describe the lower size limit of CPCs concerning particle detection [28]. Particles with diameters equal to the cutoff diameter are detected with a detection efficiency of 50 %. Using CPCs with low cutoff diameters particles can be detected right after their formation or even at the critical cluster size [29]. Following [28] the total detection efficiency of a CPC (ε_{tot}) is given by the following relation:

$$\varepsilon_{tot}(d_p) = \varepsilon_s(d_p) \cdot \varepsilon_a(d_p) \cdot \varepsilon_c(d_p). \tag{25}$$

ε_s is the sampling efficiency, ε_a is the activation efficiency and ε_c is the counting efficiency of the instrument. The sampling efficiency accounts for particle losses inside the instrument and is simply given by the ratio of the number of particles exiting the CPC and the number of particles entering the CPC. $\varepsilon_c(d_p)$ describes the efficiency of the optical system in the optics block. The saturation ratio of the condensing vapor influences the activation probability $\varepsilon_a(d_p)$. [28]

3.4.4 Particle Size Magnifier (PSM)

Particle Size Magnifiers can generally be seen as booster stages or preconditioners that are based on Diethylene glycol (DEG). For this work PSMs are used in order to obtain detection efficiency data of seed particles with diameters smaller than 4 nm (s. Section 7.2). Due to the small diameters the aforementioned UDMA is used for the measurements. According to the manufacturers the cutoff diameter of the Airmodus A10 ranges between 1.3 nm and 3.5 nm (using NiCr seeds, [30]), depending on the operating conditions (s. Section 5.1), and the cutoff diameter of the TSI 3777 is at 1.4 nm (using NaCl seeds, [31]).
Following Wimmer et al. [29] DEG can be used for the activation of aerosol particles with diameters smaller than 3 nm. Due to the low saturation vapor pressure aerosol particles grow to sizes of about 90 nm - 100 nm in such a booster stage. As a consequence, these activated particles are too small to be detected optically. A setup involving two growth stages is required: The first growth stage consists of a PSM. Particles are activated and grow to larger sizes using DEG. In a second stage these previously activated particles grow further in a commercial CPC. The actual counting of the particles takes place in this second stage. [29]
The technical characteristics of the PSM A10, manufactured by Airmodus, can be found in [32]. The saturator is surrounded by sintered stainless steel tubing. As a result no pumps are needed to soak it. Supersaturation is generated by turbulent mixing of the saturated DEG - air mixture and the aerosol. To prevent heat transfer between the saturator and the cooled aerosol inlet plastic was used for the mixing section. The mixture then enters the growth section (s. Figure 13). [32]
Figure 14 shows the flow schematic of the TSI 3777 Nano enhancer. The Nano enhancer is based on the TSI 3776 that has already been discussed in the previous section. The main

difference between the instruments is linked to the working fluid. The Nano enhancer uses DEG as a working fluid.

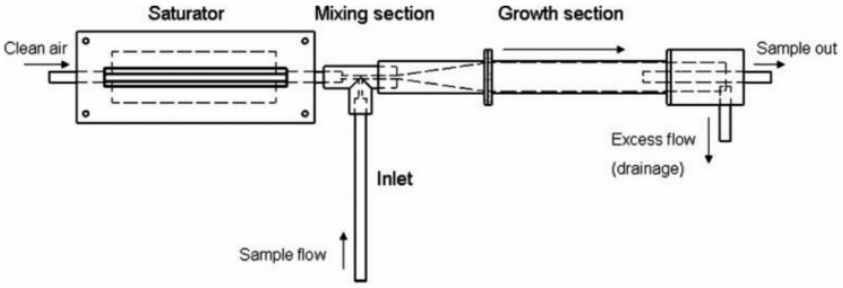

Figure 13: Schematic: PSM A10, [33]

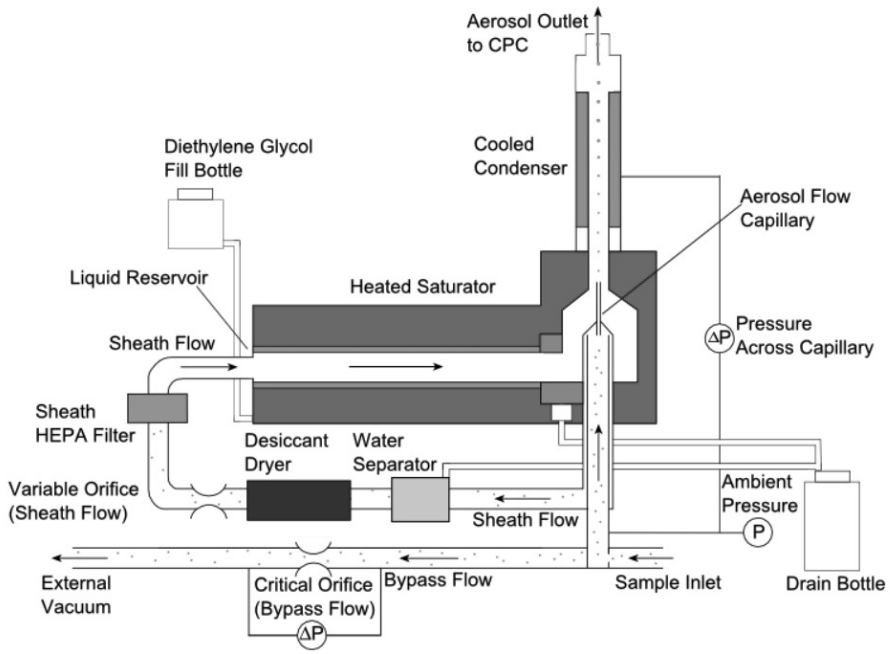

Figure 14: Layout of the TSI 3777, [31]

4 Aim of the Thesis

G. Sem published an evaluation of three different continuous - flow CPCs in 2002 [34]. The detection efficiencies of the TSI 3010, TSI 3022A and TSI 3025A. based on NaCl and Ag seeds, are presented. The diameters range from 3 nm to 100 nm and N_2 was used as carrier gas. The author reports one particular set of data corresponding to NaCl seeds and the TSI 3010 CPC that was possibly affected by the relative humidity of the carrier gas (s. Figure 15). No similar trend was found for Ag particles.

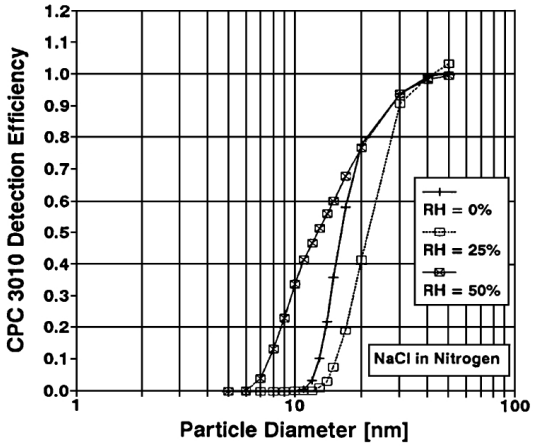

Figure 15: Possible Dependence of the Detection Efficiency on the RH of the Carrier Gas, [34]

A shift of the cutoff diameter depending on the RH of the carrier gas is visible. A relative humidity of 25 % is connected to an increased cutoff diameter. Interestingly for 50 % of RH the opposite trend can be seen. [34]

Next a publication by Schobesberger et al. [35] should be mentioned. The authors investigated the temperature dependence of the activation of NaCl and Ag seed particles. N - propanol was used as working fluid. Using NaCl seeds a deviation from the expected temperature trend, predicted by the classical nucleation theory, was found. For particles with diameters of 5.2 nm the saturation ratio necessary for their activation increased with increasing nucleation temperature. Two attempted explanations are provided. One of them states, that water contamination may have an influence on the activation of NaCl particles. However, in their study the authors could exclude this interaction due to sufficient drying of the aerosol. [35]

These two publications suggest a possible dependence of particle activation on the relative humidity of the aerosol. Accordingly the aim of this thesis was to investigate such a possible dependence in butanol - and DEG - based particle counters. The next sections explain the experimental approach and present the results.

This work was performed in close collaboration with Christian Tauber and was partly published as a discussion paper ([38] and [39]).

5 Experimental Setups and Measurement Method

5.1 Temperature - and Flow Rate Settings

The temperature difference between the saturator and the condenser of a CPC defines the supersaturation profile in the condenser [36]. The overall detection efficiency of these instruments is therefore affected by changes of the operating temperatures [37]. Figure 16 shows such a supersaturation profile in the condenser of a butanol - based CPC.

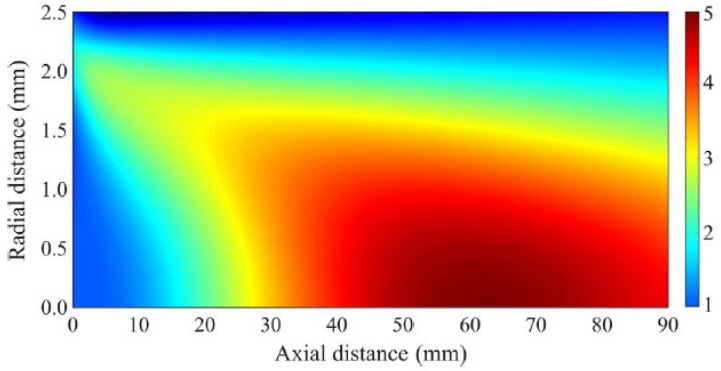

Figure 16: Exemplary Saturation Profile of a TSI 3025: The CPC was operated at a condenser temperature of 10 °C and a saturator temperature of 42 °C (ΔT = 32 °C). The origin of the coordinate system corresponds to the centerline at the beginning of the condenser tube. The radial distance describes the distance between the centerline of the condenser and the condenser walls, the axial distance refers to the length of the condenser. The color code corresponds to values of S, [37]

The same argument holds for PSMs too. Moreover, the detection efficiency of a CPC or a PSM also depends on the internal flow rates. As a result certain flow rates were altered too. The tables below present a set of temperature and flow rate settings that was used for the conducted experiments.

CPC Model	T_C [°C]	T_S [°C]	T_O [°C]	Label
3776	1.1	30.1	31.1	low T
3776	10.0	39.0	40.0	std T
3776	18.9	47.9	48.9	high T
3776	1.1	33.1	34.1	tuned
3772	22.0	39.0	40.0	std T
A20	15.0	39.0	40.0	std T

Table 1: Temperature Settings of the CPCs, [38] and [39]

T_C, T_S and T_O thereby refer to the temperatures of the condenser, the saturator and the optics block. Furthermore "std T" stands for the standard temperature settings provided

by the manufacturer. The different temperature settings of the TSI 3776 were derived empirically. Apparently, 1.1 °C is the lowest temperature the sensor in the condenser allows without showing an error. By subtracting this temperature difference also from T_S and T_O the low temperature settings were calculated resulting in a temperature difference of 8.9 °C to the standard settings. The high temperature settings are just a result of adding the same temperature difference to the standard temperature settings. Homogeneous nucleation does not occur using these temperature settings. Settings for the PSM and the Nano enhancer are listed in Tables 2 and 3. T_G describes the growth tube temperature of the PSM and Q_S refers to the saturator flow rate.

PSM Model	T_G $[°C]$	T_S $[°C]$	Q_S $[lpm]$	Label
A10	1.0	81.0	1.3	std
A10	1.0	81.0	1.1	cld

Table 2: Settings of the PSM A10

PSM Model	T_C $[°C]$	T_S $[°C]$	Label
TSI 3777	12.0	62.0	std
TSI 3777	10.0	66.0	cld

Table 3: Settings of the Nano enhancer

The label "cld" thereby refers to the settings previously used during a campaign at CERN (CLOUD experiment). For measurements involving PSMs a specially prepared UCPC (marked with a * in the schematic of the setup and referred to as tuned TSI 3776) was used. The detection efficiency of this CPC was enhanced based on [37]. The basic idea is that an increased sample flow rate minimizes particle losses. Thereby the sensor flow has to remain unchanged. Accordingly the valve controlling the make - up air flow is adjusted such, that the sample flow rate increases to 2.5 lpm (adjustment of the valve while measuring the sample flow rate with a flow meter). The valve controlling the sheath air flow has to be readjusted too. The CPC is set to modified cold temperature settings (s. tuned TSI 3776 in Table 1). As a result the aerosol flow rate of the CPC increases to about 65 cc/min. Nevertheless the flows can be adjusted such, that the CPC can be operated without displaying any error.

5.2 Seed Particles

As already mentioned two types of seed particles are used for the main experiments: NaCl and Ag particles. The NaCl particles are produced using a tube furnace. The source material is sodium chloride pro analysi manufactured by Merck KGaA (64271 Darmstadt, Germany). For the Ag particles silver wool for elemental analysis, also manufactured by Merck KGaA

(64271 Darmstadt, Germany), is used. Table 4 sums up the charging states of the particles and provides the labels that were given to them.

Material	Particle Charge	Label
NaCl	positive	NaCl(+)
NaCl	negative	NaCl(-)
NaCl	positive and neutralized	NaCl(0+)
NaCl	negative and neutralized	NaCl(0-)

Table 4: Labelling of Seed Particles (NaCl)

The silver particles are labeled following the same nomenclature. The aforementioned charges relate to the actual charging states of the particles and do not refer to the polarity of the voltage applied to the DMA. For NaCl(+) particles, for example, the voltage applied to the DMA is negative.

5.3 Butanol - Based Particle Counters

All conducted experiments can be subdivided into experiments using just butanol - based instruments and experiments involving DEG - based instruments. The setups of the different experiments are quite similar. Consequently, the setup for measurements involving butanol - based instruments and charged seed particles is discussed extensively. For similar setups only differences are pointed out.

5.3.1 Charged Seed Particles

Figure 17 shows a schematic representation of the experimental setup used for the first set of measurements of detection efficiency curves.

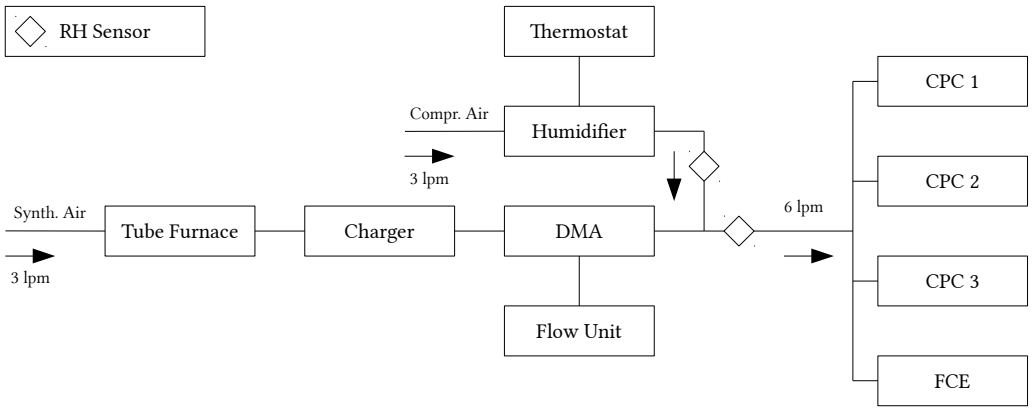

Figure 17: Setup: Humidified Carrier Gas and Charged Seed Particles

The carrier gas used to suspend the NaCl or Ag particles is a mixture of dried and compressed air and synthetic air from a gas canister (Alphagaz^{TM} 1 Air, 99.999%, $H_2O < 3.0$ ppm - mol, Air Liquide). 1.6 lpm of synthetic air are passed through the tube furnace and are mixed with 1.4 lpm of dried air between the tube furnace and the charger. The aerosol is charged using an ^{241}Am - charger. In the next step a fraction of the aerosol consisting of particles of a certain electrical mobility is selected using a nano - DMA (nDMA). The sheath air flow rate of the nDMA is 24 lpm. A flow unit maintains the sheath air flow rate and provides vacuum for the FCE. The corresponding voltages are set by a Python code executed by a Raspberry Pi single - board computer. Shortly after exiting the DMA the aerosol flow is mixed with 3 lpm of humidified air. In order to produce air of defined relative humidity, compressed and dried air is passed through a humidifier. This humidifier consists of a rectangular hull that contains up to four paper wicks. These paper wicks are soaked with purified water (HPLC Plus, CAS: 7732 - 18 - 5, Sigma - Aldrich, 3050 Spruce Street, St. Louis, MO 63103, USA). Water coming from a thermostat (Lauda Variocool VC 1200) washes around the container of the wick thereby establishing a defined saturation ratio of the air. The achieved level of relative humidity depends on the temperature of the water in the thermostat. The water temperature is adjusted manually for every measurement. Table 5 presents the approximate temperatures that have been used. Semiconductor - based RH sensors (HIH - 4000 - 004, Honeywell) are used to monitor the RH of the humidified air as well as the RH of the aerosol after the mixing. In the last part of the setup 6 lpm of humidified aerosol are distributed among three TSI 3776 UCPCs and a FCE (TSI 3068B). Every single one of these instruments is adjusted such that its sample flow rate is 1.5 lpm.

Temperature [°C]	Relative Humidity [%]
1.0	10.0
7.5	20.0
15.5	30.0
20.5	40.0

Table 5: Thermostat Settings: RH values were measured after mixing the classified aerosol with the humidified air.

The used Python program periodically applies voltage to the DMA thereby selecting aerosol particles of a certain electrical mobility. Different voltage patterns were used for different experiments. A summary of all used voltage patterns can be found in Appendix A. In general particles with diameters between 1.0 nm and 10.0 nm were selected. The program then records 90 s of background signal, which means that no voltage is applied to the DMA, followed by 90 s of active signal. Different voltages are ramped through according to this pattern. The total measurement time was about 66 minutes (based on the "d_p full range" - pattern). The signal recorded consists of the data corresponding to the two RH sensors as well as the particle number concentrations measured by the three CPCs and the FCE. Every

TSI 3776 UCPC measures 10 values of particle number concentration per second.
Whenever NaCl seed particles were generated the "d_p full range" - pattern was used. The primary size distribution of NaCl particles is broad and covers the necessary diameter region sufficiently. In this context "sufficiently" refers to particle concentrations of at least 1000 cm^{-3}. When using charged Ag seed particles the same voltage pattern as for NaCl seeds was used. However, the size distribution of Ag seeds is narrower. High concentrations are achievable but a smaller diameter region is covered. As a result it seemed better to split the voltage pattern for the measurements of neutralized Ag particles. Data referring to particles up to the size of 5.0 nm was obtained using the "d_p low range" - pattern. The "d_p high range" - pattern was used for particles with diameters bigger than 5 nm.
The last point, that should be mentioned, is linked to flow rates. Figure 17 also shows the flow rates of aerosol or carrier gas in the different sections of the setup. It is clearly visible that no overflow section is used in order to get rid of any excess flow. As a result the flow rates had to be balanced well. During a large number of tries it was noted that the shape of the measured curve improves considerably if the flow rates were adjusted such that they were marginally lower than the ones presented in the schematic (s. Section 8).
Next a sketch of the measurement procedure used for the experiments conducted on basis of positively and negatively charged seed particles is presented. The following lines briefly sum up the necessary steps:

- The seed particle material is put into the crucible and inserted into the furnace.
- The CPCs, the FCE and the tube furnace are switched on in order to warm up.
- According to the seed particle material the temperature of the oven is set to 690 °C for NaCl or to 1000 °C for Ag.
- T_C, T_S and T_O is set for every CPC.
- The HV module of the desired polarity is installed.
- If necessary the humidifier wick is wetted using HPLC grade water and the temperature of the thermostat is adjusted according to Table 5.
- The inlet flow rate of the FCE is checked using a gas meter and an offset measurement is performed.
- For the offset measurement a HEPA filter is connected to the FCE.
- The flow rate at the exit of the tube furnace is checked using two rotameters. Additionally the flows of synthetic air and compressed air have to be adjusted.
- The last step consists of checking the flow rate downstream of the humidifier and the DMA.

- Two Python programs have to be started: the DAQ program and the program controlling the voltages of the DMA.
- As soon as the measurement is finished, a data file is retrieved and named accordingly.

Using dry air as carrier gas does not require many changes (s. Figure 18). Instead of air from the humidifier simply 3 lpm of synthetic air are mixed with the aerosol exiting the DMA. The position of the two RH sensors is not changed.
This setup in a slightly modified form was also used for obtaining detection efficiency data of the TSI 3772. In order to do that one of the TSI 3776 CPCs was simply replaced by a TSI 3772. All other parts of the setup remained unchanged.

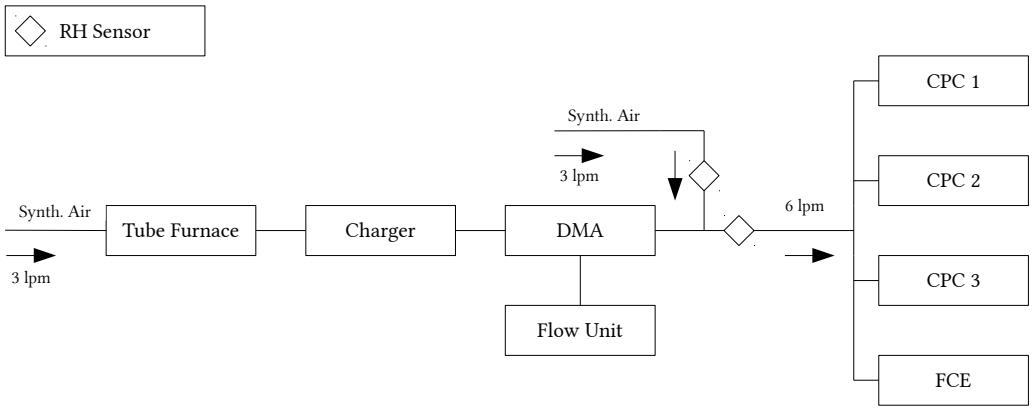

Figure 18: Setup: Dry Carrier Gas and Charged Seed Particles

5.3.2 Neutralized Seed Particles

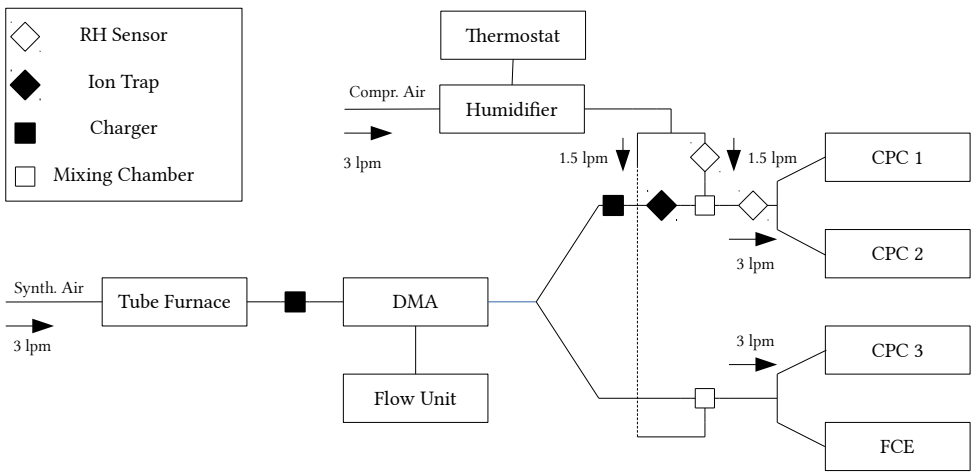

Figure 19: Setup: Humidified Carrier Gas and Neutralized Seed Particles

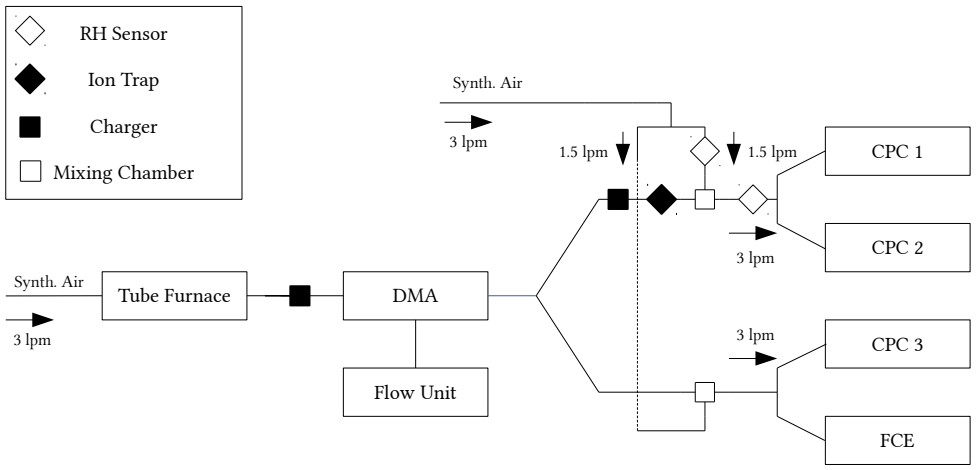

Figure 20: Setup: Dry Carrier Gas and Neutralized Seed Particles

Figure 19 and Figure 20 show the setup used for measurements involving neutralized seed particles. In contrast to measurements of charged particles the design of these setups turned out to be more challenging. An extensive period of testing was necessary to plan a setup capable of yielding reproducible results. The number concentration of charged and neutralized seed particles had to be measured simultaneously . Neutralized seed particles can be produced by simply passing the seeds through a second charger after classification. The problem is that FCEs are only capable of counting charged particles. As a result an elaborate splitting pattern of the aerosol flow had to be developed. Flow splitting quickly turned out to be a problem in this setup. Up to that point T - junctions were used to mix the dry aerosol with humidified air. The arising flow patterns were chaotic. As a result all T - junctions were replaced by mixing chambers; empty and cylindrical cavities made of aluminum. Another problem, that had to be solved, was linked to the flow rates. In order to compare the results to previously measured ones the flow rate downstream of the DMA had to be 6 lpm. In order to establish that the third CPC (CPC 3) from the previous setups is used solely as a pump.

The main differences of this setup to the previous ones are the following: The aerosol is charged and afterwards classified using the nDMA. After the DMA the flow is equally split into two branches. The first branch is connected to the FCE and the dummy CPC. Charged particles are measured. The other branch leads the aerosol through another charger that neutralizes the particles again. Additionally an ion trap is used to get rid of any residual charged particles and ions generated inside the neutralizer. The ion trap basically consists of a conductor loop wrapped around a piece of stainless steel tubing. It was sufficient to apply a voltage of ± 500 V for particle diameters up to 10 nm. Eventually the particle number concentration is determined using two UCPCs. It is crucial to apply the correct voltage polarities to the different instruments. If the detection efficiency of negative seed particles

is planned to be measured, the voltages applied to the UDMA and to the ion trap need to be positive (and vice versa).
Accordingly the measurement procedure is very similar to the procedure described in the previous section. The only minor difference is related to the ion trap, that needs to be switched on along all other instruments.

5.4 DEG - Based Particle Counters

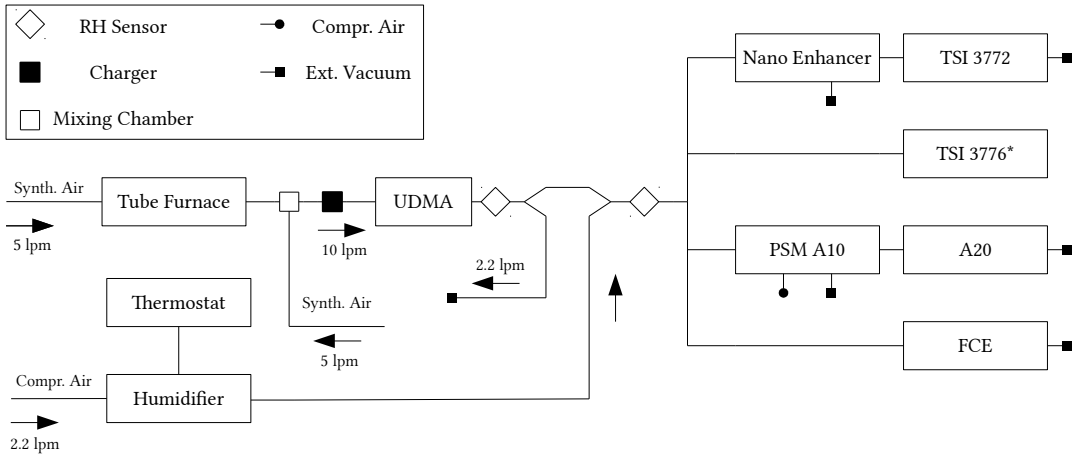

Figure 21: Humidified Carrier Gas and Charged Seed Particles

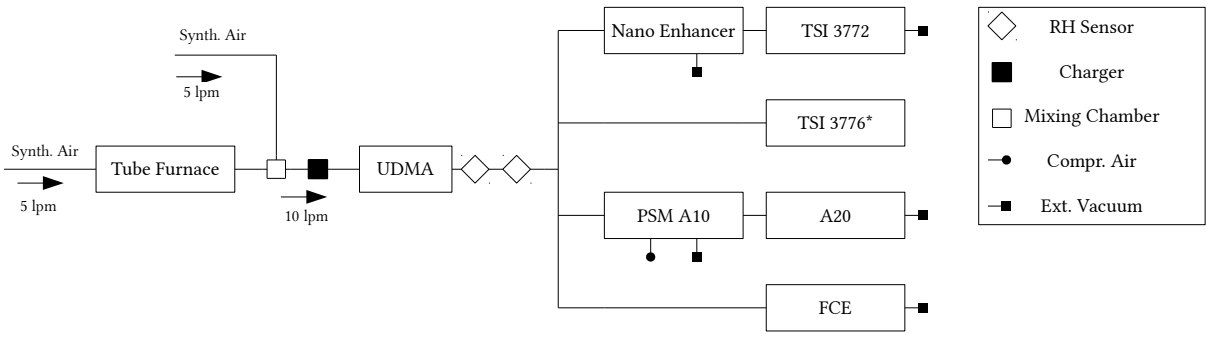

Figure 22: Setup: Dry Carrier Gas and Charged Seed Particles

Figure 22 and Figure 21 show the setup used for the measurements of the detection efficiencies involving PSMs. The resolution of a DMA depends on four different flow rates (s. Equation 24). Accordingly, the combined aerosol flow rate was increased to 10 lpm. Again a mixing chamber was used in order to combine 5 lpm of aerosol and 5 lpm of dried (or humidified)

carrier gas. In order to establish comparable conditions considering the experiments using butanol - based particle counter, the dry aerosol had to be classified by the UDMA. Due to the desired DMA resolution a sample flow rate of 10 lpm had to be used. The summed up inlet flow rates of all particle counters upstream of the second RH sensor was 10 lpm as well. In order to mix the aerosol with humidified air 2.2 lpm of classified aerosol was removed using a pump in the section between the two RH sensors. 2.2 lpm of humidified air were mixed in again to adjust the RH of the carrier gas to 10 %. For a relative humidity of40 % these two flow rates were increased to 4.5 lpm. Two Y - junctions were used to establish proper flow conditions. For the measurements involving dried carrier gas, both RH sensors were placed next to each other in order to use a a setup that was comparable to the setup used for the humidified carrier gas. The temperature of the thermostat was adjusted according to Table 5 again. The tuned TSI 3776 UCPC was used for the first time in this setup. These measurements were just conducted for charged seed particles and carrier gas humidities of 0 %, 10 % and 40 %. The following procedure was used:

- All instruments are turned on and the flow rates are adjusted.
- Additionally the vent of the UDMA has to be switched on and the blower is set to 5.
- While all other instruments are warming up, the UDMA is flushed with dried and compressed air ($\approx$ 1 bar).
- The desired settings are set for every instrument and an offset measurement of the FCE is performed.
- After about 10 minutes of UDMA flushing the UDMA is quickly connected to the mixing chamber.
- The overall RH downstream of the UDMA must not exceed 2 %, else the flushing has to be repeated.
- The DAQ program is started.

The reconnecting of the UDMA after flushing it appeared to be tricky. This step was repeated frequently until a proper measurement could be started. Special care has to be taken of the PSM. Before any measurements can be done the instrument has to be drained and primed in order to establish correct working conditions.

5.4.1 Calibration of the UDMA

At the beginning or at the end of every measurement day the UDMA has to be calibrated. As a result the blower settings must not be changed during a measurement sequence. Figure 23 schematically shows the setup for the UDMA calibration. For the calibration a solution of tetraheptylammonium bromide (THABr) in acetonitrile (1 mMol/l) is used. As a solvent

HPLC grade acetonitrile is used (CAS: 75 - 05 - 8, Sigma - Aldrich) to dissolve THABr (purum, EC No.: 2244593, Sigma - Aldrich). Using a syringe the solution is pumped through a capillary into the electrospray chamber. The chamber is connected to the UDMA and flushed with 15 lpm of compressed and dried air. A FCE detects particles downstream of the UDMA.

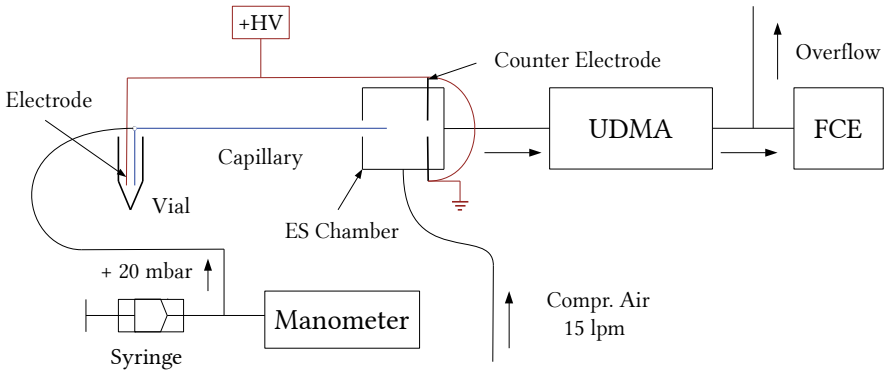

Figure 23: Setup for Calibration of the UDMA: A positive HV potential (1300 V) is applied between an electrode in the vial and a counter electrode inside of the ES chamber. The THABr solution is pushed through a capillary into the ES chamber using a syringe. The pressure applied to the capillary is monitored using a manometer. Compressed air is used to suspend the particles and carry them into the UDMA. The blue lines depict the capillary; red lines describe electrical connections.

The following procedure is used for the calibration of the UDMA:

- The THABr solution is prepared (s. Appendix B).
- Six empty vials including lids are prepared. Four of them are filled with one pipette tip of acetonitrile. One is kept empty as encasing for the wires and one is filled with one pipette tip of THABr solution.
- The chamber is flushed with 15 lpm of compressed and dried air and an acetonitrile vial is mounted.
- A syringe is used to flush the capillary.
- The liquid is pushed into the capillary with approximately 200 mbar. Afterwards it is sucked out with 80 mbar again.
- The process is repeated.
- A second vial is attached and the capillary is flushed again.
- After cleaning the vial containing the THABr solution is mounted and a pressure of 20 mbar is applied.

- A voltage of 1350 V is applied resulting in a current of approximately 100 nA.
- The solution is sprayed positively and therefore the UDMA voltage has to be negative.
- The program, that records the spectrum, is called "DC10DAQCPFnegV" and needs to be started.
- The FCE's offset is adjusted such, that the voltages corresponding to the three channels are about the same.
- A spectrum is recorded. The UDMA can be calibrated using the monomer peak (s. Section 6).

During all experiments the flow rates are checked using the Gilian Gilibrator - 2 (Serial Nr.: 1312041) or the TSI Series 4000 Flowmeter (Serial Nr.: 414006008007).

6 Data Analysis

The principal approach to data analysis depends on the used instruments. In general a separate file of raw data is created for every single measurement. These data files contain a time stamp and a certain number of particle number concentrations measured using CPCs and the FCE. Due to different voltage patterns and the used software the analysis of nDMA related data differs from the analysis of data obtained using the UDMA.

6.1 Raw Data

CPCs manufactured by TSI measure ten values of $\mathcal{N}$ every second. Data of the TSI CPCs is therefore averaged over every second. Eventually the particle number concentration can be plotted against time (s. Figure 24).

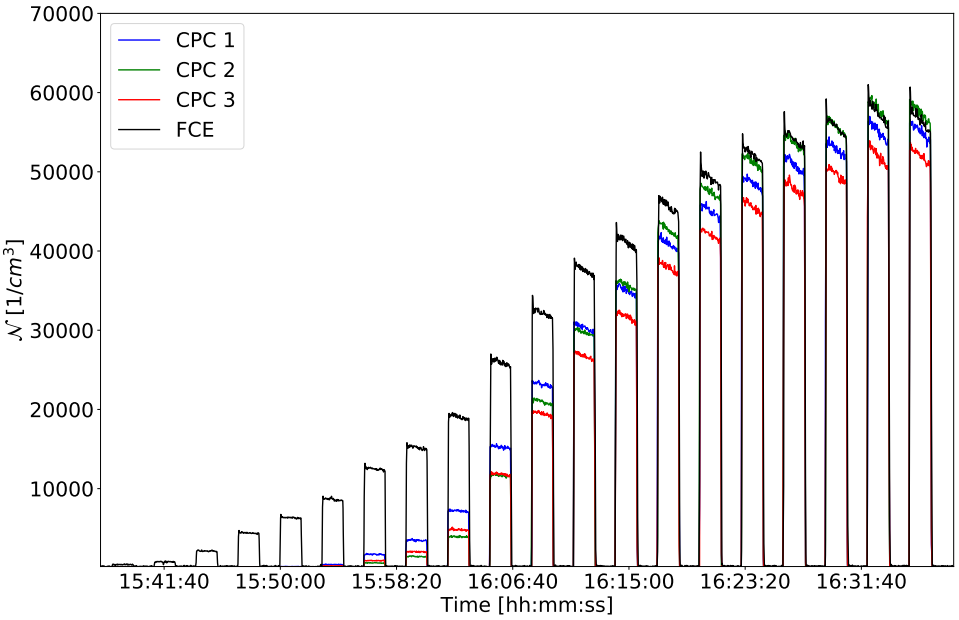

Figure 24: Exemplary Spectrum (RH=(0±2)%, NaCl(-), std T)

The lines in the graph connect a large number of measured particle number concentrations. The next step of data analysis consists of averaging data over the time intervals. A Python code is written that divides the measurement into subintervals. The time series is split into periods of background measurement and periods of active DMA classification. In the case of the measurements of charged particles the measurement is subdivided into 44 intervals. The particle number concentrations in every interval is then averaged again. Eventually there is one single value of $\mathcal{N}$ for every interval and every instrument. Applying voltage to the DMA sometimes produces a spike. Consequently, a few seconds at the beginning and the end of an interval are neglected.

6.2 Detection Efficiency and Cutoff Diameter

The detection efficiency of every CPC is calculated using

$$\varepsilon = \frac{\mathcal{N}_{CPC}}{\mathcal{N}_{FCE}}. \tag{26}$$

These calculations yield one value of ε for every selected particle diameter (corresponding to a specific DMA voltage). In order to obtain a cutoff curve the detection efficiency is plot against the particle diameter. Figure 25 shows such a cutoff curve.

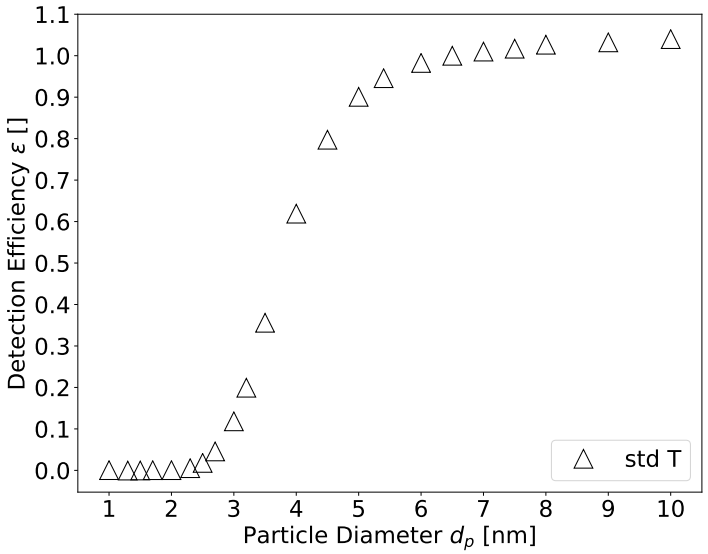

Figure 25: Exemplary Cutoff Curve (RH=(10±2)%, NaCl(+), std T): The detection efficiency of a CPC (according to Equation 26) is plotted against the seed particle diameter. The cutoff diameter is (3.82 ± 0.31) nm.

Different functions are used to fit the data:

- Wiedensohler Fit:

$$y = \frac{a - b}{1 + e^{\frac{x - x_1}{x_2}}} \tag{27}$$

- Hyperbolic Fit:

$$y = \frac{a \cdot (x - x_0)}{b + (x - x_0)} \tag{28}$$

- Empirical Fit:

$$y = a \cdot e^{-e^{-k \cdot (x - x_0)}} \cdot \left(1 - e^{(-x \cdot n)}\right) \tag{29}$$

As usual x is the independent variable and y is the value of the functions at x. All other constants are minimized. Wiedensohler's fit [40] was the standard approach to data fitting. Unfortunately this function could not always be used due to irregular curve shapes (s. Section

7). The last choice was to use the empirical function. This empirical function can be adjusted to different curve shapes. Table 6 presents the tunable parameters and their impact on the fit function's shape.

Parameter	Linked to	Range
a	Position of the Plateau	0.8 - 1.3
k	Curvature	6 - 9
x_0	Offset	2
n	nth root function	0.5

Table 6: Parameters of the Empirical Fit Function

Based on the fit data the cutoff diameter is calculated. A simple curve fitting algorithm determines the cutoff diameter of every CPC. The last step of data analysis consists of plotting the cutoff diameter against the relative humidity of the carrier gas.

6.3 Uncertainties

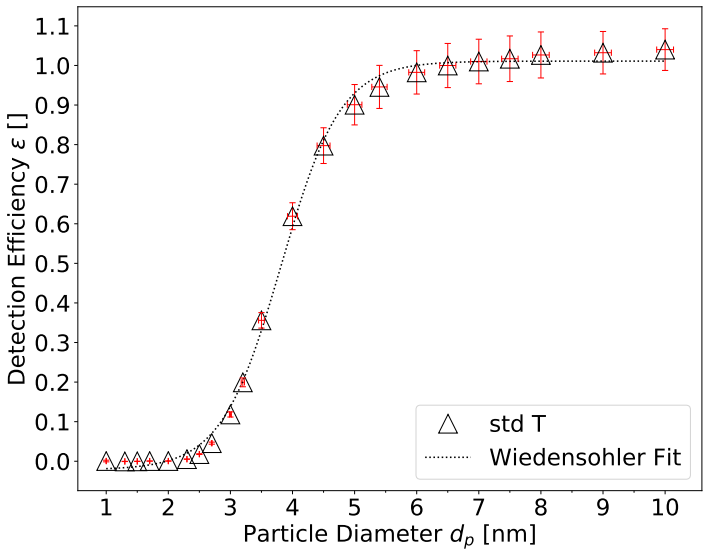

Figure 26: Exemplary Cutoff Curve (RH=(10±2)%, NaCl(+), std T): The figure shows a fully analyzed cutoff curve. Data points are fitted using Wiedensohler's fit in order to calculate the cutoff diameter. Error bars are added.

In general the uncertainties of the experimental data are calculated using mean values and standard deviations or Gaussian error propagation (using [41]). Considering the detection efficiency curves the uncertainties of the mean values of $\mathcal{N}$ have been calculated using both methods. It turned out that the standard deviations are lager than the uncertainties arising from Gaussian error propagation. As a result standard deviations were used, but starting

from the splitting of the intervals solely Gaussian error propagation was used.
Some detection efficiency curves have been measured using two or more CPCs with the same temperature settings. Thus, a maximum uncertainty could be calculated referring to different identically constructed CPCs. These maximum uncertainties were only used for charged and neutralized particle measurements. The uncertainties of the diameters in the plots are calculated using the DMA resolution (s. Equation 24). Figure 26 presents a fully analyzed detection efficiency curve. Table 7 sums up the uncertainties of the used instruments.

Instrument	Uncertainty of	Uncertainty [%]
all CPCs	$\mathcal{N}$	10.0
FCE	$\mathcal{N}$	5.0
Gilibrator - 2 Flowmeter	Flow Rate Q	1.0
TSI Series 4000 Flowmeter	Flow Rate Q	2.0

Table 7: Uncertainties of used Instruments, ([26], [42], [43], [44])

6.4 Dilution Factors of the PSMs

The analysis of the PSM related data is different. First, the averaging of the data has to be done in a similar way. The only difference is that the Airmodus CPC just records a single value of $\mathcal{N}$ per second. Furthermore there are correction factors f linked to the use of PSMs. These correction factors account for the different flow rates in a PSM / CPC - combination and are used to correct the measured particle number concentrations.
According to [31] the correction factor for the TSI 3777 / TSI 3772 - combination is given by the following relation:

$$f_{NE} = \frac{Q_{in,CPC}}{Q_{in,NE}} \approx 6.67, \tag{30}$$

where Q_{in} refers to the inlet flow rates. This factor can be seen as a constant due to the fact, that the inlet flow rate of the Nano enhancer has never been altered during the experiments. The correction for the PSM A10 is more complex. According to the user manual the correction factor for the A10 / A20 - combination can be expressed as

$$f_{A10} = \frac{Q_{in} + Q_S}{Q_{in}} \approx (1.3 \ldots 1.5), \tag{31}$$

[45].The saturator flow rate of the PSM A10 has been altered during the experiments.

6.5 UDMA Calibration based on the Monomer Peak

Figure 27 shows the raw data of the UDMA calibrations. Raw data consist of a spectrum with the DMA voltages on the abscissa and the particle number concentrations on the ordinate. The first peak at approximately 500 V corresponds to the THABr - monomer. This peak is used for the calibration. The peak position V_p is read out manually.

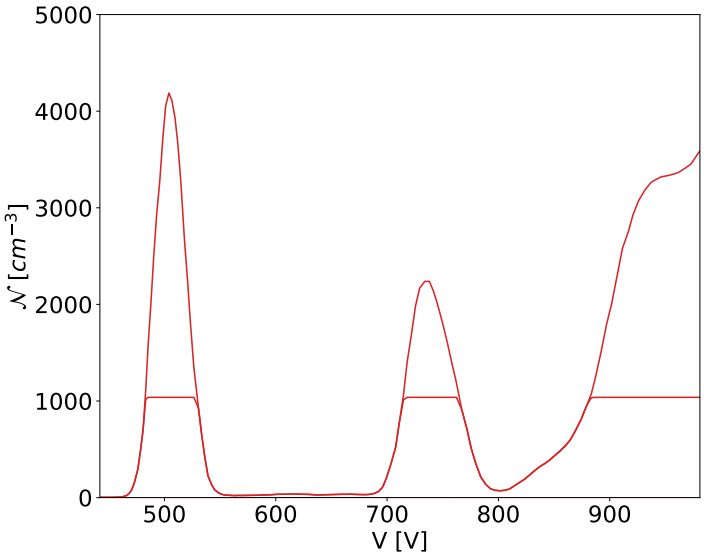

Figure 27: Exemplary UDMA Spectrum (18.05.2018): The spectrum shows the monomer peak at about 500 V and the dimer peak at approximately 750 V. The position of the monomer peak is used for the calibration of the UDMA.

The following constants are used for the related calculations:

Constant	Symbol	Value	Source
Inner Diameter (UDMA)	R_1	0.0175 m	[15]
Outer Diameter (UDMA)	R_2	0.0240 m	[15]
UDMA Length	L	0.0065 m	[15]
Electrical Mobility of THABr(+)	D	0.9709 $cm^2(Vs)^{-1}$	[46]

Table 8: UDMA Calibration: Used Constants

The following calculations can be found in [15]:
Let K be the DMA's characterization factor. K depends on R_1, R_2, L and Q_{sh}. The following relation holds:

$$K = Z \cdot V \quad \rightarrow \quad K = D \cdot V_p. \tag{32}$$

The sequence of the voltages applied to the UDMA shall be referred to as V_U. K can be calculated. By knowing K the inverse electrical mobility of the particles Z_n^{-1} can be calculated using V_U. Thus,

$$Z_n^{-1} = \frac{V_U}{K}. \tag{33}$$

n is the number of entries in V_U. An approximation is used to recalculate the mobility equivalent diameters [47]:

$$d_p = \sqrt{2.01 \cdot Z_n^{-1}}. \tag{34}$$

Eventually a series of voltages and particle diameters is obtained. Additionally the sheath

flow rate of the UDMA is calculated using Equation 21.
All uncertainties linked to the UDMA calibration and the calculation of the sheath flow rate are assumed to vanish. Again the resolution R of the UDMA is used for the calculation of the uncertainties of the measured cutoff diameters.

7 Results and Discussion

The following section contains detection efficiency curves as well as their interpretations. For the sake of comprehensibility and readability the error bars are removed. More than one detection efficiency curve has been measured for every set of instrument settings, relative humidity and seed particles. Only one curve for every set is presented in this section. The summarizing plots at the end of every subsection are based on all performed measurements (e. g. Figure 48). A summary of the used instruments, the calculated cutoff diameters, the minimal and maximal seed particle concentrations and the UDMA sheath flow rates can be found in Appendix C, Appendix D, Appendix E and Appendix F.

7.1 CPC - Based Measurements

The following figures show the results of the measurements using charged and neutralized NaCl and Ag seeds. Three TSI 3776 UCPCs and a TSI 3068B FCE were used in parallel to determine the particle number concentrations. During the measurements using charged seeds all four instruments were involved in data acquisition. In order to obtain the results shown in Section 7.1.4 one of the UCPCs was replaced by a TSI 3772 CPC. Only two UCPCs and the FCE were actively measuring during the experiments using neutralized seed particles. One UCPC was used solely as pump (s. Figure 19).

7.1.1 Counting Efficiencies of Charged Seed Particles

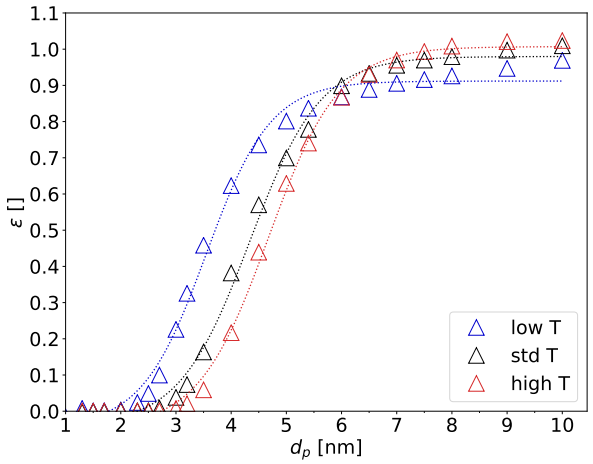

Figure 28: RH=(0±2)%, NaCl(+)

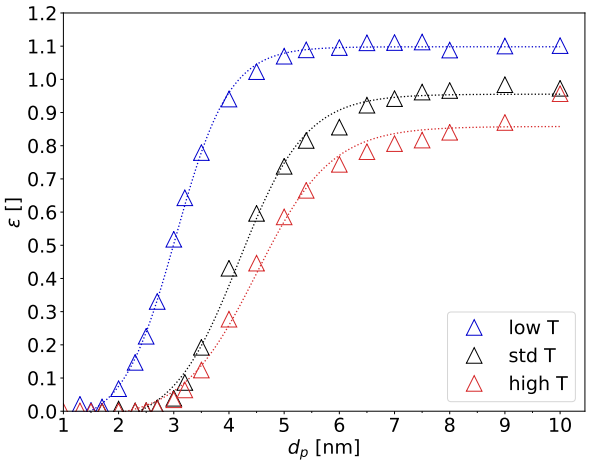

Figure 29: RH=(0±2)%, NaCl(-)

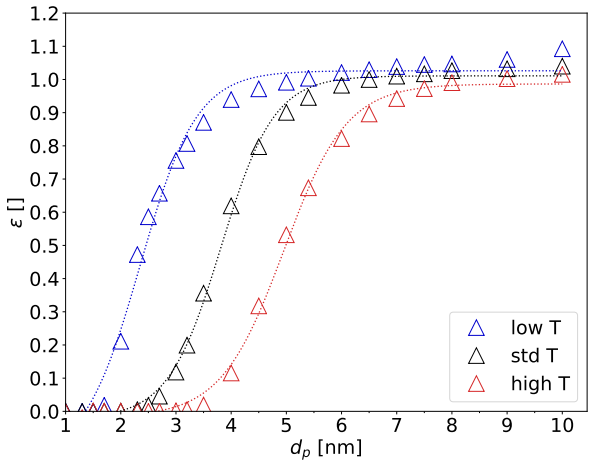

Figure 30: RH=(10±2) %, NaCl(+)

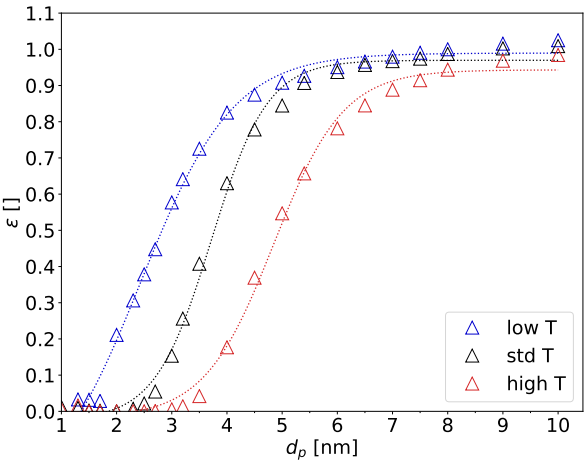

Figure 31: RH=(10±2)%, NaCl(-)

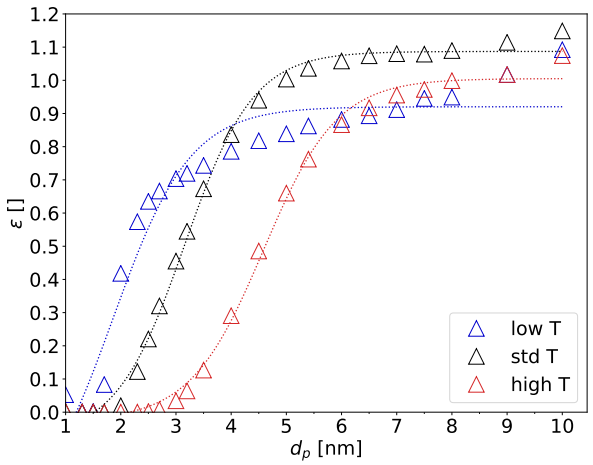

Figure 32: RH=(20±2)%, NaCl(+)

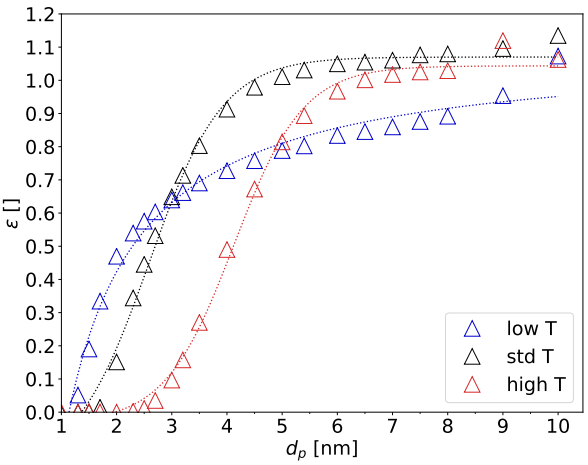

Figure 33: RH=(20±2)%, NaCl(-)

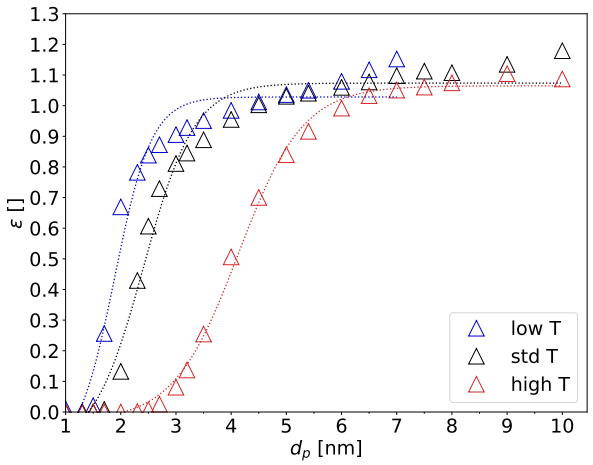

Figure 34: RH=(30±2)%, NaCl(+)

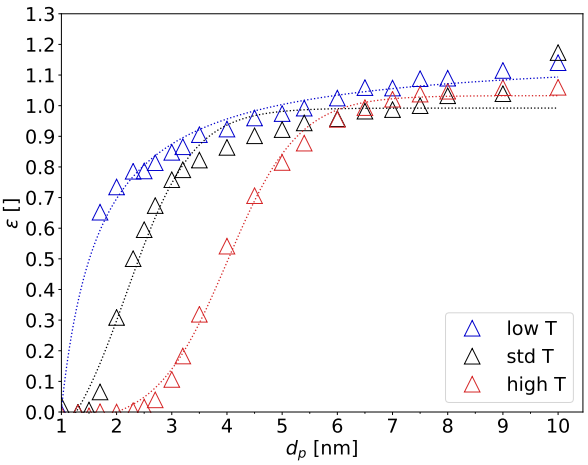

Figure 35: RH=(30±2)%, NaCl(-)

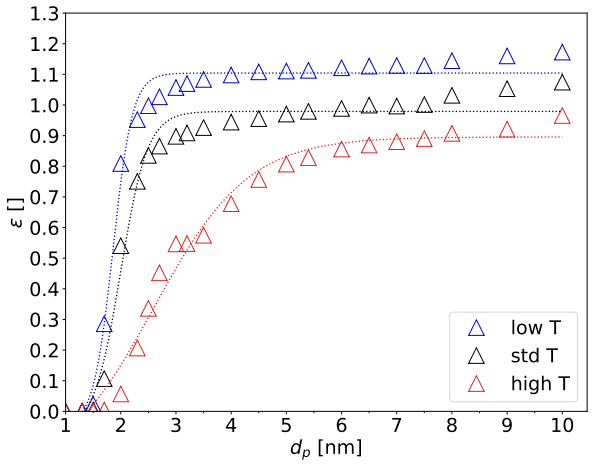

Figure 36: RH=(40±2)%, NaCl(+)

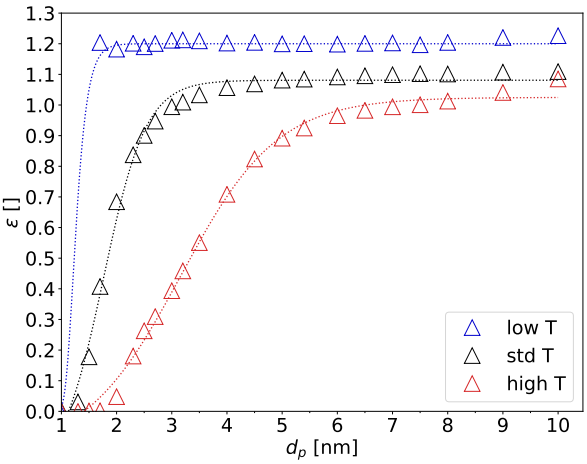

Figure 37: RH=(40±2)%, NaCl(-)

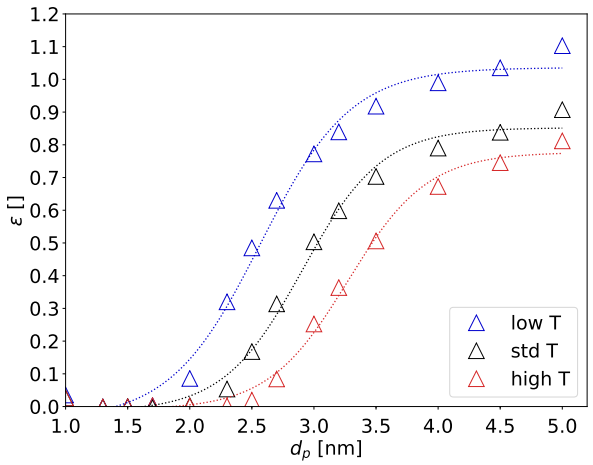

Figure 38: RH=(0±2)%, Ag(+)

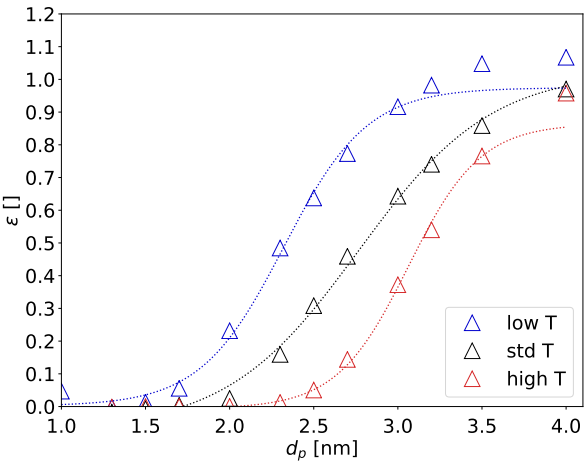

Figure 39: RH=(0±2)%, Ag(-)

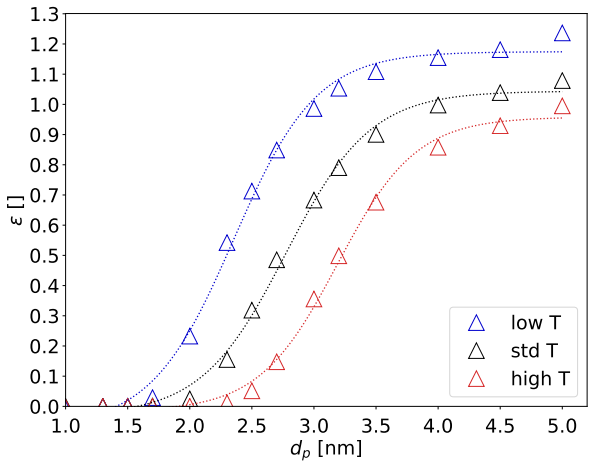

Figure 40: RH=(10±2)%, Ag(+)

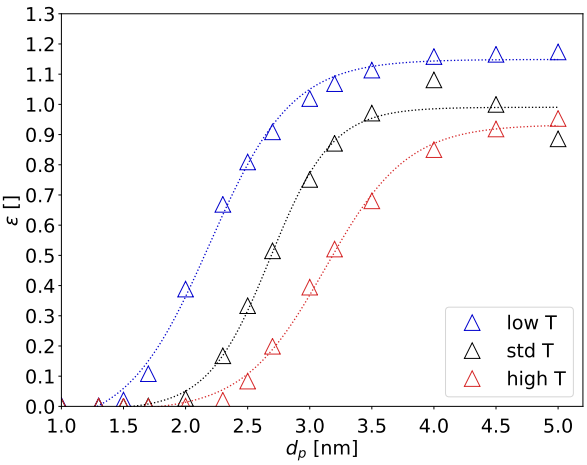

Figure 41: RH=(10±2)%, Ag(-)

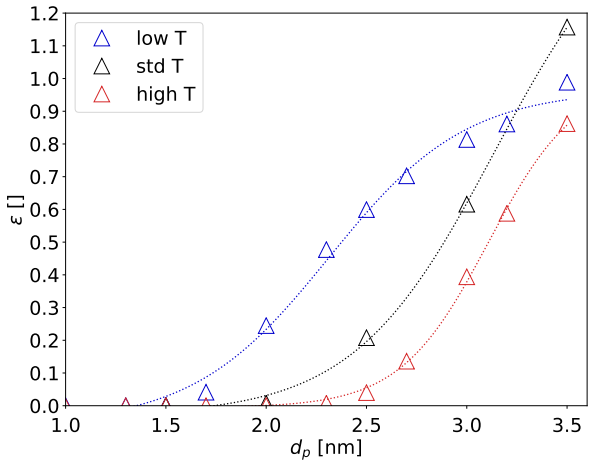

Figure 42: RH=(20±2)%, Ag(+)

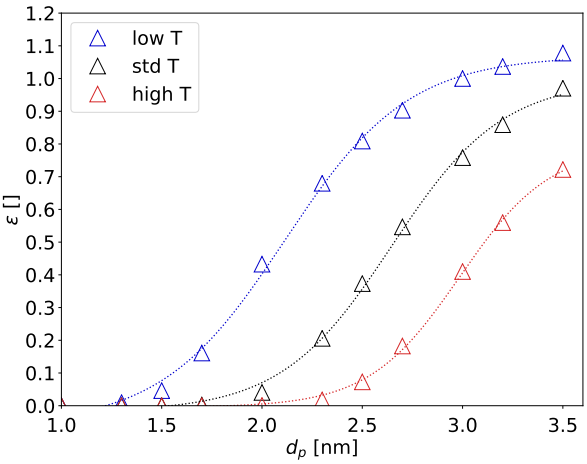

Figure 43: RH=(20±2)%, Ag(-)

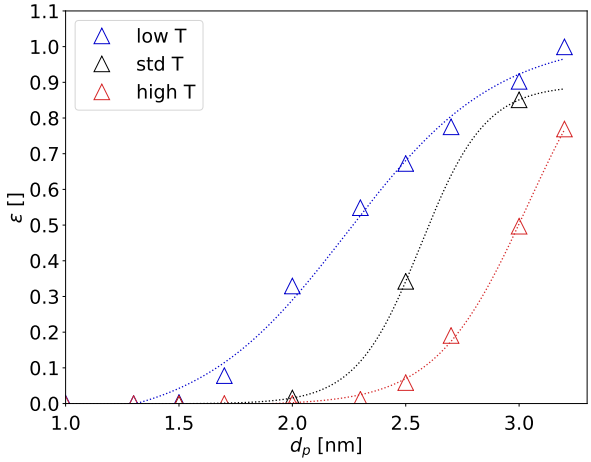

Figure 44: RH=(30±2)%, Ag(+)

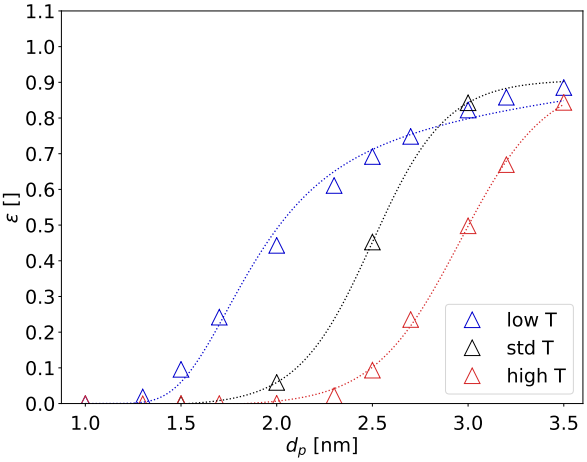

Figure 45: RH=(30±2)%, Ag(-)

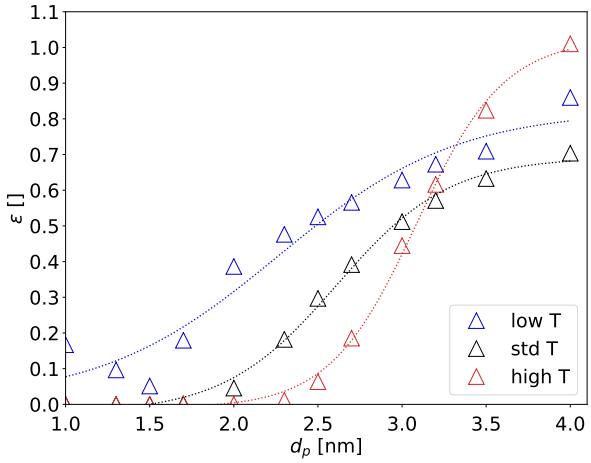

Figure 46: RH=(40±2)%, Ag(+)

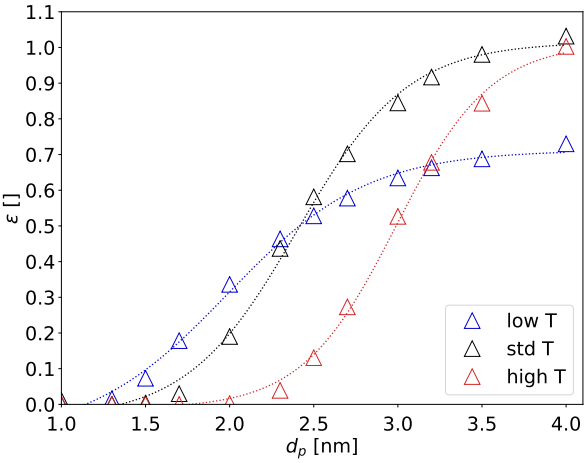

Figure 47: RH=(40±2)%, Ag(-)

7.1.2 Cutoff Diameters of Charged Seeds

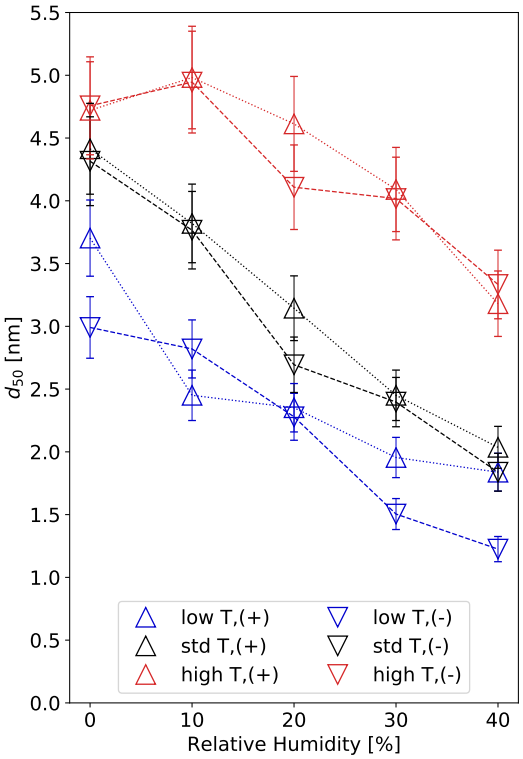

Figure 48: Cutoff Diameters of NaCl Seeds, [38] and [39]

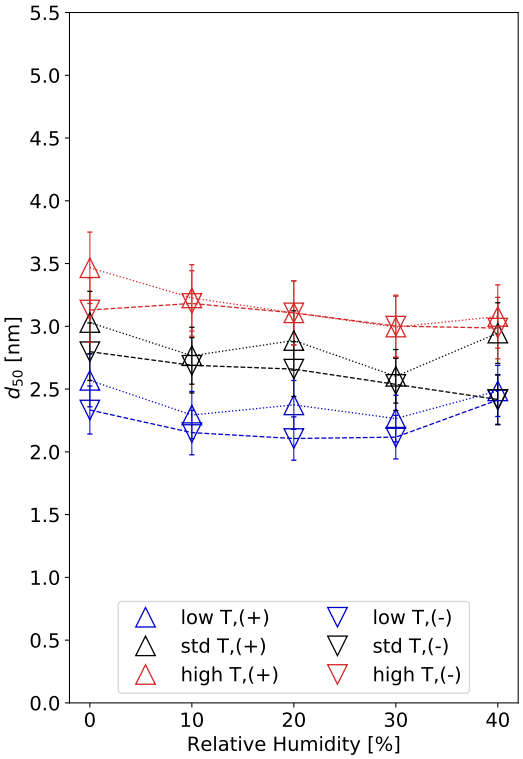

Figure 49: Cutoff Diameters of Ag Seeds, [38] and [39]

7.1.3 Discussion of the Results 1

Generally it is important that the measured curves look like the curve in Figure 25. Information concerning particle activation can be retrieved from the curve's shape. In order to get maximum information the curves should be complete. A complete detection efficiency curve consists of three parts: the starting point of the curve ($\varepsilon = 0$), its slope (including $\varepsilon = 0.5$) and its plateau ($\varepsilon = max$). The overall curve shape yields information about the instrument's performance. In the case of NaCl seeds all recorded curves are complete. In contrast some of the Ag curves miss important parts. The main problem is that there are curves presenting themselves without plateaus (s. Figure 42, Figure 44 and Figure 45). The concentrations of Ag particles produced in the tube furnace are higher compared to the concentration of NaCl particles. Nevertheless the overall distribution of particle sizes is narrow. As a result curves should be recorded using two tube furnace temperatures, one for low diameters and one for larger diameters. Initially the concentrations of Ag particles seemed sufficient for all diameters between 1 nm and 10 nm at a single temperature. Data analysis revealed the opposite. The experimental approach of just using one single temperature of the tube furnace yielded data, that could not be used entirely. Only data corresponding to seed particle diameters up to approximately 4 nm yielded proper values for the detection efficiency. For larger diameters the signal deteriorated due to very poor seed particle

concentrations and could not be distinguished from the background signal anymore. The diameter at which data deterioration starts can easily be determined by taking a look at the recorded spectra (s. Figure 24). Due to the poor S/N - ratio these parts of the curves were cut away. The analysis of such data does not yield proper, reliable and reproducible values for the detection efficiency. Summing up, using just a single temperature setting of the tube furnace for Ag seed particles is a systematic measurement error that can be not corrected during data analysis. Nevertheless all of these curves include at least the cutoff diameter. As a result they can still be used for further analysis as well as for the overall data interpretation.

In order to address and further verify the aforementioned issues some curves were measured using two CPCs with the same temperature settings. The first measurements using neutralized seed particles were performed just using one single UCPC. Again, a CPC - characteristic activation behaviour related to the preset aerosol flow rate of the particle counter could be seen. Additionally every single detection efficiency curve was measured more than once. The figures in this section only show one curve for every combination of temperature settings, relative humidity and seed particles.

The next eye - catching structures are the different plateau shapes. One would expect a flat shape that can clearly be distinguished from the slope of the curve (s. Figure 28). Obviously some of the curves exhibit different plateau shapes. The shape of the plateau and its transition to the slope of the detection efficiency curve are connected to the flow rates in the setup. As a rough estimate it can be stated that a differing plateau shape is a hint for unbalanced flows. As already stated in previous sections, the inlet flow rates of the CPCs vary. After some measurements one could clearly see that these variations lead to flattened curve shapes (s. low temperature curves in Figure 33 and Figure 35, as well as the standard temperature curve in Figure 35 and the high temperature curves in Figure 36 and Figure 37). In the case of Ag seeds these flattened curve shapes cannot only be attributed to the overall flow rate patterns in the setup. The previously mentioned issues with the size distribution need to be taken into account too. As a result it is very difficult to interpret these curves concerning flow rate patterns. Most certainly a combination of both problems influenced the curve shapes for Ag seed particles. It has been found that very small deviations from the theoretical flow rates of the CPCs have an immense effect on the curve shapes. Flow rate deviations of 0.05 lpm already flattened the detection efficiency curves in general. In order to minimize this flattening of the plateaus special care was taken to properly adjust the flows rates. That procedure revealed that the flow rate downstream of the DMA determines the shape of the plateau. The plateaus linked to different UCPCs slightly differ due to individual inlet flow rates determined by the internal pumps and the flow regulating orifices.

Also the position of the plateau contains important CPC - characteristic information. In the ideal case the plateau of the curve should reflect a detection efficiency of 100 %. Losses of particles shift the position of the plateau. These particle losses are also flow rate dependent [27]. The penetration efficiency of particles influences the curve shape too.

Information about three different parameters, suspected to influence heterogeneous nucleation, can be extracted from Figure 48 and Figure 49. Those three parameters are the relative humidity of the carrier gas, the temperature settings of the used UCPCs and the charge state of the seed particles. Indeed, two of these parameters obviously have an impact on heterogeneous nucleation.

Heterogeneous nucleation that is enhanced by a certain charge state of the seed particles cannot be seen in the results. This finding is contradictory to, for example, Kangasluoma et al. [48]. There is a slight deviation in the cutoff diameters of oppositely charged seed particles. These deviations, nevertheless, are confined within the uncertainties of the data. In contrast to that, the chosen temperature settings of the CPCs have a significant influence on particle activation. Increasing cutoff diameters are observed for increasing temperatures. The lowest cutoff diameters are measured using the lowest temperature settings. This finding is clearly linked to the saturation profile in the condenser of the CPCs. The temperature difference between the saturator and the condenser, that was not changed during this study, defines the supersaturations seed particles are exposed to [37]. Lastly, there is a seed particle material dependent influence of the relative humidity of the carrier gas on particle activation. In the case of Ag seeds, that are completely insoluble in water, no effect is visible. In this case particle activation solely depends on the temperature settings of the CPC. In the case of soluble NaCl seeds a distinct trend is observed for all temperature settings: The cutoff diameters decrease for increasing relative humidities of the carrier gas ([38] and [39]).

7.1.4 Detection Efficiency of the TSI 3772

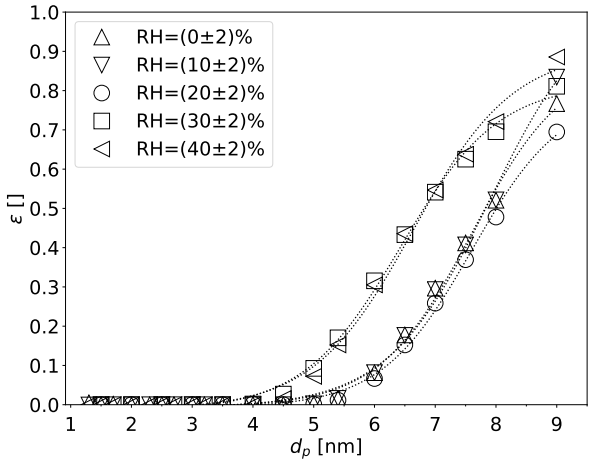

Figure 50: TSI 3772, Ag(+), std T

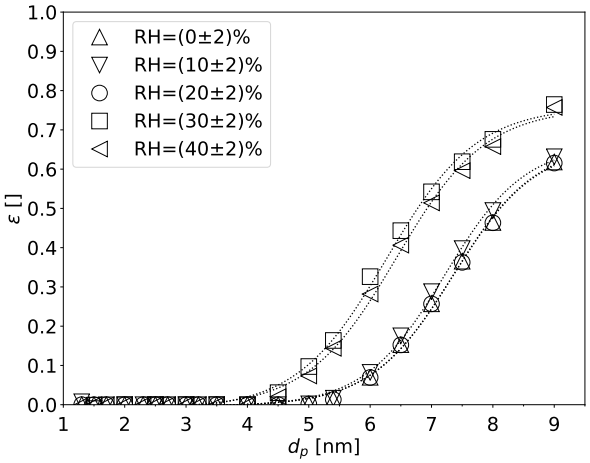

Figure 51: TSI 3772, Ag(-), std T

7.1.5 TSI 3772: Cutoff Diameters of Charged Seed Particles

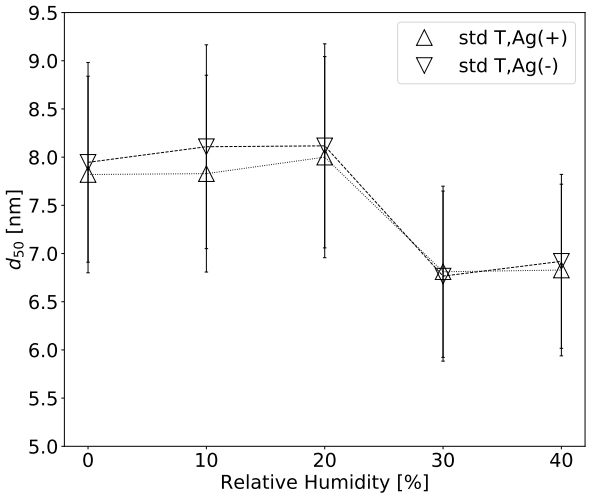

Figure 52: Cutoff Diameters of Charged Ag Seeds

7.1.6 Discussion of the Results 2

The results of the detection efficiency measurements using the TSI 3772 CPC for Ag seeds differ from the findings using the TSI 3776 (s. Figure 50 and Figure 51). Figure 52 indicates a dependence of insoluble Ag seeds on the relative humidity of the carrier gas. This result actually contradicts the aforementioned findings. The three major differences between those CPCs are the following: The TSI 3772 is not based on the capillary - sheath structure used in the TSI 3776. Secondly, the cutoff diameter provided by the manufacturer is at 10 nm using sucrose seeds (compared to sucrose - based 2.5 nm of the TSI 3776, [26]). Lastly, the concentration range of the TSI 3772 only goes up to 10^4 particles/cc [49] , whereas the TSI 3776 can measure up to 10^5 particles/cc [26]. The particle number concentrations related to these measurements can be found in Appendix E. The concentrations linked to the cutoff diameters displayed in Figure 52 were kept within the limits.
Obviously the cutoff diameter using Ag particles is lower compared to sucrose particles. There is an indication that particles with larger diameters ($\approx$ 7 nm) behave differently concerning their activation. This effect might be hidden in the plateau of the curves of the previous measurements. All particles having diameters of about 7 nm are already activated in the TSI 3776. As a result the effect of relative humidity might actually be hiding a size - dependent effect on particle activation.

7.1.7 Counting Efficiencies of Neutralized Seed Particles

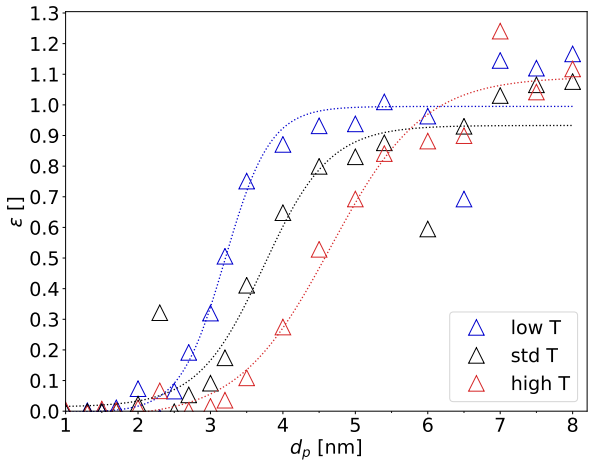

Figure 53: RH=(0±2)%, NaCl(0+)

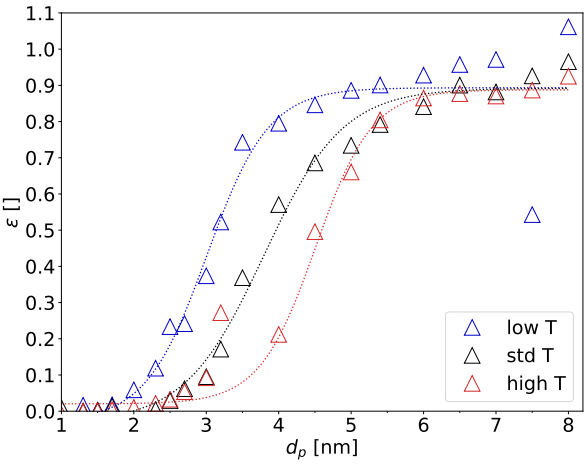

Figure 54: RH=(0±2)%, NaCl(0-)

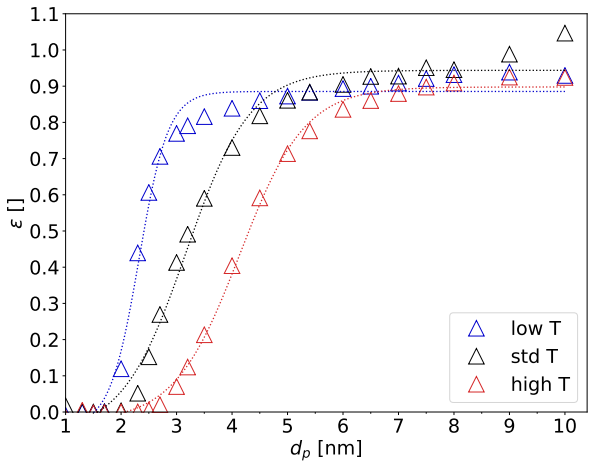

Figure 55: RH=(10±2)%, NaCl(0+), [38] and [39]

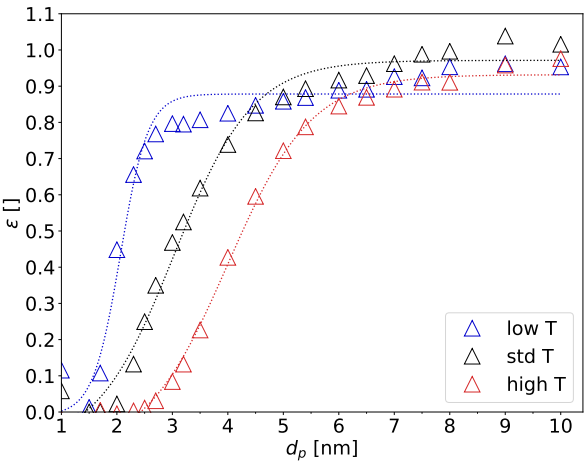

Figure 56: RH=(10±2)%, NaCl(0-)

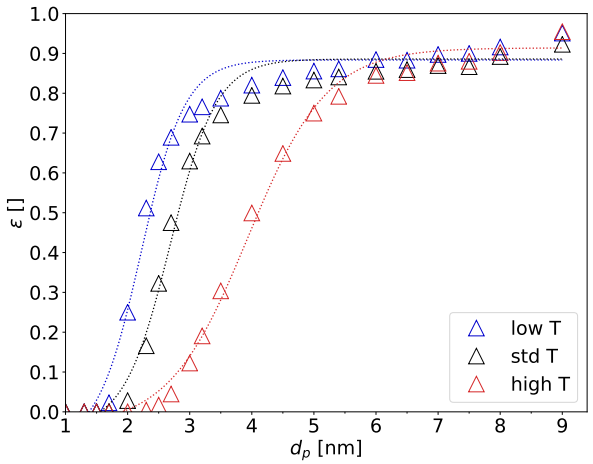

Figure 57: RH=(20±2)%, NaCl(0+)

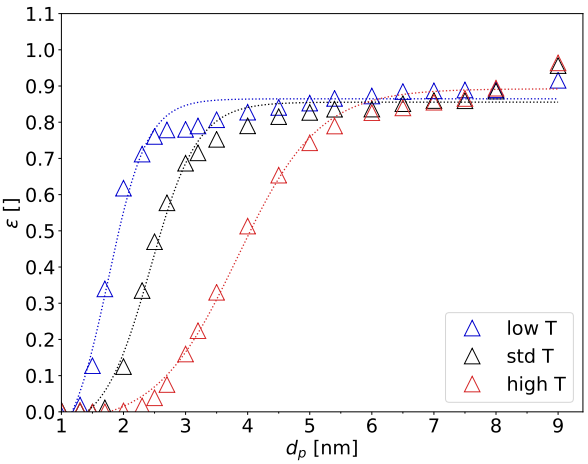

Figure 58: RH=(20±2)%, NaCl(0-)

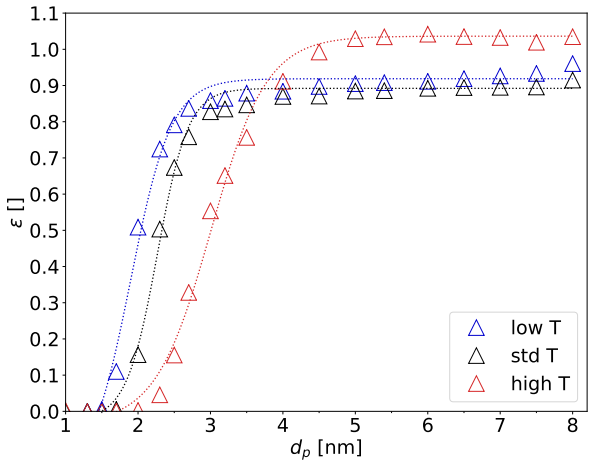

Figure 59: RH=(30±2)%, NaCl(0+)

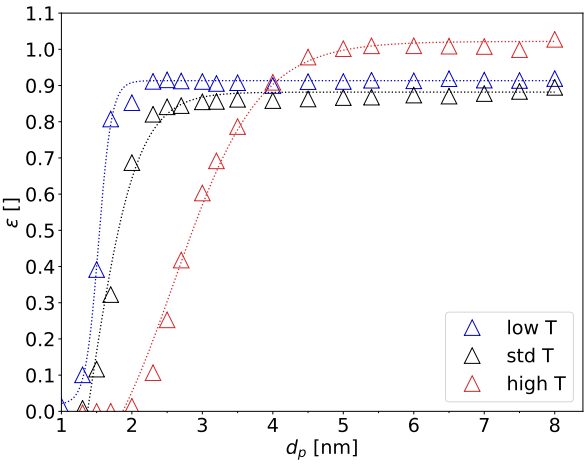

Figure 60: RH=(30±2)%, NaCl(0-)

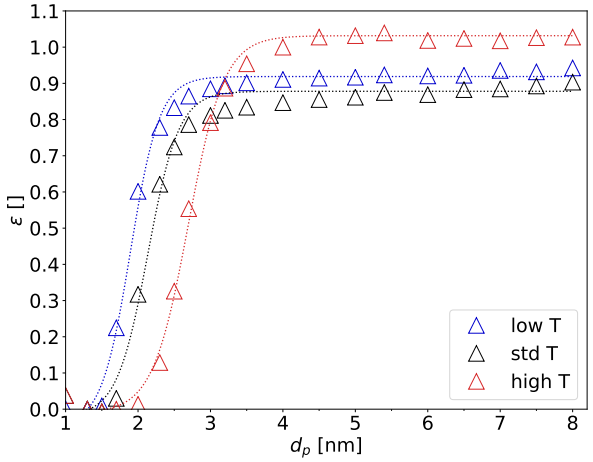

Figure 61: RH=(40±2)%, NaCl(0+)

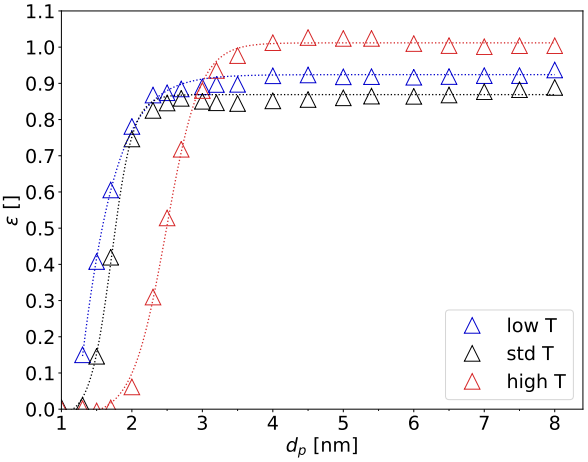

Figure 62: RH=(40±2)%, NaCl(0-)

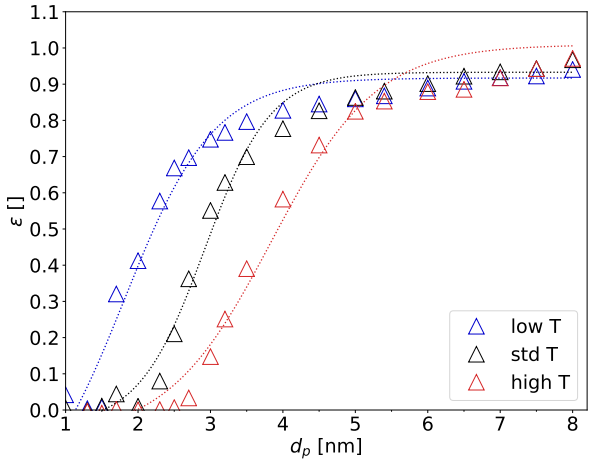

Figure 63: RH=(0±2)%, Ag(0+)

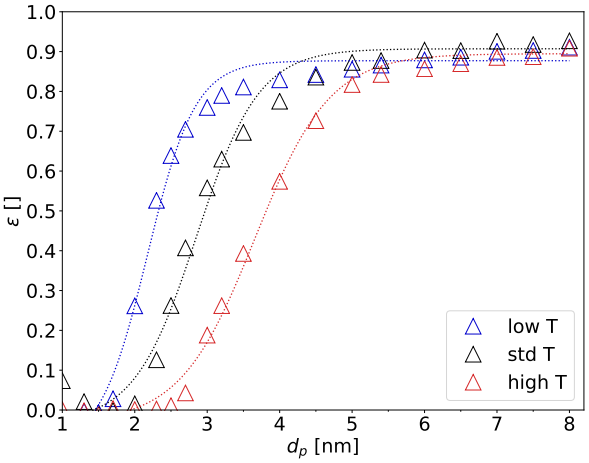

Figure 64: RH=(0±2)%, Ag(0-)

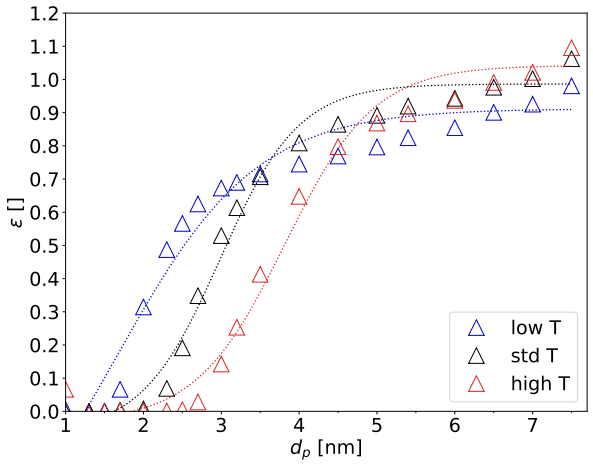

Figure 65: RH=(10±2)%, Ag(0+)

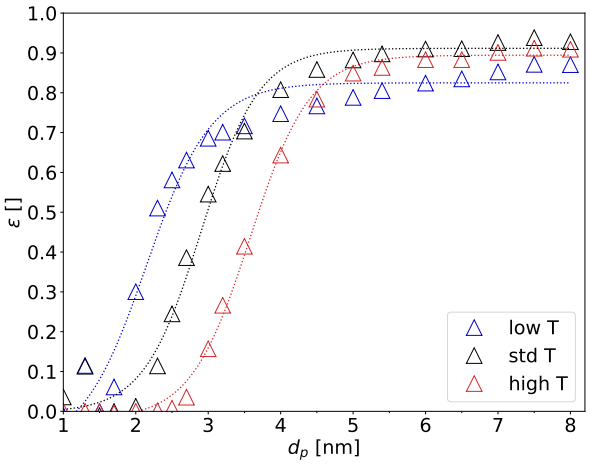

Figure 66: RH=(10±2)%, Ag(0-)

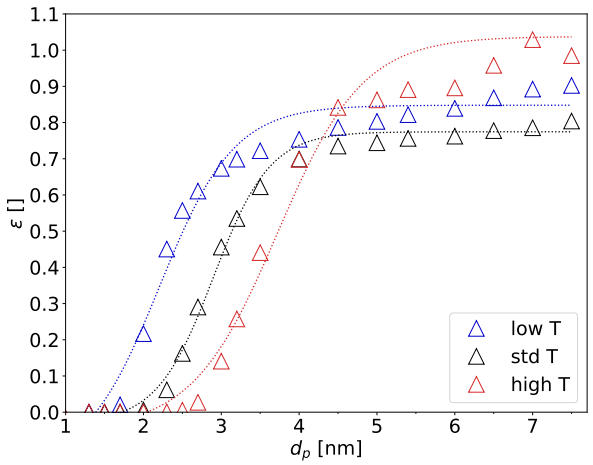

Figure 67: RH=(20±2)%, Ag(0+)

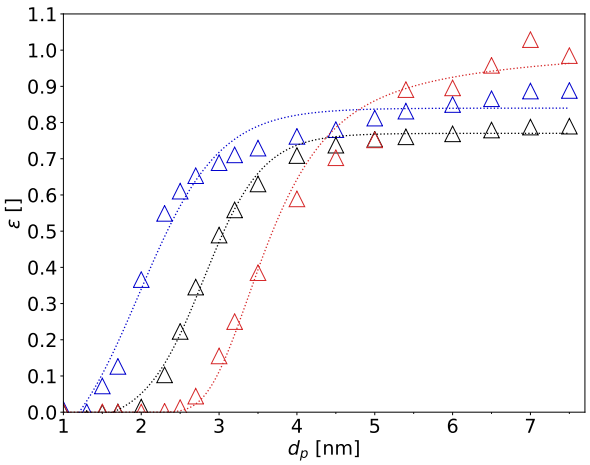

Figure 68: RH=(20±2)%, Ag(0-)

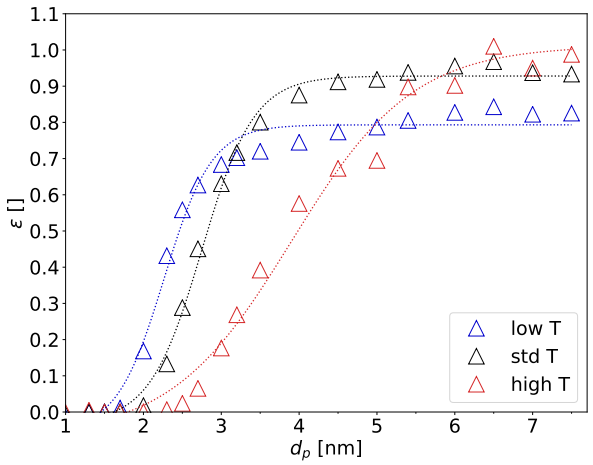

Figure 69: RH=(30±2)%, Ag(0+)

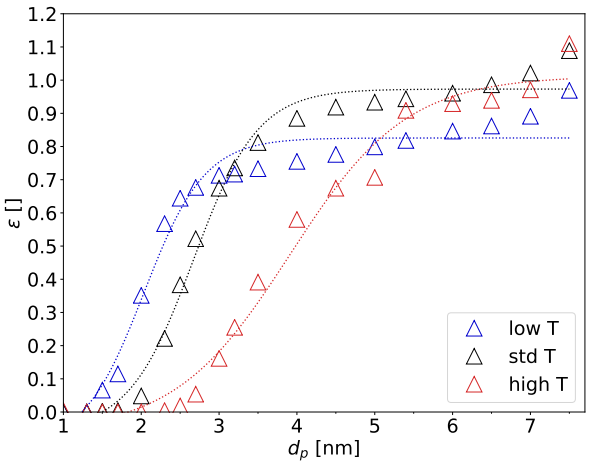

Figure 70: RH=(30±2)%, Ag(0-)

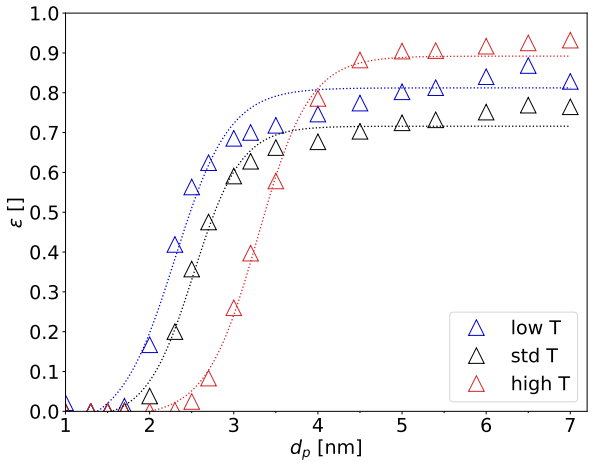

Figure 71: RH=(40±2)%, Ag(0+)

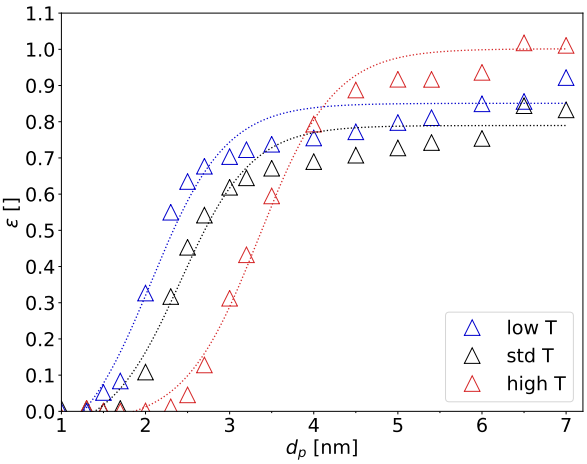

Figure 72: RH=(40±2)%, Ag(0-)

7.1.8 Cutoff Diameters of Neutralized Seeds

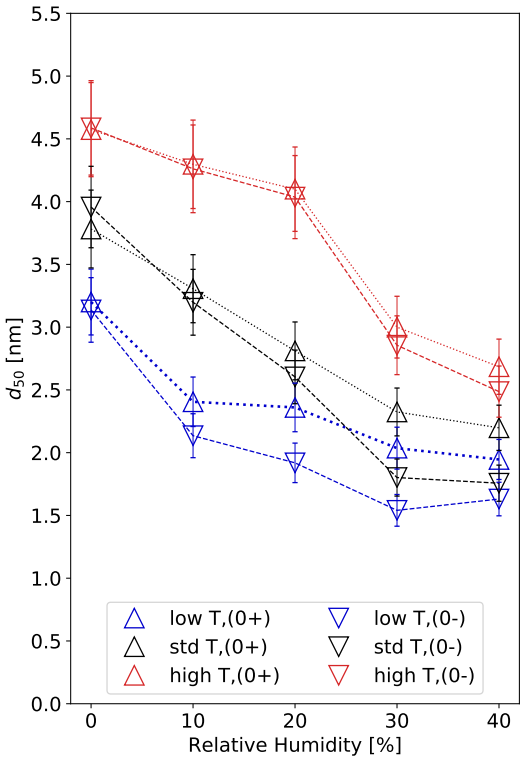

Figure 73: Cutoff Diameters of NaCl Seeds, [38] and [39]

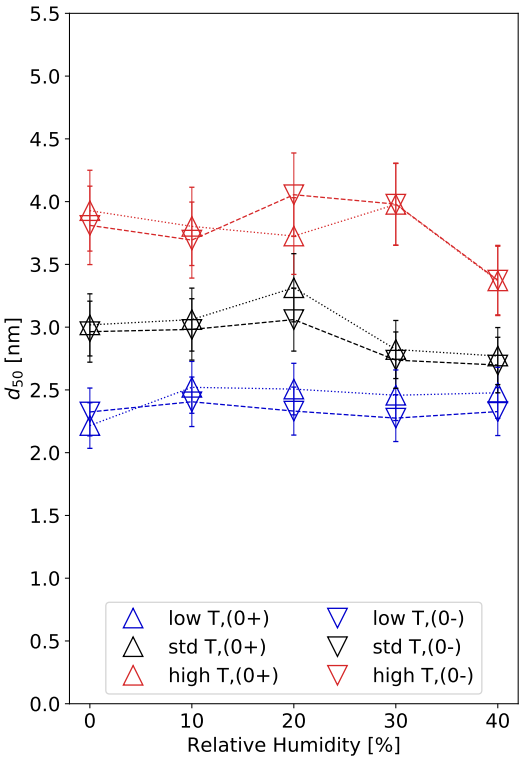

Figure 74: Cutoff Diameters of Ag Seeds, [38] and [39]

7.1.9 Discussion of the Results 3

Figure 53 and Figure 54 show the results obtained by using a dry carrier gas and NaCl seed particles. The curves turned out not to be as smooth as expected. The scattered data

points are caused by the mixing of synthetic air and compressed air. For these two (initial) measurements common T - junctions were used. As a result the mixing was inefficient. Based on these results mixing sections were used in the setup yielding much smoother detection efficiency curves.
Figure 62 displays an offset of the detection efficiency based on the lowest temperature settings of the CPC. This offset is not connected to the overall flow pattern but to the particle concentrations at small diameters. In general it is very important for these kind of measurements to keep the background signal as low as possible by precisely adjusting the flows. The particle concentrations need to be high due to the elaborated scheme of the setup and the resulting particle losses in the tubings. The particle losses are also connected to the penetration efficiencies in the CPCs and are clearly visible when taking a look at the positions of the plateaus of the curves [27]. The overall curve slopes are well pronounced and therefore a cutoff diameter can be calculated for every single curve.
In some curves a secondary increase of the detection efficiency can be seen for larger particle diameters. These deviations occur due to decreasing particle concentrations and do not have any impact on the cutoff diameter.
Figure 73 and Figure 74 are similar to the results of the measurements using charged seed particles. Again, there is no charge preference. Initially positively charged particles as well as initially negatively charged particles are activated equally. A distinct temperature dependence is recognized. The best activation occurs for the lowest temperature settings of the CPC. Accordingly a strong dependence of the cutoff diameter on the relative humidity of the carrier gas is visible. For increasing relative humidity the cutoff diameter decreases for every temperature setting for NaCl seed particles ([38] and [39]). In the case of Ag particles the influence of the relative humidity vanishes and the effect of the temperature settings remains ([38] and [39]). Generally the range of the cutoff diameters is very similar to Figure 48 and Figure 49. The quality of the Ag - based curves has severely improved supporting the decision to use mixing chambers instead of T - junctions.

7.2 PSM - Based Experiments

The following figures present the results of the measurements using booster stages. "CPC*" refers to the tuned TSI 3776 UCPC, "NE" describes the combination of the TSI 3777 Nano enhancer and a TSI 3772 CPC and "PSM" refers to the combination of the Airmodus A10 and the Airmodus A20 CPC. Due to the irregular curve shapes data fitting appeared to be very difficult. As a result the aim was to approximate the curve slopes and obtain the cutoff diameter by using a fit function.

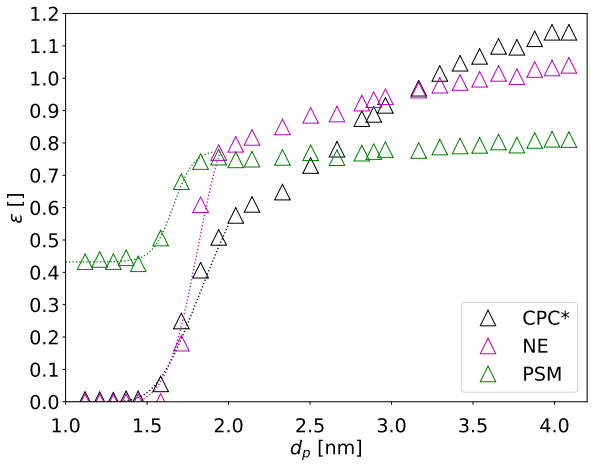

Figure 75: RH=(0±2)%, NaCl(+), std Settings

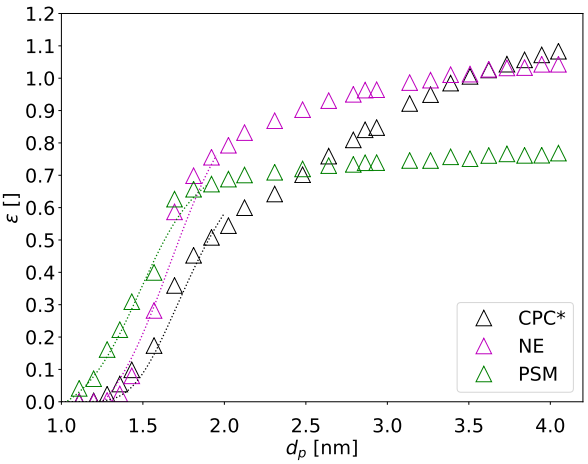

Figure 76: RH=(0±2)%, NaCl(-), std Settings

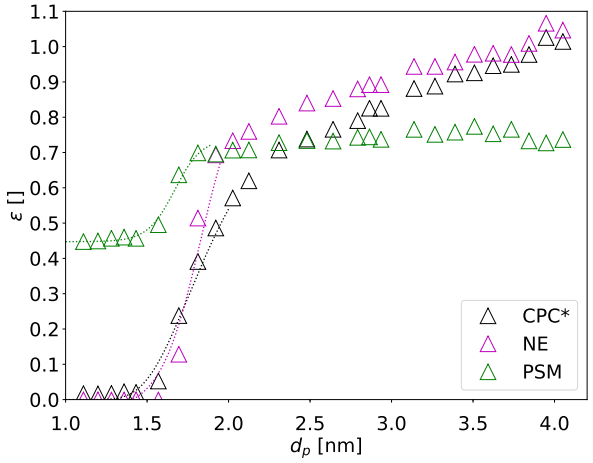

Figure 77: RH=(10±2)%, NaCl(+), std Settings

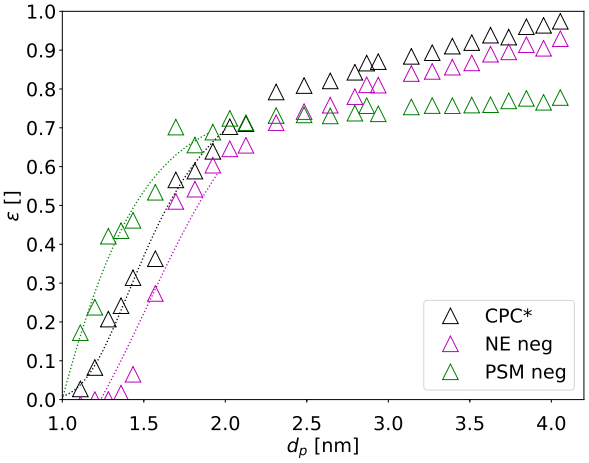

Figure 78: RH=(10±2)%, NaCl(-), std Settings

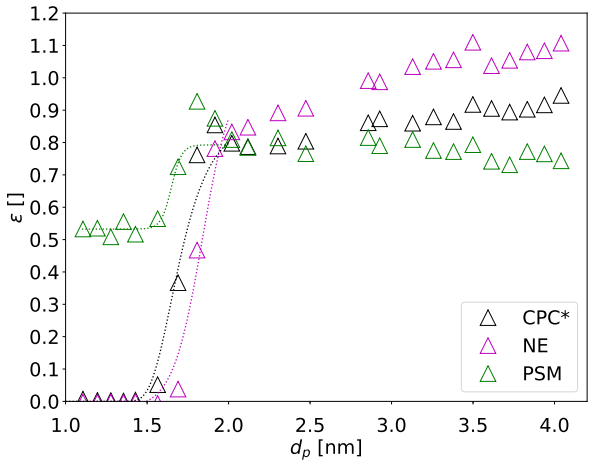

Figure 79: RH=(40±2)%, NaCl(+), std Settings

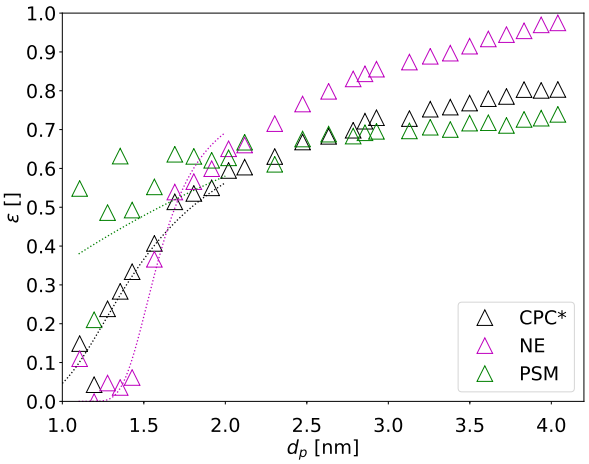

Figure 80: RH=(40±2)%, NaCl(-), std Settings

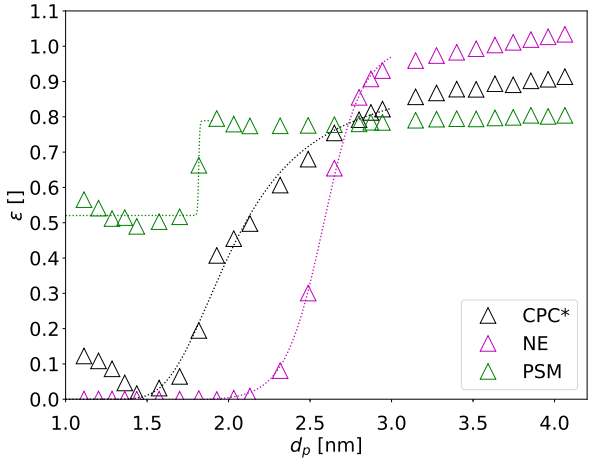

Figure 81: RH=(0±2)%, Ag(+), std Settings

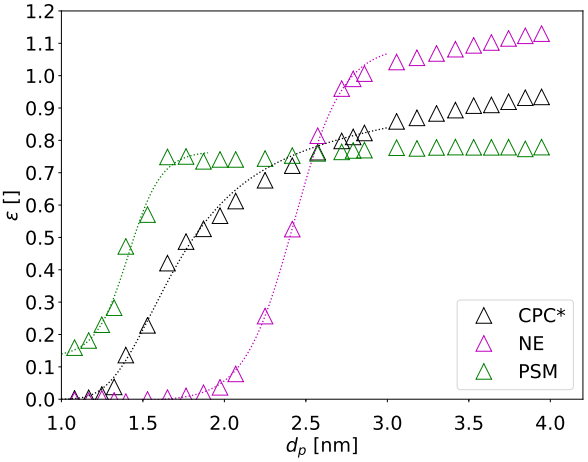

Figure 82: RH=(0±2)%, Ag(-), std Settings

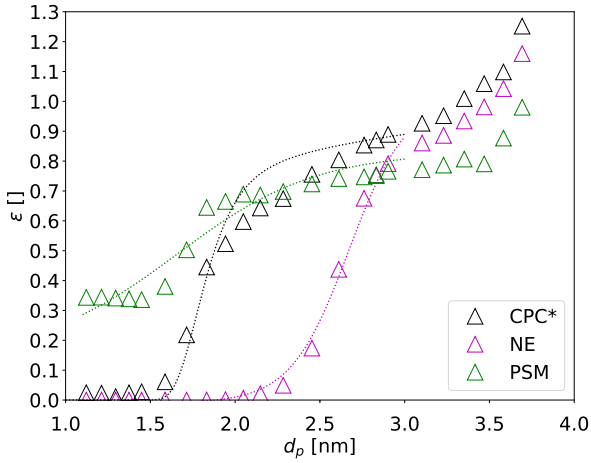

Figure 83: RH=(10±2)%, Ag(+), std Settings

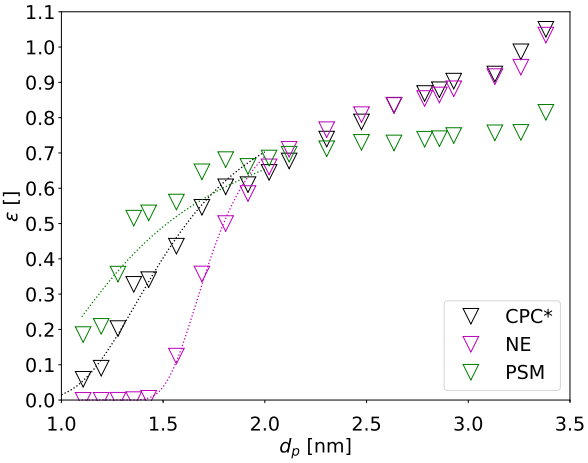

Figure 84: RH=(10±2)%, Ag(-), Std Settings

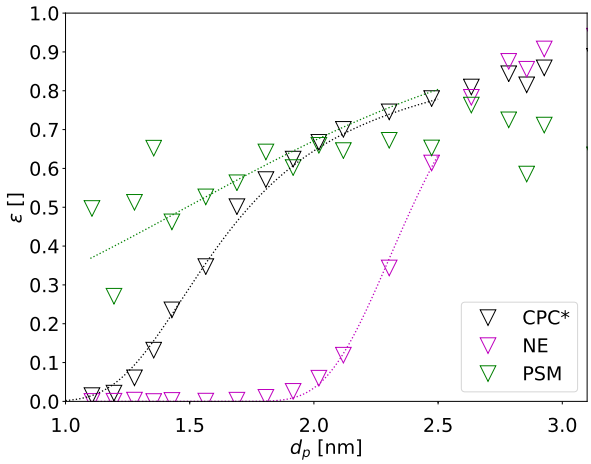

Figure 85: RH=(40±2)%, Ag(-), std Settings

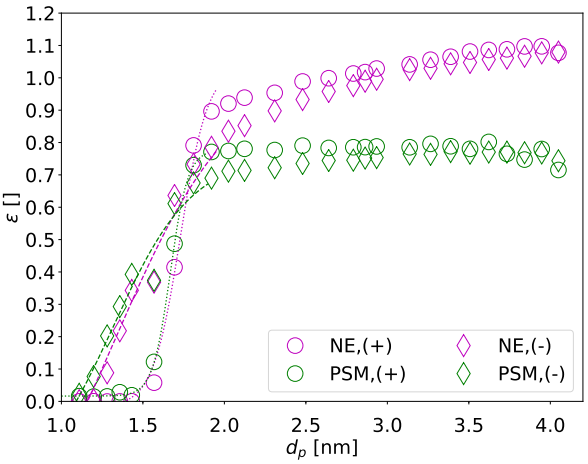

Figure 86: RH=(0±2)%, NaCl, cld Settings

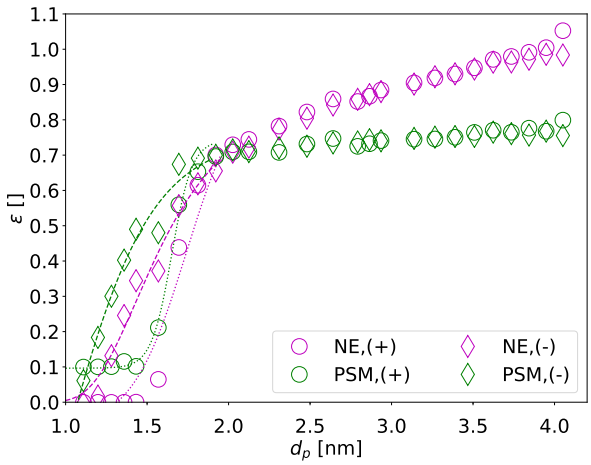

Figure 87: RH=(10±2)%, NaCl, cld Settings

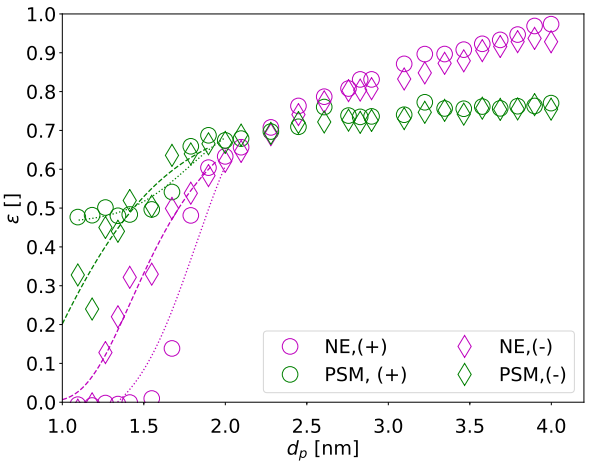

Figure 88: RH=(40±2)%, NaCl, cld Settings

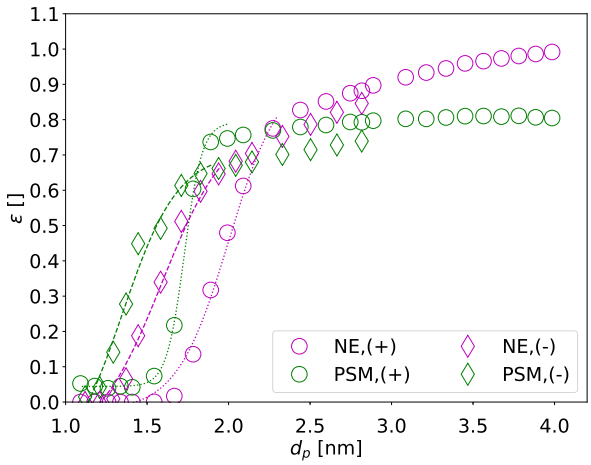

Figure 89: RH=(0±2)%, Ag, cld Settings

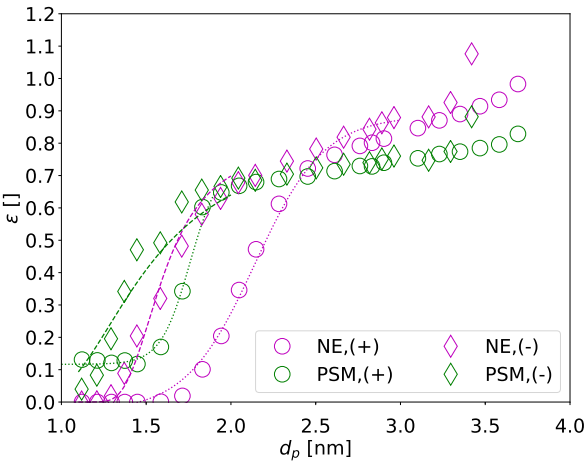

Figure 90: RH=(10±2)%, Ag, cld Settings

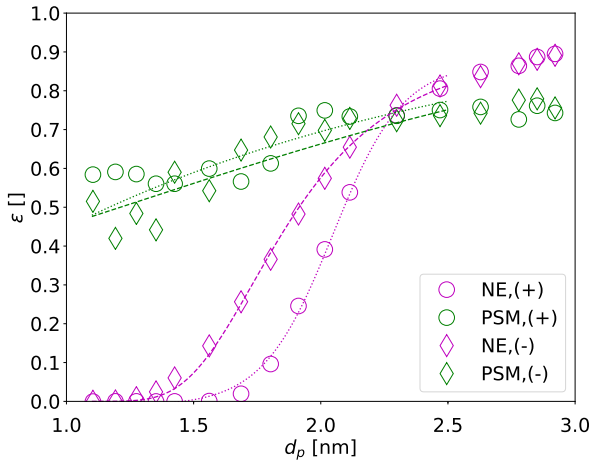

Figure 91: RH=(40±2)%, Ag, cld Settings

7.2.1 Cutoff Diameters of Charged Seeds

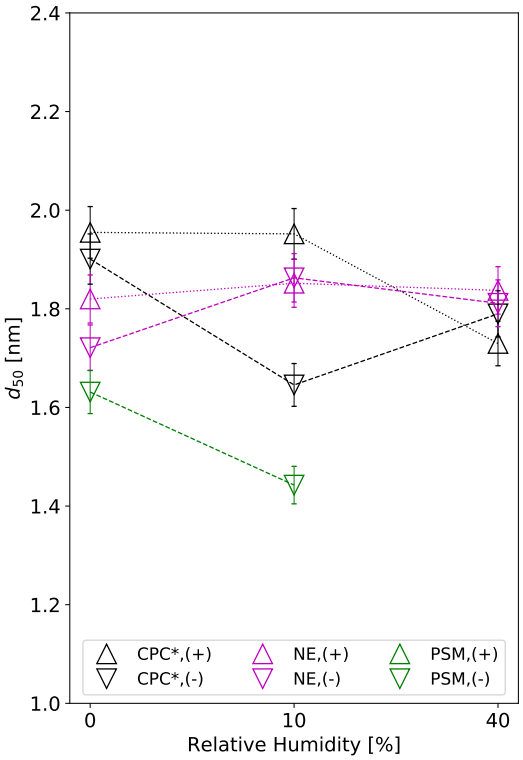

Figure 92: Cutoff Diameters of Charged NaCl Seeds based on std Settings

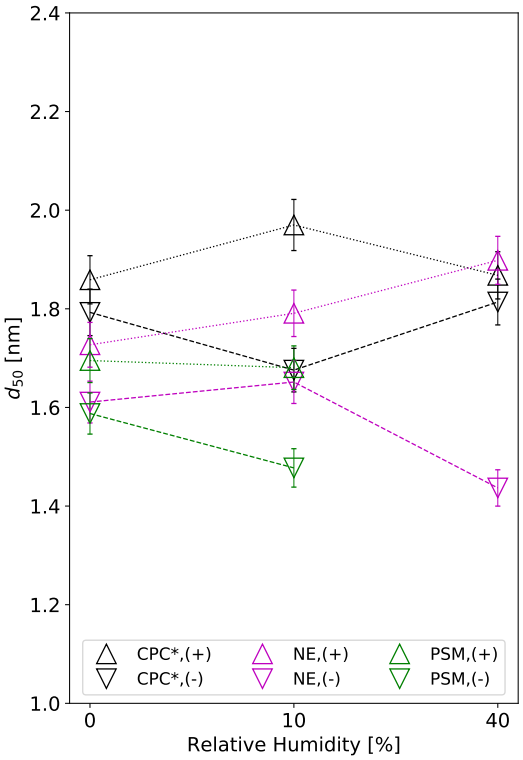

Figure 93: Cutoff Diameters of Charged NaCl Seeds based on cld Settings

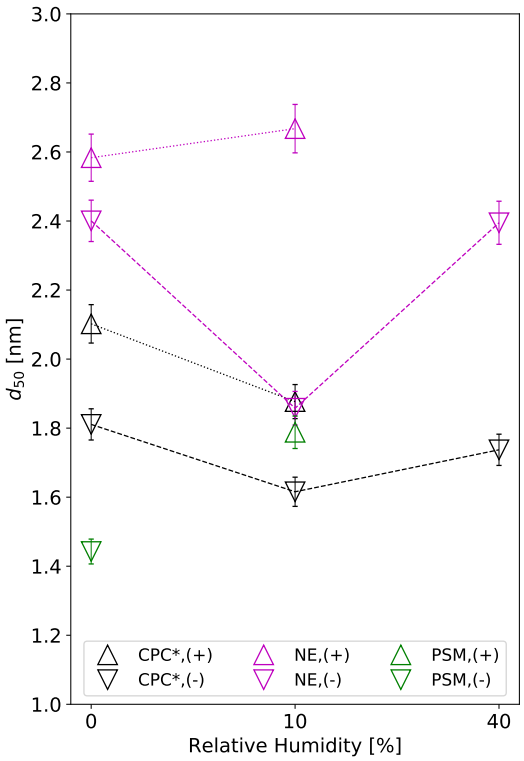

Figure 94: Cutoff Diameters of Charged Ag Seeds based on std Settings

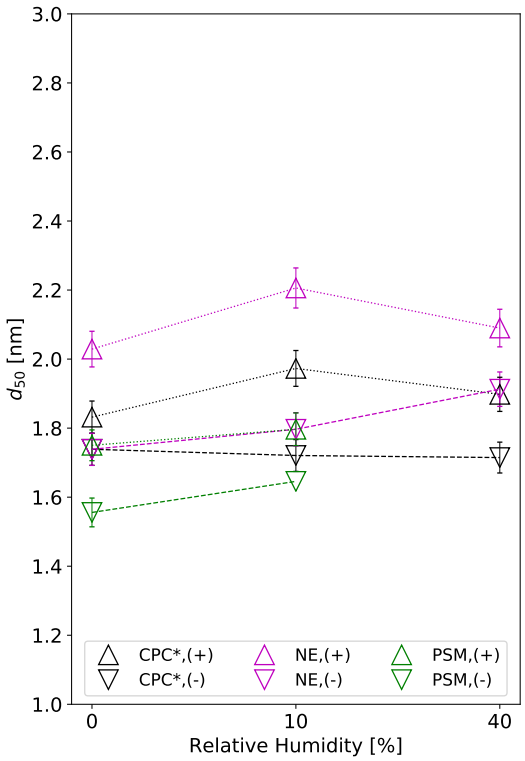

Figure 95: Cutoff Diameters of Charged Ag Seeds based on cld Settings

7.2.2 Discussion of the Results 4

The activation curves obtained by using booster stages, like the PSM A10 and the TSI 3777 Nano enhancer, exhibit a variety of effects and dependences. These are discussed, one after another, in this section.

First of all there are again effects of the seed particle concentrations on the curve shapes. The data points in Figure 81 for seed particle diameters between 1 nm and 1.5 nm, for example, can clearly be attributed to low particle concentrations. Furthermore steps in the plateau of a curve are also linked to low particle concentrations at larger diameters (s. Figure 77, Figure 79, Figure 83, Figure 84, Figure 87 and Figure 90).

Due to the large number of involved instruments well balanced flow conditions could not be provided during every single measurement. There were slight deviations from the ideal flow patterns. The shapes of the plateaus reflect that. Most of the plateaus are not perfectly horizontal. The Airmodus A10 thereby shows the best behavior. There seems to be some kind of insensitivity to small flow rate variations. This behavior is linked to the underlying functioning principle of the instrument (s. Section 8).

Figure 92 - Figure 95 show the summarized results of all measurements involving booster stages. Interestingly, there is no clear trend for particle charges, the relative humidity of the carrier gas or the chosen instrument settings visible. Changing the operational settings

is related to another curve shape. Furthermore the dependence on the relative humidity vanishes. There are changes in the cutoff diameters related to different relative humidities but these changes do not follow any pattern. In general the values of the cutoff diameters corresponding to certain relative humidities seem to be stochastically scattered around an average value. These deviations can also be justified based on variations of the data.
As far as particle charges are concerned the activation curves corresponding to the Nano enhancer and the tuned TSI 3776 show no charge preference. The curves based on positively and negatively charged particles are similar. In the case of the PSM there is a difference. Those curves show a non - negligible offset for positively charged particles with small diameters using standard settings. Furthermore the cutoff curve of the PSM changes with increasing relative humidity of the carrier gas for all seed particles. In the extreme case of relative humidities of 40 % not a single PSM - based cutoff curve keeps its shape. Particles are activated instantly. Overall the tuned CPC shows the best results. The lowest cutoff diameters can be measured using this CPC. It is therefore possible to completely replace the TSI 3777 by a tuned TSI 3776 in terms of the cutoff diameter. The expected shape of an activation curve is preserved using the Nano enhancer. The PSM exhibits a different kind of dependence on the relative humidity of the carrier gas. In order to investigate this dependence and the occurring offset for positively charged seed particles it is necessary to take a look into the raw data. In order to do that all raw data corresponding to dry conditions and a RH of 40% is plotted (s. Figure 97 - Figure 112).
Although there is no correlation between the cutoff diameters of the particle detectors and the relative humidity of the carrier gas, increasing levels of relative humidity lead to a built - up of background signal for both working conditions in the PSM. As a result background measurements were performed using positively charged Ag and NaCl seeds. Thereby a voltage of 0 V was applied to the UDMA for approximately 5 minutes and the particle number concentrations were recorded (s. Figure 96). Table 9 shows the mean values as well as the standard deviations of the background signal in the PSM.

Seed	RH [%]	Δ(RH) [%]	Settings	$\langle\mathcal{N}\rangle$ [#/cc]	$\sigma(\mathcal{N})$ [#/cc]
NaCl(+)	0	2	cld	8.37	6.63
NaCl(+)	40	2	cld	22.60	16.70
Ag(+)	0	2	cld	17.44	48.03
Ag(+)	40	2	cld	187.48	50.90

Table 9: Background Measurements: The table shows the mean particle number concentration as well as the standard deviations based on background measurements using positively charged seeds.

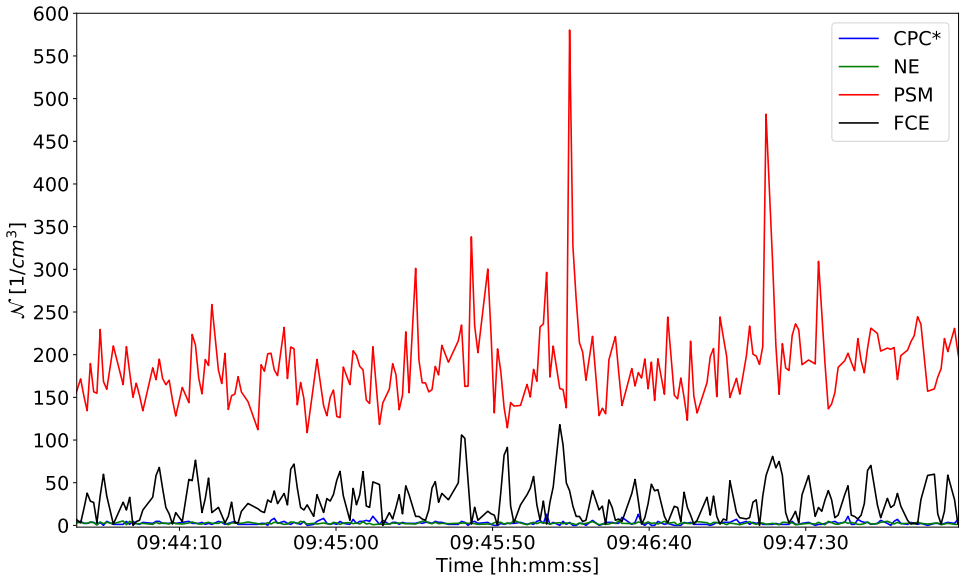

Figure 96: Background Measurement: RH=(40±2)%, Ag(+), cld Settings. The spikes in the signal of the PSM linked to the standard deviations in Table 9 are clearly visble.

A clear dependence of the background signal on the relative humidity of the carrier gas can be seen. The high values for the standard deviations are linked to randomly occurring concentration peaks in the spectra. Additionally there is a slight difference in the spectra depending on the chosen PSM settings. There is a higher background noise for the "cld" settings.

Furthermore the offset for positively charged particles, that is also visible in the cutoff curves, is clearly caused due to charger ions. These charger ions are also detected in the case of negatively charged particles. The according signal in the positive case is much higher and, as a result, has a recognizable influence on the cutoff curve. It can be seen that the different polarities are linked to a different detection behavior and therefore to another curve shape. The background signal is accounted for by the way data is obtained (s. Section 6.1). The background noise of the PSM is not stable enough to apply an overall background correction (s. Figure 112).

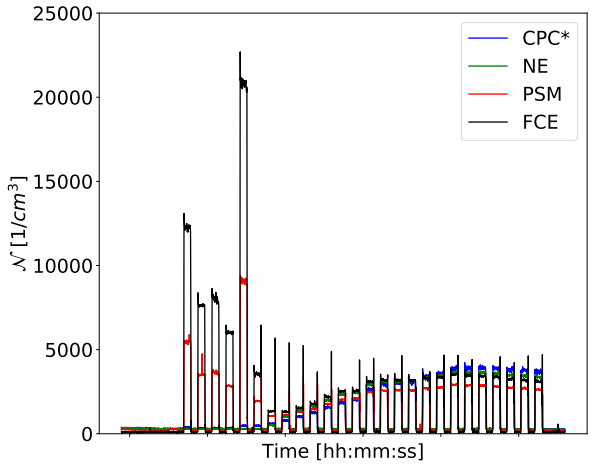

Figure 97: RH=(0±2)%, NaCl(+), std

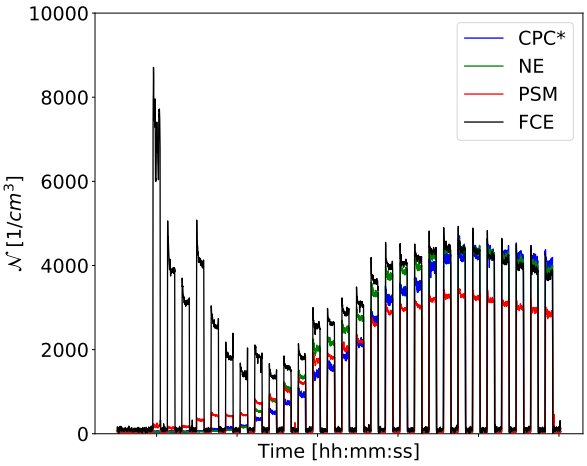

Figure 98: RH=(0±2)%, NaCl(-), std

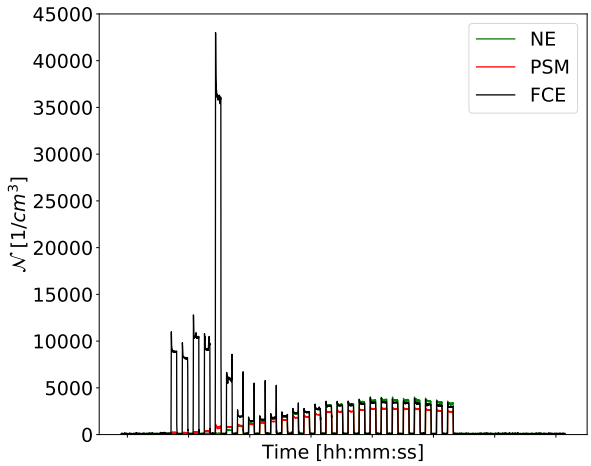

Figure 99: RH=(0±2)%, NaCl(+), cld

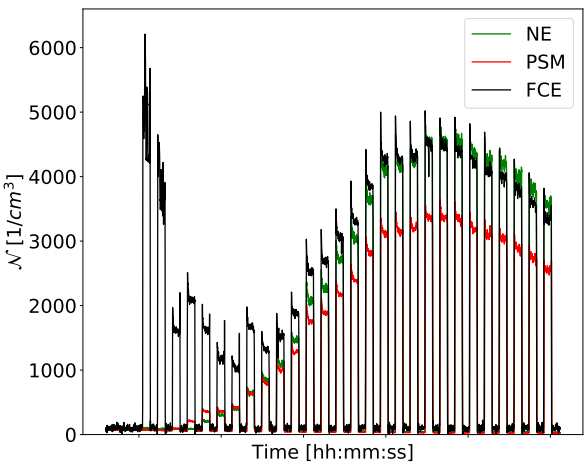

Figure 100: RH=(0±2)%, NaCl(-), cld

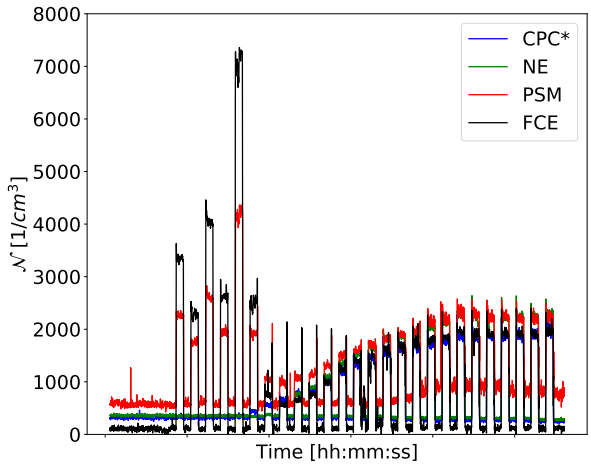

Figure 101: RH=(40±2)%, NaCl(+), std

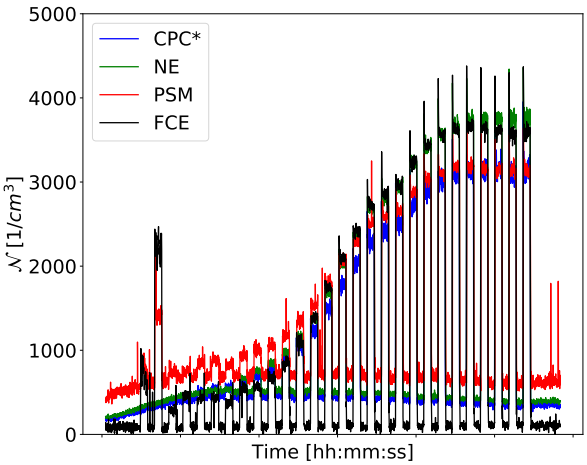

Figure 102: RH=(40±2)%, NaCl(-), std

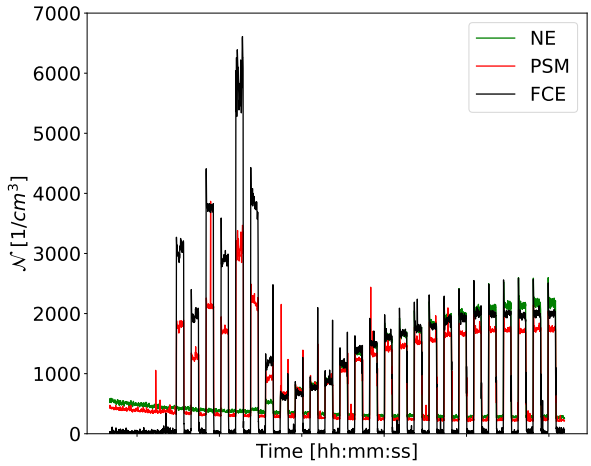

Figure 103: RH=(40±2)%, NaCl(+), cld

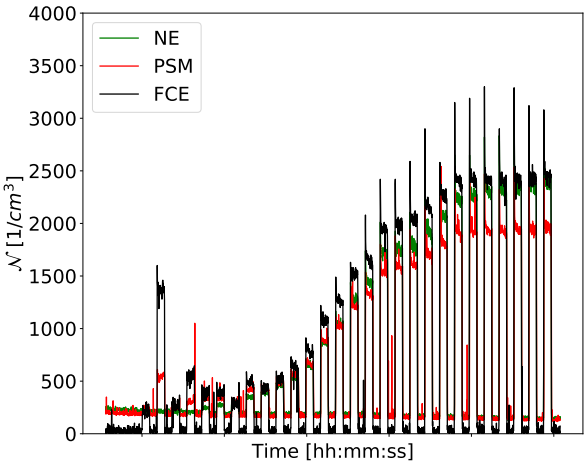

Figure 104: RH=(40±2)%, NaCl(-), cld

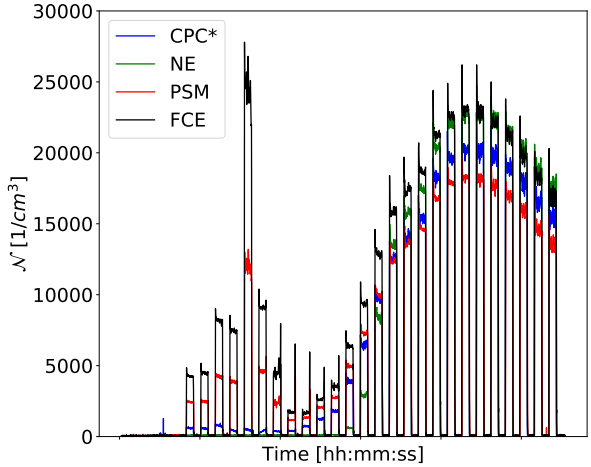

Figure 105: RH=(0±2)%, Ag(+), std

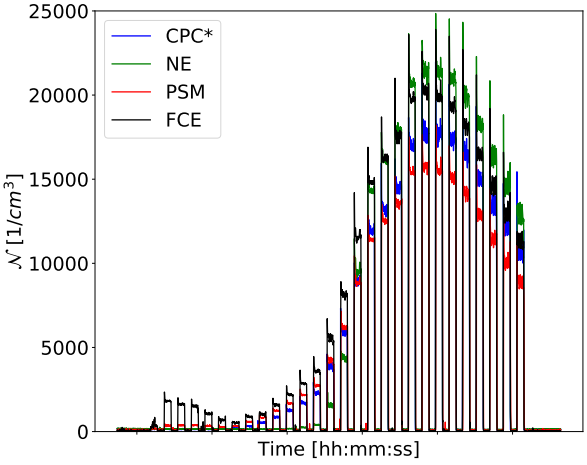

Figure 106: RH=(0±2)%, Ag(-), std

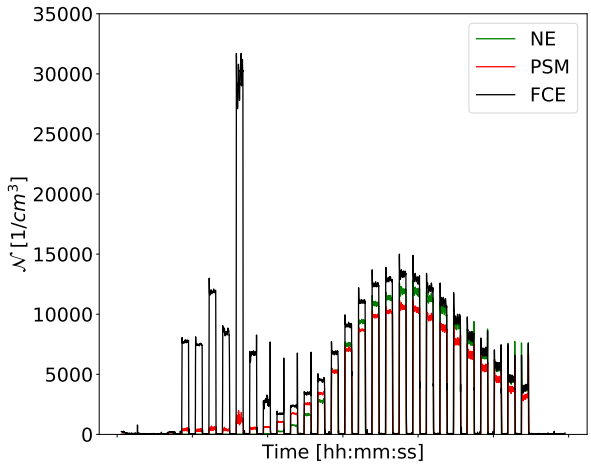

Figure 107: RH=(0±2)%, Ag(+), cld Settings

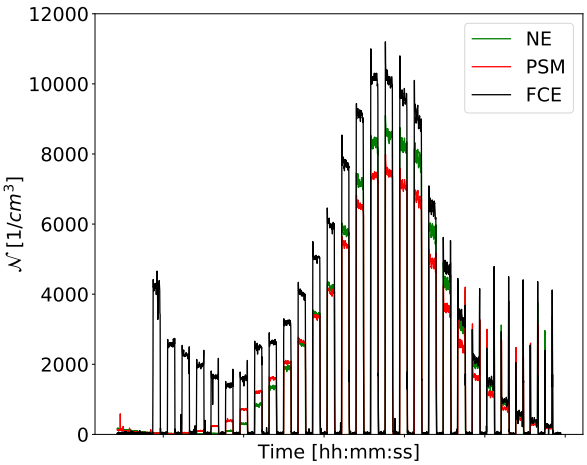

Figure 108: RH=(0±2)%, Ag(-), cld

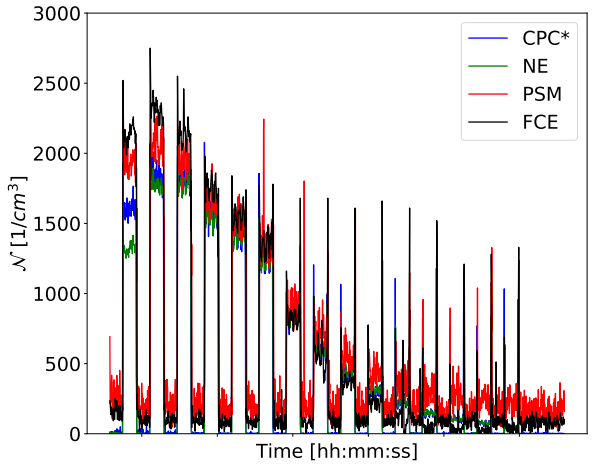

Figure 109: RH=(40±2)%, Ag(+), std

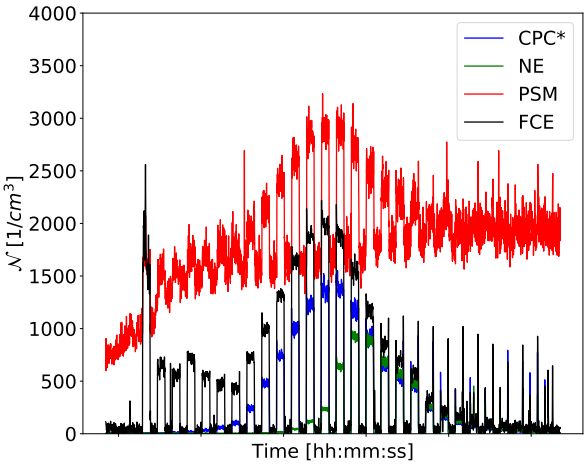

Figure 110: RH=(40±2)%, Ag(-), std

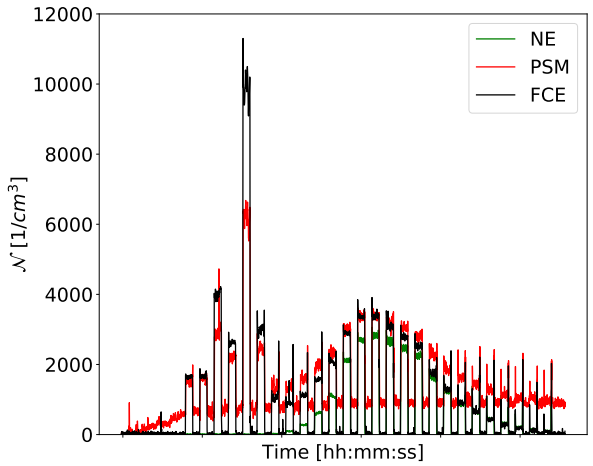

Figure 111: RH=(40±2)%, Ag(+), cld

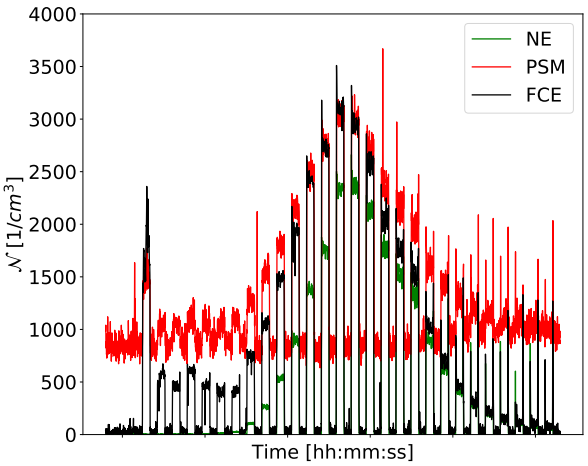

Figure 112: RH=(40±2)%, Ag(-), cld

Generally, the reliability of the results concerning the PSM has to be questioned (s. Section 9). The calculated cutoff diameters are not based on data yielding an activation curve similar to Figure 25. PSM related data can be used for evaluating the influence of the relative humidity of the carrier gas on particle activation and the calculated cutoff diameters correspond to a detection efficiency of 50 %. The curve shapes were not taken into account for these calculations.

8 Physicochemical Approach to Particle Growth

The relative humidity of the carrier gas influences particle activation of NaCl seed particles in butanol - based CPCs. Consequently the relevant property of the seed particles is their solubility in the working fluid. Solubility of salts in a solvent is always linked to the polarity of the solvent. As a result there is a link between vapor polarity, seed particle solubility and the relative humidity of the carrier gas in CPCs.
Preliminary work on this topic has been done by C. Li and C. J. Hogan, Jr. [50]. The authors investigated the uptake of organic vapors by sodium chloride cluster ions in the nanometer range. A differential mobility - mass spectrometer was used. It was found that the molecular structure of the vapor molecules has an influence on vapor uptake. Furthermore effects due to charge polarity were involved in the uptake process. Consequently, the authors used solvent polarity to explain and discuss their results. [50]
Literature review unveils two commonly known effects describing the interaction of nanometer - sized NaCl particles and water: particle shrinkage and deliquescence. These two effects also need to be considered when interpreting the results of this thesis.

8.1 Particle Shrinkage and Deliquescence

In 2000 L. Krämer et al. published a study on the interaction of water vapor with NaCl particles [51]. Sodium chloride particles with diameters between 19 nm and 200 nm were exposed to water vapor and differential mobility analysis was performed using a tandem DMA setup. The authors found a decrease in particle size up to 50 % for relative humidities under the deliquescence threshold. This particle shrinkage was attributed to a microstructural rearrangement of the NaCl particles. [51]
Additionally G. Biskos et al. published their work on the effect of deliquescence of NaCl particles in 2006 [52]. According to this publication crystalline sodium chloride particles spontaneously take up water above a certain level of RH (deliquescence). This spontaneous water uptake can be noted as a broadening of the particle size distribution. The behavior of seed particles with diameters of 10 nm and 40 nm was investigated. The authors found out that the deliquescence threshold level for the sodium chloride particles was 76 % and 82 % of RH, respectively. [52]
Both effects play an important role during particle growth and have to be combined with the investigated RH dependence in order to obtain a complete picture. The basics of vapor polarity and the chemical structure of commonly used working fluids are therefore presented in this chapter.

8.2 Electronegativity and Polar Molecules

Following [53] electronegativity is an empirical parameter. It is commonly used to describe the inequality of electron sharing in a chemical bond. L. Pauling introduced it and arbitrarily picked an electronegativity value of 4.0 for fluorine, that is the element with the highest

electronegativity value. Pauling observed that nonpolar covalent bonds have lower dissociation energies than polar covalent bonds. [53]
Differences in the electronegativity of atoms in a molecule lead to polar molecules. Table 10 sums up the electronegativities of relevant chemical elements.

Element	Electronegativity
Fluorine F	3.98
Caesium Cs	0.79
Hydrogen H	2.20
Carbon C	2.55
Oxygen O	3.44

Table 10: Electronegativities According to Pauling, [54]

P. Atkins and J. de Paula [54] introduce polar molecules as molecules with a permanent electric dipole moment. Partial charges (commonly denoted as δ^+ and δ^-) on atoms are formed due to differences in electronegativity. [54]
These partial charges arise from changes in the spatial distribution of electrons (electron cloud, see Section 8.2.2). The extent of polarity of a molecule can be measured using its electric dipole moment μ or its dielectric constant γ. Table 11 sums up the values of these parameters for three commonly used working fluids in CPCs. γ is thereby used to describe a bulk property, whereas μ refers to single molecules.

Solvent	γ	$\mu \cdot 10^{-30}$ [Cm]
N - Butanol	17.51	5.8
Diethylene Glycol	31.69	7.7
Water	78.36	6.2

Table 11: Polarity of Working Fluids, [55]

Due to the ancient alchemic principle "simila similibus solvuntur" there is a connection between the polarity of a molecule and its properties by means of solvation. In general solvation describes the process of surrounding a molecule or ion by a shell of solvent molecules determined by intermolecular forces between the solvent and the solute [55]. Solvents can be polar or apolar and, as a result, the aforementioned principle refers to this property. It states that polar solutes can easily be dissolved in polar solvents and vice versa. In order to set these principles into context to the performed measurements the chemical structure of the used working fluids has to be analyzed.

8.3 Chemical Structure of Common Working Fluids

Figure 113, Figure 114 and Figure 115 show the chemical structure of the working fluids used in the particle detectors. The gray spheres correspond to carbon atoms, the white ones to

hydrogen atoms and the red spheres represent oxygen atoms. The figures accurately display the angles between the different atoms. All three molecules are polar solvents.
Butanol (s. Figure 113) is a primary alcohol. It consists of a carbon chain and one hydroxyl group (- OH). The adjective "primary" thereby refers to the appearance of one OH - group. Its counterpart in the group of aliphatic hydrocarbons is butane, which is a completely apolar compound. Due to the attachment of a hydroxyl group differences in the electronegativities of the constituents are introduced. The oxygen atom has the highest electronegativity of all occurring atoms and therefore draws electrons towards itself. A polar covalent bond is formed and the electron cloud of the molecule is deformed. The molecule can be divided into an hydrophobic part (the C - chain) and a hydrophilic part (OH - group), which is a potential docking site for other molecules based on hydrogen bonds. As a result butanol is a polar compound. It is frequently used as a working fluid in CPCs due to its small diffusion coefficient (s. Section 3.4.2). Water (s. Figure 114) is a very common and cheap polar solvent. It has a typical dipole structure. Accordingly, water is miscible with other polar solvents, like DEG or butanol, by establishing hydrogen bonds. The third polar solvent in use was diethylene gylcol (s. Figure 115). DEG belongs to the group of secondary alcohols (dioles). It has the structure of an ether and therefore can be seen as two ethanol molecules that are connected by an oxygen atom. These functional groups lead to a high polarity of the molecule.

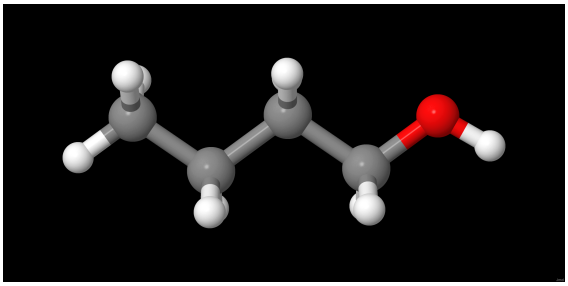

Figure 113: N-Butanol, C_4H_9OH, generated using [56]

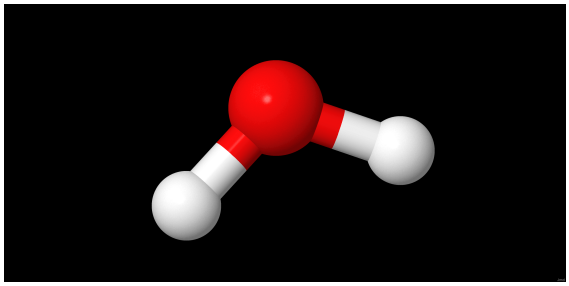

Figure 114: Water, H_2O, generated using [56]

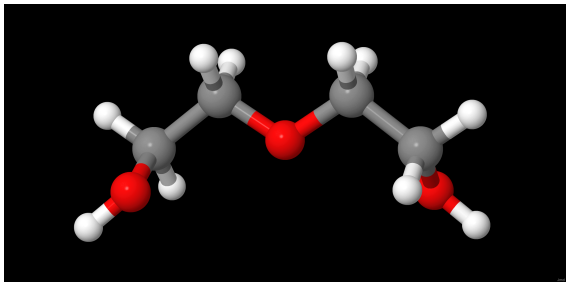

Figure 115: Diethylene Gylcol (DEG), $C_4H_{10}O_3$, generated using [56]

A convenient way of displaying the differences in the polarity of these three compounds

consists of using the Molecular Electrostatic Potential (MEP). According to [57] the MEP is defined as the electrostatic potential around a molecule that is formed by its nuclei and electrons. It can be used as a proxy for the reactivity of a molecule. Electrophilic and electrophobic regions of a molecule can be displayed. As a result a positive test charge is attracted towards molecule parts with a negative MEP (red) and repelled from parts with a positive MEP [57]. The MEPs of the previously discussed molecules are qualitatively displayed in the Figure 116, Figure 117 and Figure 118.

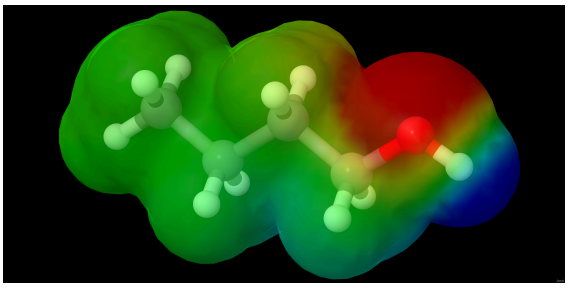

Figure 116: MEP: N - Butanol, generated using [56]

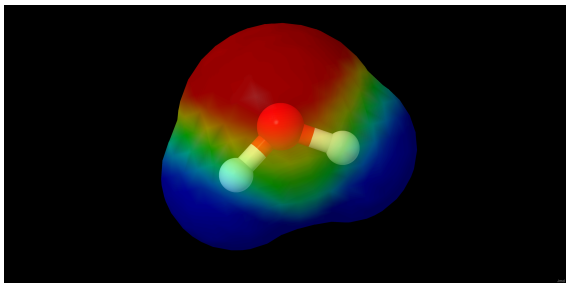

Figure 117: MEP: Water, generated using [56]

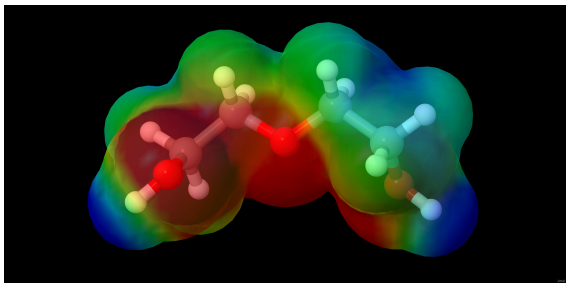

Figure 118: MEP: Diethylene Gylcol, generated using [56]

In the case of the MEP of butanol it is obvious that the hydroxyl group is responsible for a distortion of the electron cloud. The largest part of the molecule is neutral (green). There is a quite large negative section around the oxygen atom and a fairly weak positive section next to the hydrogen atom. These charges are located next to each other and as a result the dipole moment of the molecule is small. The MEP map of water looks different. Nearly the whole molecule is polarized. There is only a small region of electrical neutrality between the hydrogen atoms and the oxygen atom. DEG shows a very wide region of negative or positive potential and is therefore comparable to water. There is no neutral tail, like in the case of butanol. These MEPs clearly reflect and confirm the values of μ and η displayed in Table 10.

8.4 Vapor Polarity and Vapor Uptake in Butanol - Based CPCs

The results of this thesis clearly show the effect of the relative humidity of the carrier gas on particle activation for soluble seed particles. The decrease of the cutoff diameter occurs for all seed particle charges. There is no effect when using Ag seed particles. Based on the aforementioned basics of vapor polarity and solvation processes an effect using insoluble Ag particles cannot be expected. Butanol has compared to all other working fluids the lowest polarity in terms of its electric dipole moment and its dielectric constant. As a result any mixture of butanol and water increases the overall polarity of the working fluid ([38] and [39]). The tendency of forming out a solvent cage around a NaCl seed particle increases accordingly. This enhanced dissolving of seed particles is likely to reduce the energy barrier necessary to grow an embryo on a seed particle's surface. Solubility is connected to an energetic advantage. Releasing energy by dissolving a seed particle in a solvent further reduces the activation barrier of the particle in terms of Gibbs free energy. This process is independent from any preexisting seed particle charge. Therefore decreasing cutoff diameters also occur for neutralized seed particles. Additional charge on the seeds is likely to even enhance this process. As a result there is a notable difference in the decrease of the cutoff diameters between charged seed particles and neutralized seed particles. Increasing the amount of water vapor corresponds to an increase in the overall polarity. Based on that the gradual decrease in the cutoff diameter by increasing the relative humidity can be explained.
Assuming spherical seed particles and a short residence time in the humidified air stream before entering the saturator of the CPC the following model describing particle nucleation and condensational growth can be proposed. The occurring processes can be subdivided into three separated subprocesses:

1. Particle Accumulation : Based on their polarity vapor molecules have the tendency to accumulate on the seed particle's surface by formation of hydrogen bonds (nucleation). Vapor polarity is likely to have an effect on the sticking probability of the seed particle surface. Preexisting charges on the surface enhance this process.

2. Particle Shrinkage: A sufficiently high number of vapor molecules is attached to the seed particle in order to start dissociative processes. The crystal lattice is restructured and particle shrinkage occurs. The separation of lattice ions additionally attracts vapor molecules due to their charge.

3. Water Uptake: The physicochemical parameters of the dissociation process initiate paticle growth. Water vapor is spontaneously taken up due to deliquescence.

The used relative humidities are clearly below the threshold of deliquescence. In the different mixing zones higher relative humidities are likely to occur.

8.5 Vapor Polarity and Vapor Uptake in PSMs

The findings of this thesis suggest different processes governing particle activation and growth in PSMs. There is no clear trend concerning a change in the cutoff diameters recognizable in the detection efficiency data. The relative humidity of the carrier gas does not seem to have a detectable influence on the cutoff diameter of the used instrument. In fact, the relative humidity of the carrier gas has an effect on PSMs too. This effect completely differs from the effect observed in CPCs. As already mentioned there is a difference between the method of establishing supersaturated conditions in CPCs and PSMs, although the basic construction of the instruments is similar. In CPCs laminar flow conditions are established inside the instrument. Supersaturation is based on non - isothermal diffusion processes. In the Airmodus A10 the supersaturation is produced by turbulent mixing. The use of turbulent mixing creates a highly dynamic environment. The overall polarity of the working fluid also increases by mixing it with water vapor. Particles are activated instantly. Turbulent mixing most likely lowers the activation barrier even more. As a result the expected shape of the cutoff curve changes. In fact the detection efficiency curves transform to nearly horizontal lines and no cutoff diameter can be calculated. The addition of water vapor also seems to increase the background noise drastically. On the other hand, the TSI 3777 Nano enhancer also uses non - isothermal diffusion to supersaturate the vapor in the condenser. This different mechanism results in different cutoff curves. The curve shape is preserved in all measurements. Higher relative humidities do not change the detection efficiency and no elevated background signal is induced. The appearance of smaller cutoff diameters can simply be credited to the use of DEG as working fluid. The higher polarity of DEG results in smaller cutoff diameters.

Generally, the effect of the surface tension of different working fluids has to be taken into account too. Following [58] the fluid with the highest surface tension leads to the smallest critical cluster diameter concerning particle activation. Furthermore Magnusson et al. state that this effect is even enhanced if the molecular weight of the fluid is high. The molecular weight of DEG is higher than the molecular weight of n - butanol. The surface tension of DEG is also higher than the surface tension of n - butanol. The enhanced particle activation is therefore also influenced by these parameters.

9 Future Work

The results of this thesis provide deeper insights into the physicochemical processes governing heterogeneous nucleation. Nevertheless there are a few open questions that need further investigation.

First of all there is one set of PSM - related data missing. Due to the large amount of conducted measurements data using positively charged Ag seed particles and 40 % of relative humidity is missing (RH=40%, AG(+), std Settings).

In order to further confirm the results for the butanol - based CPCs the measurements should be extended to other CPC models. The measurement set involving the TSI 3772 yielded different and unexpected results. Measurements using the TSI 3772 and different seed particles as well as different temperature settings are necessary. Measurements involving butanol - based CPCs with a cutoff diameter between the cutoff diameter of the TSI 3776 and the TSI 3772 (under standard operating conditions) could provide deeper insight into the dependence of the observed effects on the particle diameter. The Airmodus A20 or the TSI 3022A could be used for that purpose.

The measurements using DEG - based booster stages only allow for a rough estimate concerning the processes governing particle activation. Intensive research is needed in order to fully understand the activation behavior of these instruments. These additional measurements should include measurements on the effect of turbulent mixing in order to establish supersaturation. A monodisperse aerosol with a known particle number concentration can be sent through a turbulent mixing zone. Particle production inside of such a turbulent mixing zone needs to be investigated. Additionally the particle size distribution of a classified aerosol could be recorded after passing through a PSM. This size distribution most likely changes when the relative humidity of the carrier gas increases. One would expect a shift to larger sizes that depends on the amount of water vapor in the system.

Data analysis and interpretation of the data was based on one assumption: spherical particles. It is well known that NaCl particles produced by a tube furnace have differing shapes. In order the exclude a potential impact of the dynamic shape factor on particle activation similar experiments could be conducted using different seed particles [59]. Ammonium sulphate ($(NH_4)_2SO_4$), for example, is also soluble in polar solvents. Nevertheless it is chemically different from Ag or NaCl. Measurements based on ammonium sulphate could potentially provide further information about the effect of the relative humidity. Lastly, it should be mentioned, that the used setup only allowed for relative humidities up to 40 %. By designing a different setup, that provides the possibility to use higher relative humidities, the decreasing trend of cutoff diameters could be investigated in more detail.

10 Conclusion

This work experimentally investigated the physicochemical processes governing heterogeneous nucleation. A variety of experimental setups was used to measure the impact of the temperature and the relative humidity of the carrier gas on butanol - and DEG - based condensation particle counters. Precise control over the relevant physical parameters led to a qualitative analysis of the findings. Reproducible results were obtained and compared to recent literature. A decrease of the cutoff diameters of a commonly used CPC depending on the temperature settings and the relative humidity of the carrier gas for soluble seed particles could be confirmed. Furthermore the absence of this effect for insoluble seed particles was verified. Using DEG - based booster stages suggestions on the differences between two methods of establishing supersaturations were made. The foundations for further investigations of the physicochemical basics was built. A model for particle activation and growth combining three important effects was suggested. This thesis confirms the suggestions of G. Sem [34] and S. Schobesberger et al. [35]. Both authors suspect that there might be a dependence of the cutoff diameter based on sodium chloride particles on the relative humidity of the carrier gas.

The importance of measurements of the detection efficiencies of particle detectors and booster stages was pointed out. Cutoff diameters and detection efficiency curves provide a variety of important information. These curves are characteristic for an instrument's performance and contain information about the chosen setup. The overall curve shape, the position of the plateau and the occurrence of an offset in the detection efficiency data describe important physical parameters of a measurement, i. e. the balance of the flow rates, low or high pressure in the tubes, problems concerning size selection of the particles, contaminations with water vapor and problems linked to the particle concentrations. As a result measurements of cutoff curves should be performed with great care and highest possible accuracy. Unmindfully recorded cutoff curves yield inaccurate results and eventually lead to imprecise interpretations of the findings of an experiment.

It was found that the impact of vapor polarity on heterogeneous nucleation cannot be neglected. Due to the small particle sizes, interactions between single atoms are of major importance. Electrostatic attractions and repulsions are crucial processes on that scale. The initial steps, that eventually lead to condensational growth, are initiated and promoted by charge effects. RH dependent detection efficiency measurements of CPCs provide deeper insights into the physicochemical processes that influence the activation of nanometer - sized particles. A well - structured physicochemical approach is needed in order to completely understand nucleation processes. The measurements additionally confirm the approach chosen by Li and Hogan [50]. Depending on aerosol characteristics and the stage of the growth process different subprocesses are predominant. The identification of the hierarchy linked to these processes should be the focus of future research.

References

[1] B. L. Zhuang, S. Li, T. J. Wang, J. J. Deng, M.Xie, C. Q. Yin, and J. L. Zhu. Direct radiative forcing and climate effects of anthropogenic aerosols with different mixing states over China. *Atmospheric Environment*, 79:349–361, 2013.

[2] http://www.ipcc.ch/, 28.10.2018.

[3] G. Myhre, D. Shindell, F.-M. Bréon, W. Collins, J. Fuglestvedt, J. Huang, D. Koch, J.-F. Lamarque, D. Lee, B. Mendoza, T. Nakajima, A. Robock, G. Stephens, T. Takemura, and H. Zhang. *Anthropogenic and Natural Radiative Forcing. In: Climate Change 2013: The Physical Science Basis. Contribution of Working Group I to the Fifth Assessment Report of the Intergovernmental Panel on Climate Change*. Cambridge University Press, Cambridge, United Kingdom and New York, NY, USA, 2013.

[4] T. F. Stocker, D. Qin, G.-K. Plattner, M. Tignor, S.K. Allen, J. Boschung, A. Nauels, Y. Xia, V. Bex, and P. M. Midgley. *IPCC, 2013: Summary for Policymakers. In: Climate Change 2013: The Physical Science Basis. Contribution of Working Group I to the Fifth Assessment Report of the Intergovernmental Panel on Climate Change*. Cambridge University Press, Cambridge, United Kingdom and New York, NY, USA, 2013.

[5] M. Kulmala, J. Kontkanen, H. Junninen, K. Lehtipalo, H. E. Manninen, T. Nieminen, T. Petäjä, M. Sipilä, S. Schobesberger, P. Rantala, A. Franchin, T. Jokinen, E. Järvinen, M. Äijälä, J. Kangasluoma, J. Hakala, P. P. Aalto, P. Paasonen, J. Mikkilä, J. Vanhanen, J. Aalto, H. Hakola, U. Makkonen, T. Ruuskanen, R. L. Mauldin, J. Duplissy, H. Vehkamäki, J. Bäck, A. Kortelainen, I. Riipinen, T. Kurtén, M. V. Johnston, J. N. Smith, M. Ehn, T. F. Mentel, K. E. J. Lehtinen, A. Laaksonen, V. M. Kerminen, and D. R. Worsnop. Direct Observations of Atmospheric Aerosol Nucleation. *Science*, 339(6122):943–946, 2013.

[6] P. H. McMurry. The History of Condensation Nucleus Counters. *Aerosol Science and Technology*, 33(4):297–322, 2000.

[7] P. M. Winkler, G. Steiner, A. Vrtala, H. Vehkamäki, M. Noppel, K. E. Lehtinen, G. P. Reischl, P. E. Wagner, and M. Kulmala. Heterogeneous Nucleation Experiments Bridging the Scale from Molecular Ion Clusters to Nanoparticles. *Science*, 319(5868):1374–1377, 2008.

[8] C. Tauber, X. Chen, P. E. Wagner, P. M. Winkler, C. J. Hogan Jr., and A. Maißer. Heterogeneous Nucleation onto Monoatomic Ions: Support for the Kelvin-Thomson Theory. *ChemPhysChem*, 19:1–7, 2018.

[9] D. Kashchiev. *Nucleation*. Butterworth - Heinemann, 1 edition, 2000.

[10] W. C. Hinds. *Aerosol Technology: Properties, Behavior, and Measurement of Airborne Particles*. John Wiley and Sons, 2 edition, 1999.

[11] J. H. Seinfeld and S. N. Pandis. *Atmospheric Chemistry and Physics: From Air Pollution to Climate Change*. John Wiley and Sons, Inc., 2 edition, 2006.

[12] P. M. Winkler, R. L. McGraw, P. S. Bauer, C. Rentenberger, and P. E. Wagner. Direct determination of three-phase contact line properties on nearly molecular scale. *Scientific Reports*, 2016.

[13] http://www.tut.fi/en/research/research-fields/physics/aerosol-physics/aerosol-physics/index.htm, 17.07.2018.

[14] H. G. Scheubel and J. Porstendörfer. Generation of Monodisperse Ag- and NaCl- Aerosol with Particle Diameters between 2 and 300 nm. *Journal of Aerosol Science*, 14(2):113–126, 1982.

[15] G. Steiner. *High Resolution Mobility Spectrometry Of Molecular Ions And Their Effect On The Charging Probabilities Of Airborne Particles Under Bipolar Diffusion Charging Conditions*. PhD thesis, University of Vienna, 2011.

[16] P. Kallinger, G. Steiner, and W. W. Szymanski. Characterization of four different bipolar charging devices for nanoparticle charge conditioning. *Journal of Nanoparticle Research*, (14):944, 2012.

[17] P. Kulkarni, P. Baron, and K. Willeke, editors. *Aerosol Measurement: Principles, Techniques, and Applications*. Wiley Interscience NY, 2011.

[18] G. Steiner and G. P. Reischl. The effect of carrier gas contaminants on the charging probability of aerosols under bipolar charging conditions. *Journal of Aerosol Science*, 54:21 – 31, 2012.

[19] G. Steiner, M. Attoui, D. Wimmer, and G. P. Reischl. A Medium Flow, High-Resolution Vienna DMA Running in Recirculating Mode. *Aerosol Science and Technology*, 44(4):308–315, 2010.

[20] E. Cunningham and J. Larmor. On the velocity of steady fall of spherical particles through fluid medium. *Proceedings of the Royal Society of London. Series A, Containing Papers of a Mathematical and Physical Character*, 83:357–365, 1910.

[21] K. Pihlava, J. Keskinen, and J. Yli-Ojanperä. Improving the signal-to-noise ratio of Faraday cup aerosol electrometer based aerosol instrument calibrations. *Aerosol Science and Technology*, 50(4):373–379, 2016.

[22] Y. Yang, T. Yu, J. Zhang, J. Wang, W. Wang, H. Gui, and J. Liu. On the Performance of an Aerosol Electrometer with Enhanced Detection Limit. *Sensors*, 18:3889, 11 2018.

[23] A. Järvinen, J. Keskinen, and J. Yli-Ojanperä. Extending the Faraday cup aerosol electrometer based calibration method up to 5 μm. *Aerosol Science and Technology*, 52(8):828–840, 2018.

[24] N. A. Fuchs. On the stationary charge distribution on aerosol particles in a bipolar ionic atmosphere. *Geofisica pura e applicata*, 56(1):185–193, Sep 1963.

[25] P. Intra and N. Tippayawong. Measurements of ion current from a corona-needle charger using a Faraday cup electrometer. *Chiang Mai Journal of Science*, 36:110 – 119, 01 2009.

[26] http://tsi.com/uploadedFiles/_Site_Root/Products/Literature/Spec_Sheets/3776_2980345.pdf, 28.10.2018.

[27] N. Takegawa, K. Iida, and H. Sakurai. Modification and laboratory evaluation of a TSI ultrafine condensation particle counter (Model 3776) for airborne measurements. *Aerosol Science and Technology*, 51(2):235–245, 2017.

[28] M. R. Stolzenburg and P. H. McMurry. An ultrafine aerosol condensation nucleus counter. *Aerosol Science and Technology*, 14(1):48–65, 1991.

[29] D. Wimmer, K. Lehtipalo, A. Franchin, J. Kangasluoma, F., A. Kürten, A. Kupc, A. Metzger, J. Mikkilä, T. Petäjä, F. Riccobono, J. Vanhanen, M. Kulmala, and J. Curtius. Performance of diethylene glycol-based particle counters in the sub-3 nm size range. *Atmospheric Measurement Techniques*, 6(7):1793–1804, 2013.

[30] https://airmodus.com/wp-content/uploads/2017/12/a10psm_datasheet_170913.pdf, 09.02.2019.

[31] http://www.tsi.com/uploadedFiles/_Site_Root/Products/Literature/Application_Notes/3777_Nano_Enhancer_Theory_of_Op_3777-001_A4-web.pdf, 28.10.2018.

[32] J. Vanhanen, J. Mikkilä, K. Lehtipalo, M. Sipilä, H. E. Manninen, E. Siivola, T. Petäjä, and M. Kulmala. Particle Size Magnifier for Nano-CN Detection. *Aerosol Science and Technology*, 45(4):533–542, 2011.

[33] J. Kangasluoma, A. Franchin, J. Duplissy, L. Ahonen, F. Korhonen, M. Attoui, J. Mikkilä, K. Lehtipalo, J. Vanhanen, M. Kulmala, and T. Petäjä. Operation of the Airmodus A11 nano Condensation Nucleus Counter at various inlet pressures and various operation temperatures, and design of a new inlet system. *Atmospheric Measurement Techniques*, 9(7):2977–2988, 2016.

[34] G. J. Sem. Design and performance characteristics of three continuous-flow condensation particle counters: a summary. *Atmospheric Research*, (62):267–294, 2002.

[35] S. Schobesberger, P. M. Winkler, T. Pinterich, A. Vrtala, M. Kulmala, and P. E. Wagner. Experiments on the Temperature Dependence of Heterogeneous Nucleation on Nanometer-Sized NaCl and Ag Particles. *ChemPhysChem*, 11(18):3874–3882, 2010.

[36] C. Tauber, G. Steiner, and P. M. Winkler. Counting efficiency determination from quantitative intercomparison between expansion and laminar flow type condensation particle counter. *Aerosol Science and Technology*, 2019. https://doi.org/10.1080/02786826.2019.1568382.

[37] K. Barmpounis, A. Ranjithkumar, A. Schmidt-Ott, M. Attoui, and G. Biskos. Enhancing the detection efficiency of condensation particle counters for sub-2 nm particles. *Journal of Aerosol Science*, (117):44–53, 2018.

[38] C. Tauber, S. Brilke, P. J. Wlasits, P. S. Bauer, G. Köberl, G. Steiner, and P. M. Winkler. Humidity effects on the detection of soluble and insoluble nanoparticles in butanol operated condensation particle counters. *Atmospheric Measurement Techniques Discussions*, 2019. in review.

[39] C. Tauber. *On the Charge, Temperature and Humidity Dependence of Heterogeneous Nucleation of n-Butanol Vapor for Improved Nano-particle Detection.* PhD thesis, University of Vienna, 2019.

[40] A. Wiedensohler. An approximation of the bipolar charge distribution for particles in the submicron size range. *Journal of Aerosol Science*, 19(3):387 – 389, 1988.

[41] E. O. Lebigot. Uncertainties: a Python package for calculations with uncertainties. http://pythonhosted.org/uncertainties/.

[42] http://tsi.com/uploadedFiles/_Site_Root/Products/Literature/Spec_Sheets/3068B.pdf, 28.10.2018.

[43] https://www.sensidyne.com/air-sampling-equipment/calibration-equipment/gilibrator-2/, 28.10.2018.

[44] http://www.tsi.com/uploadedFiles/Product_Information/Literature/Manuals/1980340G.pdf, 28.10.2018.

[45] Airmodus Ltd. *User Manual: nano Condensation Nucleus Counter system, Model A11 nCNC*, 2014.

[46] J. F. de la Mora and S. Ude. Molecular monodisperse mobility and mass standards from electrosprays of tetra-alkyl ammonium halides. *Journal of Aerosol Science*, 36:1224–1237, 2005.

[47] J. M. Mäkelä, M. Riihelä, A. Ukkonen, V. Jokinen, and J. Keskinen. Comparison of mobility equivalent diameter with Kelvin-Thomson diameter using ion mobility data. *The Journal of Chemical Physics*, 105(4):1562–1571, 1996.

[48] J. Kangasluoma, A. Samodurov, M. Attoui, A. Franchin, H. Junninen, F. Korhonen, T. Kurtén, H. Vehkamäki, M. Sipilä, K. Lehtipalo, D. R. Worsnop, T. Petäjä, and

M. Kulmala. Heterogeneous Nucleation onto Ions and Neutralized Ions: Insights into Sign-Preference. *The Journal of Physical Chemistry C*, 120(13):7444–7450, 2016.

[49] https://www.kenelec.com.au/ken/wp-content/uploads/2016/06/TSI_3772_Spec_Sheet.pdf, 12.02.2019.

[50] C. Li and C. J. Hogan Jr. Vapor specific extents of uptake by nanometer scale charged particles. *Aerosol Science and Technology*, 51(5):653–664, 2017.

[51] L. Krämer, U. Pöschl, and R. Niessner. Microstructural rearrangement of sodium chloride condensation aerosol particles on interaction with water vapor. *Journal of Aerosol Science*, 31:673–685, 2000.

[52] G. Biskos, A. Malinowski, L. M. Russell, P. R. Buseck, and S. T. Martin. Nanosize Effect on the Deliquescence and the Efflorescence of Sodium Chloride Particles. *Aerosol Science and Technology*, 40(2):97–106, 2006.

[53] R. Mortimer. *Physical Chemistry: Third Edition*. Elsevier, 2008.

[54] P. Atkins and J. de Paula. *Physical Chemistry*. Oxford University Press, 2006.

[55] C. Reichardt and T. Welton. *Solvents and Solvent Effects in Organic Chemistry*. Wiley VCH, 2010.

[56] Jmol: an open-source java viewer for chemical structures in 3D. http://www.jmol.org/.

[57] P. Politzer, P. R. Laurence, and K. Jayasuriya. Molecular electrostatic potentials: an effective tool for the elucidation of biochemical phenomena. *Environmental Health Perspectives*, (61):191–202, 1985.

[58] L. E. Magnusson, J. A. Koropchak, M. P. Anisimov, V. M. Poznjakovskiy, and J. F. de la Mora. Correlations for Vapor Nucleating Critical Embryo Parameters. *Journal of Physical and Chemical Reference Data*, 32(4):1387–1410, 2003.

[59] P. Zieger, O. Väisänen, J. C. Corbin, D. G. Partridge, S. Bastelberger, M. Mousavi-Fard, B. Rosati, M. Gysel, U. K. Krieger, C. Leck, A. Nenes, I. Riipinen, A. Virtanen, and M. E. Salter. Revising the hygroscopicity of inorganic sea salt particles. *Nature Communications*, 8(15883), 2017.

A Voltage Patterns Applied to the nDMA

d_p [nm]	Voltage [V]	d_p [nm]	Voltage [V]	d_p [nm]	Voltage [V]
1.00	6.40	3.00	57.27	6.50	266.08
1.30	10.81	3.20	65.12	7.00	308.14
1.50	14.38	3.50	77.83	7.50	353.21
1.70	18.46	4.00	101.51	8.00	401.28
2.00	25.53	4.50	128.28	9.00	506.37
2.30	33.73	5.00	158.14	10.00	623.31
2.50	39.83	5.40	184.24		
2.70	46.43	6.00	227.05		

Table 12: Voltage Pattern "d_p full range"

d_p [nm]	Voltage [V]	d_p [nm]	Voltage [V]
1.50	14.38	3.00	57.27
1.70	18.46	3.50	77.83
2.00	25.53	4.00	101.51
2.30	33.73	4.50	128.28
2.50	39.83	5.00	158.14

Table 13: Voltage Pattern "d_p low range"

d_p [nm]	Voltage [V]	d_p [nm]	Voltage [V]
5.00	158.14	7.50	353.21
5.40	184.24	8.00	401.28
6.00	227.05	9.00	506.37
6.50	266.08	10.00	623.31
7.00	308.14		

Table 14: Voltage Pattern "d_p high range"

B Preparation of the THABr Solution

The following chemical quantities are needed in order to produce the THABr solution for the UDMA calibration:

Symbol	Quantity	Unit
m	Mass	kg
n	Amount of Substance	mol
M	Molar Mass	$g \cdot mol^{-1}$

Table 15: Chemical Quantities

The following fundamental relation holds:

$$n = \frac{m}{M}. \tag{35}$$

THABr has a molar mass of 490.669 $g \cdot mol^{-1}$. 1 mMol is equal to 0.001 mol and therefore

$$m = M \cdot m = 0.4907g. \tag{36}$$

50 mL of solution are produced. For 50 mL of solution 0.0245 g THABr have to be dissolved in 50 mL of acetonitrile.

C Serial Numbers of Used Particle Detectors

Instrument	Model	Number[1]	Serial Number
UCPC	TSI 3776	2	3776143302
UCPC	TSI 3776	3	3776143303
UCPC	TSI 3776	4	3776142801
UCPC	TSI 3776	5	3776143401
CPC	TSI 3772	x	3772160601
CPC	A20	x	2271545336
PSM	A10	x	A1013050106
PSM	TSI 3777	x	3777160401
FCE	TSI 3068B	x	3776143401

Table 16: Used Particle Detectors

[1] corresponding to the stickers on the instruments

D CPCs In Use

Seed	T-Setting	RH [%]	CPC	Seed	T-Setting	RH [%]	CPC
NaCl(+)	low	0	4	NaCl(0+)	low	0	3
NaCl(+)	std	0	4	NaCl(0+)	std	0	3
NaCl(+)	high	0	5	NaCl(0+)	high	0	3
NaCl(-)	low	0	4	NaCl(0-)	low	0	3
NaCl(-)	std	0	3	NaCl(0-)	std	0	3
NaCl(-)	high	0	3	NaCl(0-)	high	0	3
NaCl(+)	low	10	5	NaCl(0+)	low	10	3
NaCl(+)	std	10	5	NaCl(0+)	std	10	4
NaCl(+)	high	10	5	NaCl(0+)	high	10	4
NaCl(-)	low	10	5	NaCl(0-)	low	10	3
NaCl(-)	std	10	5	NaCl(0-)	std	10	4
NaCl(-)	high	10	5	NaCl(0-)	high	10	4
NaCl(+)	low	20	3	NaCl(0+)	low	20	3
NaCl(+)	std	20	4	NaCl(0+)	std	20	3
NaCl(+)	high	20	4	NaCl(0+)	high	20	4
NaCl(-)	low	20	3	NaCl(0-)	low	20	3
NaCl(-)	std	20	3	NaCl(0-)	std	20	3
NaCl(-)	high	20	3	NaCl(0-)	high	20	4
NaCl(+)	low	30	4	NaCl(0+)	low	30	3
NaCl(+)	std	30	4	NaCl(0+)	std	30	3
NaCl(+)	high	30	3	NaCl(0+)	high	30	4
NaCl(-)	low	30	4	NaCl(0-)	low	30	3
NaCl(-)	std	30	4	NaCl(0-)	std	30	3
NaCl(-)	high	30	3	NaCl(0-)	high	30	4
NaCl(+)	low	40	4	NaCl(0+)	low	40	3
NaCl(+)	std	40	2	NaCl(0+)	std	40	3
NaCl(+)	high	40	2	NaCl(0+)	high	40	4
NaCl(-)	low	40	3	NaCl(0-)	low	40	3
NaCl(-)	std	40	3	NaCl(0-)	std	40	3
NaCl(-)	high	40	3	NaCl(0-)	high	40	4

Table 17: CPC - Based Measurements and NaCl Seeds

Seed	T-Setting	RH [%]	CPC	Seed	T-Setting	RH [%]	CPC
Ag(+)	low	0	4	Ag(0+)	low	0	3
Ag(+)	std	0	3	Ag(0+)	std	0	4
Ag(+)	high	0	5	Ag(0+)	high	0	4
Ag(-)	low	0	4	Ag(0-)	low	0	3
Ag(-)	std	0	4	Ag(0-)	std	0	4
Ag(-)	high	0	5	Ag(0-)	high	0	4
Ag(+)	low	10	5	Ag(0+)	low	10	3
Ag(+)	std	10	5	Ag(0+)	std	10	4
Ag(+)	high	10	4	Ag(0+)	high	10	4
Ag(-)	low	10	4	Ag(0-)	low	10	3
Ag(-)	std	10	4	Ag(0-)	std	10	4
Ag(-)	high	10	5	Ag(0-)	high	10	4
Ag(+)	low	20	4	Ag(0+)	low	20	3
Ag(+)	std	20	4	Ag(0+)	std	20	4
Ag(+)	high	20	5	Ag(0+)	high	20	4
Ag(-)	low	20	4	Ag(0-)	low	20	3
Ag(-)	std	20	4	Ag(0-)	std	20	4
Ag(-)	high	20	5	Ag(0-)	high	20	4
Ag(+)	low	30	4	Ag(0+)	low	30	3
Ag(+)	std	30	4	Ag(0+)	std	30	4
Ag(+)	high	30	5	Ag(0+)	high	30	4
Ag(-)	low	30	4	Ag(0-)	low	30	3
Ag(-)	std	30	4	Ag(0-)	std	30	4
Ag(-)	high	30	5	Ag(0-)	high	30	4
Ag(+)	low	40	4	Ag(0+)	low	40	3
Ag(+)	std	40	4	Ag(0+)	std	40	3
Ag(+)	high	40	5	Ag(0+)	high	40	4
Ag(-)	low	40	4	Ag(0-)	low	40	3
Ag(-)	std	40	5	Ag(0-)	std	40	3
Ag(-)	high	40	5	Ag(0-)	high	40	4

Table 18: CPC - Based Measurements and Ag Seeds

E Summary of Measured Cutoff Diameters

CPC - Based Measurements

Seed	T-Setting	RH [%]	d_{50} [nm]	$\Delta(d_{50})$ [nm]	$\mathcal{N}_{min}$ $[cm^{-3}]$	$\mathcal{N}_{max}$ $[cm^{-3}]$
NaCl(+)	low	0	3.70	0.30	300	40000
NaCl(+)	std	0	4.41	0.36	500	50000
NaCl(+)	high	0	4.72	0.39	500	12500
NaCl(-)	low	0	2.99	0.25	500	30000
NaCl(-)	std	0	4.32	0.35	300	30000
NaCl(-)	high	0	4.76	0.39	1000	30000
NaCl(+)	low	10	2.45	0.20	500	35000
NaCl(+)	std	10	3.82	0.31	300	35000
NaCl(+)	high	10	4.98	0.41	300	35000
NaCl(-)	low	10	2.82	0.23	250	30000
NaCl(-)	std	10	3.77	0.31	500	40000
NaCl(-)	high	10	4.95	0.41	200	40000
NaCl(+)	low	20	2.35	0.19	200	8000
NaCl(+)	std	20	3.14	0.26	200	12000
NaCl(+)	high	20	4.61	0.38	500	11000
NaCl(-)	low	20	2.28	0.19	100	10000
NaCl(-)	std	20	2.69	0.22	200	20000
NaCl(-)	high	20	4.11	0.34	500	15000
NaCl(+)	low	30	1.96	0.16	300	10000
NaCl(+)	std	30	2.45	0.20	500	20000
NaCl(+)	high	30	4.09	0.34	200	18000
NaCl(-)	low	30	1.50	0.12	200	15000
NaCl(-)	std	30	2.40	0.20	200	15000
NaCl(-)	high	30	4.02	0.33	250	30000
NaCl(+)	low	40	1.84	0.15	500	17500
NaCl(+)	std	40	2.04	0.17	1500	15000
NaCl(+)	high	40	3.18	0.26	800	12500
NaCl(-)	low	40	1.23	0.10	500	20000
NaCl(-)	std	40	1.84	0.15	500	25000
NaCl(-)	high	40	3.33	0.27	1000	25000

Table 19: CPC - Based Measurements: Charged NaCl Seeds, measurements performed in cooperation with C. Tauber; [38] and [39]

Seed	T-Setting	RH [%]	d_{50} [nm]	$\Delta(d_{50})$ [nm]	$\mathcal{N}_{min}$ $[cm^{-3}]$	$\mathcal{N}_{max}$ $[cm^{-3}]$
Ag(+)	low	0	2.57	0.21	200	30000
Ag(+)	std	0	3.03	0.25	500	20000
Ag(+)	high	0	3.47	0.28	200	18000
Ag(-)	low	0	2.12	0.17	200	25000
Ag(-)	std	0	2.54	0.21	200	7000
Ag(-)	high	0	3.00	0.25	200	3000
Ag(+)	low	10	2.29	0.19	1000	25000
Ag(+)	std	10	2.77	0.23	2000	25000
Ag(+)	high	10	3.23	0.26	1000	12000
Ag(-)	low	10	2.15	0.18	2000	25000
Ag(-)	std	10	2.69	0.22	200	6000
Ag(-)	high	10	3.18	0.26	2000	15000
Ag(+)	low	20	2.37	0.19	100	6000
Ag(+)	std	20	2.89	0.24	1000	70000
Ag(+)	high	20	3.11	0.25	200	80000
Ag(-)	low	20	2.11	0.17	500	8000
Ag(-)	std	20	2.66	0.22	250	5000
Ag(-)	high	20	3.11	0.25	200	3000
Ag(+)	low	30	2.27	0.19	200	6000
Ag(+)	std	30	2.60	0.21	200	3000
Ag(+)	high	30	2.99	0.25	100	3000
Ag(-)	low	30	2.12	0.17	500	6000
Ag(-)	std	30	2.54	0.24	400	4000
Ag(-)	high	30	3.00	0.25	250	4000
Ag(+)	low	40	2.49	0.20	500	6000
Ag(+)	std	40	2.95	0.24	500	6000
Ag(+)	high	40	3.08	0.25	500	6000
Ag(-)	low	40	2.41	0.20	600	6000
Ag(-)	std	40	2.42	0.20	400	6000
Ag(-)	high	40	2.99	0.24	1000	18000

Table 20: CPC - Based Measurements: Charged Ag Seeds, measurements performed in cooperation with C. Tauber; [38] and [39]

Seed	T-Setting	RH [%]	d_{50} [nm]	$\Delta(d_{50})$ [nm]	$\mathcal{N}_{min}$ $[cm^{-3}]$	$\mathcal{N}_{max}$ $[cm^{-3}]$
NaCl(0+)	low	0	3.20	0.26	500	15000
NaCl(0+)	std	0	3.78	0.31	500	15000
NaCl(0+)	high	0	4.57	0.38	500	15000
NaCl(0-)	low	0	3.14	0.26	250	70000
NaCl(0-)	std	0	3.96	0.32	250	60000
NaCl(0-)	high	0	4.59	0.38	400	30000
NaCl(0+)	low	10	2.41	0.20	200	8000
NaCl(0+)	std	10	3.31	0.27	200	7500
NaCl(0+)	high	10	4.30	0.35	400	6000
NaCl(0-)	low	10	2.14	0.18	500	30000
NaCl(0-)	std	10	3.20	0.26	500	30000
NaCl(0-)	high	10	4.26	0.35	500	25000
NaCl(0+)	low	20	2.36	0.19	400	10000
NaCl(0+)	std	20	2.81	0.23	500	7500
NaCl(0+)	high	20	4.10	0.34	500	7000
NaCl(0-)	low	20	1.92	0.16	800	25000
NaCl(0-)	std	20	2.60	0.21	800	20000
NaCl(0-)	high	20	4.04	0.33	600	20000
NaCl(0+)	low	30	2.04	0.17	100	10000
NaCl(0+)	std	30	2.32	0.19	100	10000
NaCl(0+)	high	30	3.00	0.25	1000	11000
NaCl(0-)	low	30	1.54	0.13	500	25000
NaCl(0-)	std	30	1.80	0.15	500	25000
NaCl(0-)	high	30	2.86	0.23	100	15000
NaCl(0+)	low	40	1.95	0.16	100	12000
NaCl(0+)	std	40	2.20	0.18	800	13500
NaCl(0+)	high	40	2.68	0.22	100	14000
NaCl(0-)	low	40	1.63	0.13	500	15000
NaCl(0-)	std	40	1.76	0.14	500	15000
NaCl(0-)	high	40	2.49	0.20	1000	20000

Table 21: CPC - Based Measurements: Neutralized NaCl Seeds, measurements performed in cooperation with C. Tauber; [38] and [39]

Seed	T-Setting	RH [%]	d_{50} [nm]	$\Delta(d_{50})$ [nm]	$\mathcal{N}_{min}$ $[cm^{-3}]$	$\mathcal{N}_{max}$ $[cm^{-3}]$
Ag(0+)	low	0	2.22	0.18	300	80000
Ag(0+)	std	0	3.02	0.25	300	70000
Ag(0+)	high	0	3.93	0.32	1500	35000
Ag(0-)	low	0	2.32	0.19	250	70000
Ag(0-)	std	0	2.96	0.24	250	60000
Ag(0-)	high	0	3.81	0.31	400	30000
Ag(0+)	low	10	2.52	0.21	250	35000
Ag(0+)	std	10	3.06	0.25	250	35000
Ag(0+)	high	10	3.80	0.31	300	20000
Ag(0-)	low	10	2.41	0.20	500	30000
Ag(0-)	std	10	2.98	0.25	500	30000
Ag(0-)	high	10	3.69	0.30	500	25000
Ag(0+)	low	20	2.51	0.21	250	20000
Ag(0+)	std	20	3.31	0.27	250	20000
Ag(0+)	high	20	3.73	0.31	250	20000
Ag(0-)	low	20	2.33	0.19	800	25000
Ag(0-)	std	20	3.06	0.25	800	20000
Ag(0-)	high	20	4.06	0.33	600	20000
Ag(0+)	low	30	2.46	0.20	250	12000
Ag(0+)	std	30	2.82	0.23	250	12000
Ag(0+)	high	30	3.98	0.33	100	20000
Ag(0-)	low	30	2.28	0.19	500	25000
Ag(0-)	std	30	2.74	0.22	500	25000
Ag(0-)	high	30	3.98	0.33	100	15000
Ag(0+)	low	40	2.48	0.20	250	12000
Ag(0+)	std	40	2.77	0.23	200	10000
Ag(0+)	high	40	3.37	0.28	500	15000
Ag(0-)	low	40	2.33	0.19	500	15000
Ag(0-)	std	40	2.70	0.22	500	15000
Ag(0-)	high	40	3.37	0.28	1000	20000

Table 22: CPC - Based Measurements: Neutralized Ag Seeds, measurements performed in cooperation with C. Tauber; [38] and [39]

Seed	T-Setting	RH [%]	d_{50} [nm]	$\Delta(d_{50})$ [nm]	$\mathcal{N}_{min}$ $[cm^{-3}]$	$\mathcal{N}_{max}$ $[cm^{-3}]$
Ag(+)	std	0	7.82	1.02	100	6000
Ag(+)	std	10	7.83	1.02	100	5000
Ag(+)	std	20	8.00	1.04	500	5000
Ag(+)	std	30	6.81	0.89	2500	15000
Ag(+)	std	40	6.83	0.89	1000	7500
Ag(-)	std	0	7.95	1.03	1000	7500
Ag(-)	std	10	8.12	1.05	900	7000
Ag(-)	std	20	8.12	1.06	500	6000
Ag(-)	std	30	6.77	0.88	2500	12000
Ag(-)	std	40	6.92	0.90	250	80000

Table 23: TSI 3772: Charged Ag Seeds

PSM - Based Measurements

Seed	T-Setting	RH [%]	d_{50} [nm]	$\Delta(d_{50})$ [nm]	$\mathcal{N}_{min}$ $[cm^{-3}]$	$\mathcal{N}_{max}$ $[cm^{-3}]$
NaCl(+)	std	0	x	x	300	3500
NaCl(+)	cld	0	1.70	0.04	250	2500
NaCl(-)	std	0	1.63	0.04	200	3500
NaCl(-)	cld	0	1.59	0.04	250	3000
NaCl(+)	std	10	x	x	250	1300
NaCl(+)	cld	10	1.68	0.04	200	1700
NaCl(-)	std	10	1.44	0.04	200	1300
NaCl(-)	cld	10	1.48	0.04	200	2000
NaCl(+)	std	40	x	x	1000	2500
NaCl(+)	cld	40	x	x	800	2000
NaCl(-)	std	40	x	x	1000	3000
NaCl(-)	cld	40	x	x	500	2000

Table 24: PSM: Charged NaCl Seeds

Seed	T-Setting	RH [%]	d_{50} [nm]	$\Delta(d_{50})$ [nm]	$\mathcal{N}_{min}$ $[cm^{-3}]$	$\mathcal{N}_{max}$ $[cm^{-3}]$
NaCl(+)	std	0	1.82	0.05	300	3500
NaCl(+)	cld	0	1.73	0.05	200	3500
NaCl(-)	std	0	1.72	0.05	100	4000
NaCl(-)	cld	0	1.61	0.04	200	4500
NaCl(+)	std	10	1.85	0.05	200	1500
NaCl(+)	cld	10	1.79	0.04	200	2000
NaCl(-)	std	10	1.86	0.05	100	1000
NaCl(-)	cld	10	1.65	0.04	150	2500
NaCl(+)	std	40	1.84	0.05	700	2000
NaCl(+)	cld	40	1.90	0.05	700	2000
NaCl(-)	std	40	1.81	0.05	1000	4000
NaCl(-)	cld	40	1.44	0.04	300	2500

Table 25: NE: Charged NaCl Seeds

Seed	T-Setting	RH [%]	d_{50} [nm]	$\Delta(d_{50})$ [nm]	$\mathcal{N}_{min}$ $[cm^{-3}]$	$\mathcal{N}_{max}$ $[cm^{-3}]$
NaCl(+)	tuned	0	1.96	0.05	300	4000
NaCl(-)	tuned	0	1.90	0.05	150	4500
NaCl(+)	tuned	10	1.95	0.05	250	1500
NaCl(-)	tuned	10	1.65	0.04	200	1500
NaCl(+)	tuned	40	1.73	0.05	500	2000
NaCl(-)	tuned	40	1.79	0.05	1000	3000

Table 26: Tuned CPC: Charged NaCl Seeds

Seed	T-Setting	RH [%]	d_{50} [nm]	$\Delta(d_{50})$ [nm]	$\mathcal{N}_{min}$ $[cm^{-3}]$	$\mathcal{N}_{max}$ $[cm^{-3}]$
Ag(+)	std	0	x	x	1000	18000
Ag(+)	cld	0	1.75	0.04	300	10000
Ag(-)	std	0	1.44	0.04	500	15000
Ag(-)	cld	0	1.56	0.04	400	7500
Ag(+)	std	10	x	x	1000	3800
Ag(+)	cld	10	1.70	0.05	300	4000
Ag(-)	std	10	x	x	150	2500
Ag(-)	cld	10	1.65	0.04	100	2000
Ag(+)	std	40	x	x	1000	2000
Ag(+)	cld	40	x	x	1000	4000
Ag(-)	std	40	x	x	1000	3000
Ag(-)	cld	40	x	x	1000	3000

Table 27: PSM: Charged Ag Seeds

Seed	T-Setting	RH [%]	d_{50} [nm]	$\Delta(d_{50})$ [nm]	$\mathcal{N}_{min}$ $[cm^{-3}]$	$\mathcal{N}_{max}$ $[cm^{-3}]$
Ag(+)	std	0	2.58	0.07	500	20000
Ag(+)	cld	0	2.03	0.05	1000	12000
Ag(-)	std	0	2.40	0.06	250	22000
Ag(-)	cld	0	1.75	0.05	100	9000
Ag(+)	std	10	2.67	0.07	250	1000
Ag(+)	cld	10	2.21	0.06	50	2000
Ag(-)	std	10	1.86	0.05	150	2500
Ag(-)	cld	10	1.80	0.05	25	2000
Ag(+)	std	40	x	x	400	2000
Ag(+)	cld	40	2.09	0.05	100	4000
Ag(-)	std	40	2.39	0.06	400	4000
Ag(-)	cld	40	1.91	0.05	100	2200

Table 28: NE: Charged Ag Seeds

Seed	T-Setting	RH [%]	d_{50} [nm]	$\Delta(d_{50})$ [nm]	$\mathcal{N}_{min}$ $[cm^{-3}]$	$\mathcal{N}_{max}$ $[cm^{-3}]$
Ag(+)	tuned	0	2.10	0.06	500	18000
Ag(-)	tuned	0	1.81	0.05	500	18000
Ag(+)	tuned	10	1.88	0.05	150	3800
Ag(-)	tuned	10	1.62	0.04	150	2500
Ag(+)	tuned	40	x	x	500	2000
Ag(-)	tuned	40	1.74	0.05	1000	3000

Table 29: Tuned CPC: Charged Ag Seeds

F Sheath Air Flow Rates of the UDMA

Seed	T-Setting	RH [%]	Q_{sh} [lpm]
NaCl(+)	std	0	373.21
NaCl(+)	cld	0	380.33
NaCl(-)	std	0	373.21
NaCl(-)	cld	0	380.33
NaCl(+)	std	10	380.06
NaCl(+)	cld	10	380.06
NaCl(-)	std	10	379.32
NaCl(-)	cld	10	379.32
NaCl(+)	std	40	382.16
NaCl(+)	cld	40	390.14
NaCl(-)	std	40	382.16
NaCl(-)	cld	40	390.14

Table 30: PSM: Charged NaCl Seeds

Seed	T-Setting	RH [%]	Q_{sh} [lpm]
NaCl(+)	std	0	373.21
NaCl(+)	cld	0	380.33
NaCl(-)	std	0	373.21
NaCl(-)	cld	0	380.33
NaCl(+)	std	10	380.06
NaCl(+)	cld	10	380.06
NaCl(-)	std	10	379.32
NaCl(-)	cld	10	379.32
NaCl(+)	std	40	382.16
NaCl(+)	cld	40	390.14
NaCl(-)	std	40	382.16
NaCl(-)	cld	40	390.14

Table 31: NE: Charged NaCl Seeds

Seed	T-Setting	RH [%]	Q_{sh} [lpm]
NaCl(+)	tuned	0	373.21
NaCl(-)	tuned	0	373.21
NaCl(+)	tuned	10	380.06
NaCl(-)	tuned	10	379.32
NaCl(+)	tuned	40	382.16
NaCl(-)	tuned	40	382.16

Table 32: Tuned CPC: Charged NaCl Seeds

Seed	T-Setting	RH [%]	Q_{sh} [lpm]
Ag(+)	std	0	377.76
Ag(+)	cld	0	392.77
Ag(-)	std	0	400.53
Ag(-)	cld	0	373.36
Ag(+)	std	10	380.24
Ag(+)	cld	10	380.24
Ag(-)	std	10	381.83
Ag(-)	cld	10	373.36
Ag(+)	std	40	388.77
Ag(+)	cld	40	383.76
Ag(-)	std	40	383.76
Ag(-)	cld	40	383.76

Table 33: PSM: Charged Ag Seeds

Seed	T-Setting	RH [%]	Q_{sh} [lpm]
Ag(+)	std	0	377.76
Ag(+)	cld	0	392.77
Ag(-)	std	0	400.53
Ag(-)	cld	0	373.36
Ag(+)	std	10	380.24
Ag(+)	cld	10	380.24
Ag(-)	std	10	381.83
Ag(-)	cld	10	373.36
Ag(+)	std	40	388.77
Ag(+)	cld	40	383.76
Ag(-)	std	40	383.76
Ag(-)	cld	40	383.76

Table 34: NE: Charged Ag Seeds

Seed	T-Setting	RH [%]	Q_{sh} [lpm]
Ag(+)	tuned	0	377.76
Ag(-)	tuned	0	400.53
Ag(+)	tuned	10	380.24
Ag(-)	tuned	10	381.83
Ag(+)	tuned	40	388.77
Ag(-)	tuned	40	383.76

Table 35: Tuned CPC: Charged Ag Seeds